

Investigating of optical device and sensing application by using photonic liquid crystal fiber

Zhang, Yifan

2013

Zhang, Y. (2013). Investigating of optical device and sensing application by using photonic liquid crystal fiber. Doctoral thesis, Nanyang Technological University, Singapore.

<https://hdl.handle.net/10356/54678>

<https://doi.org/10.32657/10356/54678>

**INVESTIGATING OF OPTICAL
DEVICE AND SENSING
APPLICATION BY USING
PHOTONIC LIQUID CRYSTAL
FIBER**

ZHANG YIFAN

School of Chemical & Biomedical Engineering

A thesis submitted to the Nanyang Technological University
in partial fulfillment of the requirement for the degree of
Doctor of Philosophy

2013

Statement of Originality

I hereby certify that the work embodied in this thesis is the result of original research done by me and has not been submitted for a higher degree to any other University or Institute.

.....
Date

.....
ZHANG YIFAN

Acknowledgments

Without the effort and support from many individuals, it would be impossible for me to overcome obstacles encountered throughout the years of my research project. Here, I would like to express my gratitude and appreciation to all of them.

I would like to express my deepest gratitude to my advisor, Prof. Chan Chi Chiu, for making my study stimulating and enjoyable. By giving me a great deal of freedom to explore this research topic, he has also taught me how to effectively present and promote my own work. These skills will surely go a long way wherever my career takes me.

My thanks also go to Prof. Shum Ping, director of Network Technology Research Centre (NTRC) and Prof. Sun Xiaowei. They and their research groups have been instrumental in providing the equipment and assistance for many of my experiments. I am especially grateful for them providing me the chance to study in friendly and entertaining research centre.

I also thank the past and present members of NTRC. In particular, I owe special thanks to Dr. Luo Dan, Dr. Dai Hai Tao, Dr. Wang Guang Hui, Dr. Wu Xuan, Dr. Zhou Jun Qiang, and Dr. Chen Xue Ping. Their insight and wealth of knowledge and stimulating discussions gave a lot of inspiration to my research work. My sincere thanks also go to the rest of NTRC members. Because of them, my graduate study has always been exciting, enjoyable and unforgettable. I would also like to thank the technical staff in Network Technology Research Centre for their kind support and help in the past three years.

Special thanks go to our research group members, Dr. Sun Jian, Dr. Ni Na, Mr. Zu Peng, Mr. Wong Wei Chang and Mr. Chen Li Han for their help and fruitful discussions. I have also made other great friends during my time at Nanyang Technological University. All of them have made life in Singapore more fun and memorable.

Finally, I am deeply grateful to my parents, husband for their love, care and sacrifice for my education. Their understanding, encouragement and never ending support always stimulate me to further efforts. I would also like to thank my dear friend, Dr. Zhao Han Xue, for her help on the completion of this thesis.

Zhang Yifan

July 2012

Summary

Photonic crystal fiber (PCF), also known as holey fiber or microstructure fiber, is characterized by the pattern arrangement of micrometer size air-holes along the length of the fiber. This microstructured waveguide is capable of guiding light by modified total internal reflection or photonic bandgap effect. The existence of the air-holes in the cladding region has opened up opportunities to introduce new materials into the fiber, allowing interactions between light and the hole-material. Because of these abilities, PCF finds their applications in various fields, including fiber-optic communications, fiber lasers, nonlinear devices and highly sensitive gas sensors etc. One specific category of PCF is photonic bandgap fiber (PBGF), which confine light by band gap effects. Recently, the perspectives of PBG active control are further widened, due to the introduction of isotropic (refractive index oil) and anisotropic materials (liquid crystal) into the holey regions of the fibers. In this thesis, the bandgap formation and tunability after the PBGFs are filled with isotropic and anisotropic materials are studied.

This thesis starts with a comprehensive review on the existing optical techniques used in optical fiber sensors. More specifically, the fundamental theory and optical fiber sensing techniques of the conventional optical fibers are reviewed. PCFs are proposed to tackle the disadvantages of conventional optical fibers, such as removing the cladding to enhance the performance. The classification and guiding mechanism of PCFs are also reviewed. Their potential advantages as optical fiber sensors are also discussed.

Following that, the photonic crystal fibers for different sensing applications are investigated experimentally. Different approaches of PCF pressure sensing and

temperature sensing have been investigated. The results are of satisfactory. In addition, the potential of PCF air-holes coating for biomedical sensing is also numerically evaluated.

Infiltrating different materials into the PCF air-holes gain different interesting features. And the interesting features are of great help in sensing applications. The introductions of isotropic material and anisotropic materials into the PCF air-holes are studied as well. The investigation of the anisotropic material mainly focuses on the nematic liquid crystal (NLC). The liquid crystal infiltrated photonic crystal fiber is called photonic liquid crystal fiber (PLCF). The temperature effect of PLCF and the electrical and optical tunabilities of PLCF have been investigated. And the applications of the PLCF have also been studied.

List of Abbreviations

AR	Air Ratio
CMT	Coupled Mode Theory
CNT	Carbon Nanotube
FBG	Fiber Bragg Grating
FPI	Fabry-Perot Interferometer
FSM	Fundamental Space Filling Mode
GOx	Glucose Oxidase
HCPCF	Hollow Core Photonic Crystal Fiber
HF	Hydrofluoric Acid
LC	Liquid Crystal
LCD	Liquid Crystal Display
LPG	Long Period Grating
MI	Michelson Interferometer
MR	Methyl Red
mTIR	Modified Total Internal Reflection
MZI	Mach-Zehnder Interferometer
NLC	Nematic Liquid Crystal
OSA	Optical Spectrum Analyzer
PBE	Photonic Bandedge
PBG	Photonic Bandgap
PBGF	Photonic Bandgap Fiber
PC	Photonic Crystal
PCF	Photonic Crystal Fiber
PLCF	Photonic Liquid Crystal Fiber
PMF	Polarization Maintaining Fiber
PMMA	Polymethyl Methacrylate

RI	Refractive Index
SCPCF	Solid Core Photonic Crystal Fiber
SI	Sagnac Interferometer
SMF	Single Mode Fiber
TEOS	Tetraethyl Orthosilicate
TIR	Total Internal Reflection
TLS	Tunable Laser Source

Table of Contents

Acknowledgments	iii
Summary	v
List of Abbreviations	vii
Table of Contents	ix
List of Figures	xii
Chapter 1 Introduction.....	1
1.1 Motivation and Objectives	1
1.2 Originality of the investigation	3
1.3 Layout of the Thesis	4
Chapter 2 Literature Review	6
2.1 Introduction.....	6
2.2 Optical Fiber Sensing Techniques	7
2.2.1 Grating	11
2.2.2 Interferometry	18
2.3 Photonic Crystal Fiber	29
2.3.1 Modified Total Internal Reflection (mTIR).....	32
2.3.2 Photonic Bandgap Effect (PBG).....	34
2.4 Materials used in PCF Airholes Infiltration.....	39
2.4.1 Liquid Crystal	39
2.4.2 Dyes	44
2.4.3 Other Materials Used	47

2.5	Chapter Summary	50
Chapter 3	Photonic Crystal Fiber for Sensing	52
3.1	Introduction.....	52
3.2	Single Mode Fiber LPG Glucose Sensing	53
3.2.1	Experimental Investigation	55
3.3	PCF LPG for Pressure Sensing	61
3.3.1	Experimental Investigation	63
3.4	PCF for Temperature Sensing.....	70
3.4.1	Theoretical Model and Simulations	71
3.4.2	Experimental Investigation	74
3.5	Refractive Index Sensing Realized by Polymer Coating.....	82
3.5.1	Numerical Analysis and Verification.....	83
3.6	Chapter Summary	93
Chapter 4	Properties of the Photonic Liquid Crystal Fiber	96
4.1	Introduction.....	96
4.2	Effect of External Electrical Voltage on Photonic Liquid Crystal Fiber	97
4.2.1	Electro-optics of Nematic Liquid Crystals	97
4.2.2	Experimental investigation	99
4.3	Effect of Temperature on Photonic Liquid Crystal Fiber	112
4.3.1	Experimental investigation	112
4.4	Chapter Summary	120
Chapter 5	Investigation of the Photonic Liquid Crystal Fiber Optical Modulation	121
5.1	Introduction.....	121
5.2	Liquid Crystal Orientation Realized by Applied Laser Power	123

5.2.1	Introduction.....	123
5.2.2	Experimental investigation	124
5.3	Liquid Crystal Reorientation Realized by Exposusre Time	135
5.3.1	Experimental investigation	135
5.4	Optical Tuning Realized by Irradiation Polarization Angle	141
5.4.1	Experimental investigation	142
5.5	Chapter Summary	156
Chapter 6	Conclusions and Future Works.....	157
6.1	Summary of the investigation	157
6.2	Suggestion of Future Work.....	160
6.2.1	Structure and boundary condition.....	161
6.2.2	Coating of Enzyme	161
6.2.3	Integrate them into microfluidic chip	161
Author's Publications	163
Bibliography	165

List of Figures

Fig 2.1 Components of an optical fiber.	8
Fig 2.2 Snell's Law.....	9
Fig 2.3 Light travel in the optical fiber by total internal reflection	9
Fig 2.4 Setup for phase mask technique	12
Fig 2.5 Light propagation through a FBG fiber.....	14
Fig 2.6 Transmission spectrum of a LPG fiber.....	16
Fig 2.7 Superposition of two waves interference.....	19
Fig 2.8 Fabry-Perot interferometer	20
Fig 2.9 a) Extrinsic FPI; b) Intrinsic FPI	21
Fig 2.10 Mach-Zehnder Interferometer	23
Fig 2.11 Mach-Zehnder interferometer formed by two 3 dB couplers.....	24
Fig 2.12 In-line MZI schemes by a) using two LPGs, b) by offset core, c) collapsing PCF airholes, d) joining MMF and SMF, e) joining small core SMF, f) tapering fiber...	24
Fig 2.13 Michelson Interferometer	25
Fig 2.14 Michelson interferometer formed by 3 dB coupler	26
Fig 2.15 In-line Michelson interferometer.....	26
Fig 2.16 Sagnac Interferometer	27
Fig 2.17 Sagnac Interferometer form by 3 dB coupler	28
Fig 2.18 Structure of conventional fiber and PCF	31
Fig 2.19 a) Solid Core PCF; b) Hollow Core PCF (Crystal Fibre A/S).	32
Fig 2.20 Refractive index profile for a) conventional optical fibers and b) index-guiding photonic crystal fibers.....	34
Fig 2.21 Light guiding mechanism by photonic bandgap effect (hollow core PCF).....	34
Fig 2.22 Microscopic resonance of a photonic crystal fiber.....	35
Fig 2.23 A wave incident on a bandgap material par	37
Fig 2.24 Transmission Spectrum for Photonic Bandgap Fiber.....	38
Fig 2.25 Three types of liquid crystals: a) Nematic, b) Smectic, c) Cholesteric [35-37] ...	41
Fig 2.26 The liquid crystals director defined in the Cartesian coordinates	42
Fig 2.27 Relaxation of a fluorescent dye upon excitation	44
Fig 2.28 Fluorescent dye application in life science[40]	45
Fig 2.29 Trans-cis isomerization of Azo Dye Compounds.....	46
Fig 2.30 Molecules aligned along light polarization direction	47
Fig 2.31 Schematic of the carbon nanotube basic unit. a) High resolution scanning tunneling microscopy image of a helical semiconducting SWNT. b) Multi-walled CNTs [42, 43]	47
Fig 2.32 Single-walled CNT formed by rolling a layer of graphene into a seamless tube[44, 45]	49
Fig 2.33 TEM images of the mesoporous silica nanoparticles with: (a) 20nm, (b) 45nm, (c) 80nm. (d) SEM image of (b) [51].....	50
Fig 3.1 Transmission spectra for different refractive index liquids.....	56
Fig 3.2 Microscope image of sol-gel coated LPG.	57

Fig 3.3 Schematic diagram of experimental setup.....	58
Fig 3.4 Transmission spectra for different glucose concentration.....	60
Fig 3.5 Sensitivity of the wavelength shifts for different concentrations.....	61
Fig 3.6 a) Grooved fixture and experimental setup for the mechanical long period grating; b) (Top View) the relationship between V-groove pitch and optical fiber grating period.	64
Fig 3.7 Transmission dips at 1320 nm for different tilted angles. It shows that the transmission dip shifts to the blue region when tilted angle increases	67
Fig 3.8 Wavelength shifts VS. Tilted angle. The experimental data fits well with the theoretical data.....	68
Fig 3.9 When angle is small, $\Delta\lambda$ VS. tilted angle is in linear relationship	69
Fig 3.10 Cross section of PCF filled with refractive index oil of 1.46 at a) room temperature b) increase of temperature.....	70
Fig 3.11 Relationships between wavelength shifting under different temperature variation for different refractive index liquid are able to get from the plotting of Eq(3.9).	74
Fig 3.12 Schematic diagram of the experimental setup (SC Light Source: Supercontinuum Light Source; OSA: Optical Spectrum Analyzer; PBGF: Photonic Bandgap Fiber (solid core)).....	75
Fig 3.13 Normalized spectra of solid core PBGF with high refractive index liquid infiltration of 1.64, 1.58 and 1.52 under temperature variation as shown in (A), (B) and (C). The highest spectrum at each graph indicated the spectrum at highest temperature, whereas the lowest indicated the spectrum at 24°C. Blue shifting of transmission windows are observed.....	79
Fig 3.14 Wavelength shifts of PBEs plotted as a function of ambient temperature changes.	80
Fig 3.15 PBGF with air holes arranged in triangular lattice.....	83
Fig 3.16 Schematic of cross section and refractive index profile.....	84
Fig 3.17 Gap map for AR = 0 and AR = 0.2.....	86
Fig 3.18 Gap map for AR from 0.7 to 0.9.	87
Fig 3.19 Band map for AR ≤ 0.7	88
Fig 3.20 Gap map with and without filling of biological samples.	90
Fig 3.21 Gap map for filling of biological solution with lower refractive index.....	91
Fig 3.22 Wavelength shift of the falling PBE as a function of biological solution refractive index.....	92
Fig 4.1 Ellipsoid representation of Liquid crystal molecules	98
Fig 4.2 Liquid crystal re-orientation upon voltage application	99
Fig 4.3 Experimental Setup	100
Fig 4.4 Liquid Crystal was infiltrated by capillary force.....	101
Fig 4.5 Transmission spectra of PLCF with different voltage levels	102
Fig 4.6 Rising Bandedge Shifting and simulated LC reorientated angles	105
Fig 4.7 Experimental Setup	105
Fig 4.8 Formation of LPG structure.....	106
Fig 4.9 Transmission Spectrum of PLCF sandwiched between a periodic electrodes ...	106
Fig 4.10 a) Individual LC director axis starts to reorientate if the first threshold meets, inducing twist profile of LCs.	108
Fig 4.11 Shifting of the long period grating transmission dip with the increase of the applied voltage	110

Fig 4.12 Schematic diagram of experimental setup.....	113
Fig 4.13 Transmission spectrum shifting for 1 mm PLCF	116
Fig 4.14 Coordinate system of microscopic order parameter of a nematic liquid crystal molecule.....	117
Fig 4.15 Degree of transmission dip shifting for different PLCF lengths	119
Fig 5.1 Experimental Setup for measuring the optical tuning properties of PLCF in a Sagnac loop.....	125
Fig 5.2 Liquid crystals will be photo-aligned by azo dye (Methyl Red, MR) under the irradiation of Argon ion laser.....	127
Fig 5.3 Molecular structural changes associated with trans-cis isomerization.....	127
Fig 5.4 LC reorientation under the irradiation of linearly polarized laser beam, \vec{E}_{OF} is optical field, β is the original angle between LC director axis and optical field, θ is the reorientation angle	128
Fig 5.5 LC director axis reorientation profile inside the PLCF air holes	129
Fig 5.6 Shifting of the interference spectrum versus the irradiation time of the PLCF under Argon ion laser.....	130
Fig 5.7 Wavelength shifting VS irradiation time of the PLCF under Argon ion laser ...	132
Fig 5.8 Propagation direction of optical field in planar aligned dye-doped LC	132
Fig 5.9 Speed and span of wavelength shiftings for different irradiation power.....	134
Fig 5.10 Transmission power, wavelength shifting vs. time.....	138
Fig 5.11 Wavelength shifting vs. exposure time	139
Fig 5.12 Experimental setup for fabrication of fiber bragg grating holographically.....	143
Fig 5.13 Grating Pitch Calculation	144
Fig 5.14 Simulated Transmission Dip Location for Grating Pitch of 569.868 nm.....	145
Fig 5.15 Transmission bandgap shifting under laser irradiation without beam splitter ...	146
Fig 5.16 Transmission bandgap with beam splitter	147
Fig 5.17 Illustration of relationship between polarizer (45° to fiber axis) and liquid crystal	148
Fig 5.18 Illustration of possible periodic changes in refractive index related to photoisomerization of azobenzene. White strips designate irradiated area (reactive region).....	151
Fig 5.19 Illustration of relationship between polarizer (90° to fiber axis) and liquid crystal	152
Fig 5.20 Illustration of relationship between polarizer (135° degree to fiber axis) and liquid crystal	154

Chapter 1

Introduction

1.1 Motivation and Objectives

Over the past few decades, the use of optical fiber in sensing application has progressed rapidly owing to the numerous advantages provided, such as the fast signal transmission, immune to electromagnetic field, small in size and ability for remote sensing. Furthermore, optical fiber could be multiplexed for measuring temperature, pressure and other parameters simultaneously along the fiber length. In recent year, optical fiber has been applied in biomedical field as it provides invasive way for in vivo measurement. It plays more and more important role in medical diagnostics and more recently, in early detection of potential bioterrorism attacks.

The reason that optical fiber is popular in biochemical sensing is that it is able to provide remote and continuous sensing. It offers long interaction length which is ideal for remote sensing. It can be easily integrated in optical instruments, such as spectrometry. And it can be used as a platform for different sensing techniques, such as Surface Plasmon Resonance or Raman spectroscopy. Thanks to its flexibility, the configuration of the sensing scheme can be customized for certain applications.

However, to be used for biochemical sensing, the fiber has to be pre-treated to enhance

the sensitivity. It is because most of the sensing schemes are depended on the evanescent wave interaction between the optical field near the fiber core and the sensing layer deposited on the fiber surface. The strength of the evanescent wave is inversely proportional to the fiber diameter. Thus to enhance the interaction, the cladding of the fiber has to be removed by immersing in strong acid or polishing the surface manually. The fiber will become very fragile to handle after the pre-treatment. In addition, the light coupling efficiency will be affected dramatically especially in fluorescent spectroscopy as the coupling of the fluosphore emission from the surface to the fiber becomes very weak. Recent years, there emerges a new category of optical fibers, photonic crystal fiber (PCF). PCF is characterized with a periodically arranged air holes running through the entire length of the fiber. The introduction of PCF attracts much attention owing to its unique waveguide feature. PCFs were mainly used for telecommunication application upon its invention. In the past few years, they have been adopted in sensing applications to overcome the limitations of conventional optical fibers. Owing to the unique feature of PCF, samples can be infiltrated into the airholes of PCF. Thus the interaction between the analyte and the optical field could be improved. And it eliminates the pre-treatment compared to the conventional optical fiber. Another advantage using PCF is that besides total internal reflection (TIR), light can be guided by photonic bandgap (PBG) effect, which is characterized as having several transmission windows. The transmission windows are sensitive to the surrounding refractive index. Thus it provides opportunity for optical tuning.

The objectives of the thesis are to apply PCF as sensing transducers that convert the changes of physical parameters to the change of transmission spectrum. An important issue is to investigate the materials of PCF airholes infiltration and the tuning opportunities that could be achieved by the infiltration. This is worth to be investigated as it could be integrated in the future design of the biochemical sensing schemes. The investigations provide prototypes for the design of the future PCF based biochemical sensors.

1.2 Originality of the investigation

The main original works in this thesis may be summarized as follows:

1. Experimental demonstration for glucose concentration sensing by sol-gel coating technique on optical fiber.
2. Experimental investigation and demonstration of the PCF mechanical pressure sensing.
3. Theoretical analyses and experimental demonstration of PCF PBG temperature sensing.
4. Theoretical analyses of polymer coating in solid-core PCF for refractive index sensing.
5. Experimental investigation and demonstration of electrical tuning on PLCF.
6. Experimental investigation and demonstration on the temperature effect on PLCF.

7. Experimental investigation and demonstration of the optical tuning properties of PLCF and the corresponding effects.
8. Experimental demonstration of the polarization effects on the transmission bandgap of the PLCF by changing of the polarization angle of input light.

1.3 Layout of the Thesis

This thesis is organized as follows:

1. Chapter 2 overviews the research background. After reviewing various optical techniques used in optical fiber sensors, the most widely studied materials for integrating with PCF are reviewed. Unique features of the PCFs, which make them very attractive for optical fiber sensing applications, are discussed.
2. Chapter 3 introduces the sensing application carried out using PCFs. Different sensing schemes by using PCFs and the different light guiding mechanisms used are presented. Theoretical explanations are also described.
3. Chapter 4 investigated the electrical properties of PLCF. The temperature effects on the PLCF are also investigated. Different experimental setups are employed and optimized for investigating the tuning properties.
4. Chapter 5 focused on the optical tuning properties of PLCF which is achieved by doping additional organic material inside the fiber. In particular, the effects on the transmission bandgap have been demonstrated.

5. Chapter 6 summarized the investigations and some future work recommendations are suggested.

Chapter 2

Literature Review

2.1 Introduction

Optical fiber based sensors are renowned for their usage in harsh environments such as offshore oil-platform structural monitoring area. There are other advantages to develop optical fiber as a sensor. Optical fiber sensors are small in size, and required no electrical power input at the sensing site. Furthermore different transducers can be multiplexed along the fiber length so that different parameters such as strain, temperature and pressure can be measured by optical equipment simultaneously[1].

Photonic crystals (PCs) are periodically structured electromagnetic materials. They have attracted tremendous interests owing to their ability of molding and controlling the electromagnetic waves propagation. Generally, the flow of light in the material depends on the wavelength and its incident angle. The periodic structures can form photonic bandgap to confine light in their transmission band and prevent light from propagating in specific range of frequency [2, 3]. The amazing example of PCs occurring naturally is the beautiful wings of the butterflies. These characteristics create a new era in the field of photonics and a wide range of applications have been invented such as photonic crystal fibers (PCFs) [3].

Photonic crystal fibers (PCF) are a special type of optical fibers. Since the invention of PCFs, researchers have toyed with the idea of varying the air-holes arrangement in the cladding or infiltrating the micro capillaries with different materials such as gases, index matching oils, fluorescent dyes. The purpose is to create guided wave structures for the entrapment of light in silica by exploiting the full capability of PCF. This has led to the possibility of photonic bandgap tuning as well as switching between two different wave guiding mechanisms, the modified total internal reflection or the photonic band gap effect.

In this chapter, the mostly used techniques in optical fiber sensing are described in Section 2.2. The brief introduction of photonic crystal fiber and its light guiding mechanism are presented in Section 2.3. Mostly used materials for PCF air-holes infiltration are introduced in Section 2.4. A Chapter Summary is described in Section 2.5

2.2 Optical Fiber Sensing Techniques

An optical fiber is a rod-like waveguide that guides light along its longitudinal direction. It consists of a higher refractive index core and lower refractive index cladding. Usually the optical fiber consists of three components, core, cladding and coating/buffer as shown in Fig. 2.1. The core and cladding are typically made of silica or polymer with different composition to achieve higher refractive index in core and lower refractive index in cladding. Coating is usually made of Acrylate to protect the core and cladding from breaking.

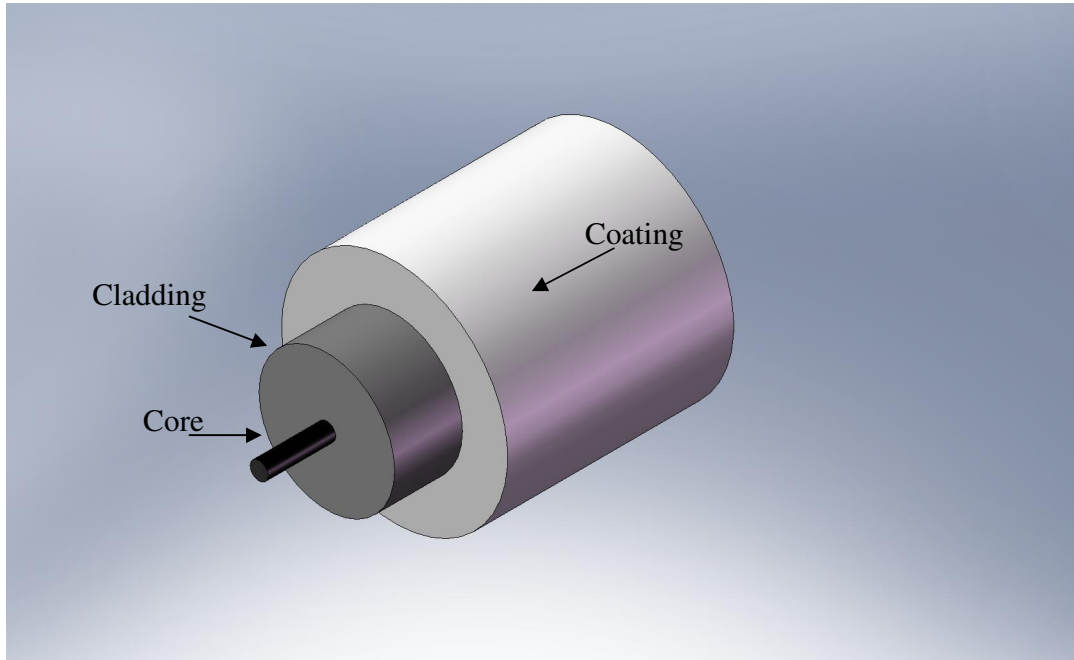


Fig 2.1 Components of an optical fiber.

As shown in Fig. 2.2, when light comes across a boundary with different refractive indices, it will be divided into two rays, reflected ray and refracted ray. The angle of the refracted ray θ_2 is of relationship between two refractive indices (n_1 and n_2) and the angle of the incident light according to Snell's Law,

$$n_1 \sin \theta_1 = n_2 \sin \theta_2 \quad (2.1)$$

where θ_1 is the angle of incidence. If the angle of incidence is greater than a critical angle ($\theta_c = \sin^{-1} \frac{n_2}{n_1}$), the light will experience total reflection instead of refraction.

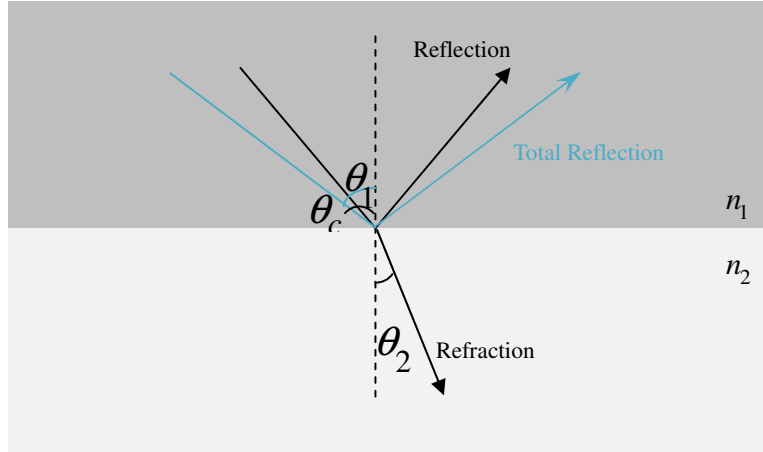


Fig 2.2 Snell's Law

In the optical fiber structure, light is guided by total internal reflection as shown in Fig 2.3. Light that is not guided by total internal reflection will be refracted to the cladding region and attenuate after travelling for certain distance along the optical fiber.

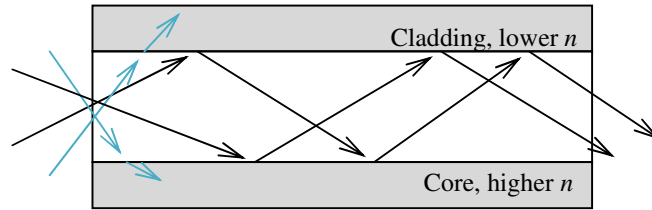


Fig 2.3 Light travel in the optical fiber by total internal reflection

The mode field in the fiber cross section can be expressed as

$$\mathbf{E}(x, y, z) = \mathbf{e}(x, y)e^{i\beta z} \quad (2.2)$$

$$\mathbf{H}(x, y, z) = \mathbf{h}(x, y)e^{i\beta z} \quad (2.3)$$

where β is the propagation constant and $\mathbf{e}(x, y)$ and $\mathbf{h}(x, y)$ are the translational invariant part of the modal fields in x, y, z direction.

Usually the transverse components of $\mathbf{e}(x, y)$ and $\mathbf{h}(x, y)$ can be determined by the

longitude components e_z or h_z by the following,

$$\mathbf{e}_t = \frac{i}{n^2 k^2 - \beta^2} \left\{ \beta \nabla_t e_z - \left(\frac{\mu_o}{\epsilon_o} \right)^{1/2} k \hat{\mathbf{z}} \times \nabla_t h_z \right\} \quad (2.4)$$

$$\mathbf{h}_t = \frac{i}{n^2 k^2 - \beta^2} \left\{ \beta \nabla_t h_z - \left(\frac{\epsilon_o}{\mu_o} \right)^{1/2} k n^2 \hat{\mathbf{z}} \times \nabla_t e_z \right\} \quad (2.5)$$

e_z or h_z (represented by Ψ) satisfy the longitudinal field equations as following,

$$(\rho^2 \nabla_t^2 + U^2) \Psi = 0 \quad \text{for } 0 \leq r < \rho \quad (2.6)$$

$$(\rho^2 \nabla_t^2 - W^2) \Psi = 0 \quad \text{for } \rho \leq r < \infty \quad (2.7)$$

where r is the transverse direction in the fiber cross section, ρ is the core radius, ϵ is the permittivity, μ is the permeability, $U = \rho \{ (k n_{co})^2 - \beta^2 \}^{1/2}$ and $W = \rho \{ \beta^2 - (k n_{cl})^2 \}^{1/2}$.

Optical fiber sensors are devices which make use of optical field to detect the change of light transmission due to external parameters. The mode field changes accordingly upon the light transmission changes. Optical fiber has been used to detect inorganic ions for pH measurement, gas detection and etc [4]. It can also be used as an intrinsic optical fiber sensor for nerve agent sensing [5]. The coating of the optical fiber is usually being stripped away. The cladding of the fiber is generally removed or taped to have better sensitivity.

Beside direct detections, fiber grating techniques and interferometries are the mostly used structures in optical fiber sensors. These two techniques will be introduced in the

following session.

2.2.1 Grating

One of the standard methods for studying the grating effect in optical fibers is coupled-mode theory (CMT). In CMT, forward- and backward- propagating waves are treated separately in non-grating region. The coupling among them happens at the grating structure. These modes can be expressed by coupled-mode equations [6]

$$\frac{dR}{dz} + j[k_{dc} + \sigma - \frac{1}{2} \frac{d\phi}{dz}]R = -jk_{ac}^* S \quad (2.8)$$

$$\frac{dS}{dz} - j[k_{dc} + \sigma - \frac{1}{2} \frac{d\phi}{dz}]S = jk_{ac} R \quad (2.9)$$

where R is the backward-propagating mode, S is the forward-propagating mode, z is the position along the grating region, $j = \sqrt{-1}$ and $d\phi/dz$ signifies the rate of the grating phase change. For a constant grating period, $d\phi/dz = 0$. And σ is a weighting factor, which measures the power exchange speed between the polarization field and the generated field. It can be defined by the propagation constant β and the grating period Λ as

$$\sigma = \beta - \frac{\pi}{\Lambda} \quad (2.10)$$

k_{dc} and k_{ac} are the coupling constant, which can be defined as

$$k_{dc} = \frac{2\pi}{\lambda} \overline{\delta n_{eff}} \quad (2.11)$$

$$k_{ac} = k_{ac}^* = \frac{\pi}{\lambda} v \overline{\delta n_{eff}} \quad (2.12)$$

where v is the fringe visibility of the refractive index modulation, $\overline{\delta n_{eff}}$ is a constant for uniform grating.

The amplitude reflection coefficient is defined as [7]

$$\rho = \frac{S(0)}{R(0)} = \frac{-k_{ac} \sinh(\alpha L)}{\delta \sinh(\alpha L) - j\alpha \cosh(\alpha L)} \quad (2.13)$$

where L is the grating length,

$$\delta = k_{dc} + \sigma - \frac{1}{2} \frac{d\phi}{dz} \quad (2.14)$$

and

$$\alpha = \sqrt{|k_{ac}|^2 - \delta^2} \quad (2.15)$$

There are various techniques for fabricating fiber gratings. One of the commonly used techniques is the phase mask technique. The setup is shown in Fig 2.4.

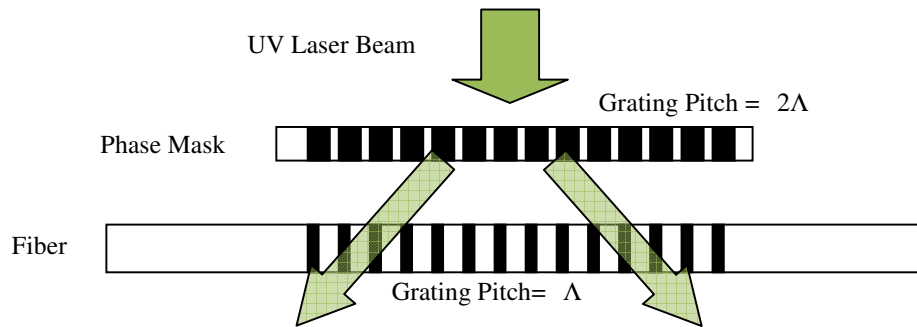


Fig 2.4 Setup for phase mask technique

The UV laser beam is projected normally on the phase mask and diffracted into several beams. The two first-order diffracted beams interfere on the fiber surface and form a periodical pattern with grating period one-half of the phase mask period. The main

advantage for phase mask technique is that the requirement for the UV laser beam on temporal and spatial coherence is not as stringent as other techniques.

In the recent years, high quality in-fiber gratings have been successfully made by exposing Germania-doped fibers to ultra-violet light. These gratings reflect light at a certain wavelength band. Asseh, et al. [8] presented a refractive index sensor using Bragg grating which uses the spectral response of the gratings as the sensing mechanism. Subsequently, Bhatia et al. [9] presented a chemical sensor based on long period gratings (LPGs). LPGs can couple light from the fiber core to the cladding, which allows direct quantitative chemical measurements of the medium surrounding the fiber cladding.

This section describes the operations of fiber Bragg gratings (FBGs) and long period gratings (LPGs). It also presents how FBGs and LPGs can be used as the main transducer components for signal processing applications.

2.2.1.1 Fiber Bragg Gratings (FBGs)

A fiber Bragg grating (FBG) is a periodic variation of the refraction index along the fiber axis with grating pitch in the order of hundreds of nanometers. The grating acts as a band rejection filter reflecting wavelengths that satisfy the Bragg condition and transmitting the others. In the last few decades, many groups in worldwide realized that by UV laser writing, high quality gratings in the core of photosensitive optical fibers could be achieved. During irradiation, a refractive index modulation (index grating) is formed with

the same spatial periodicity as the writing interference pattern. This refractive index grating acts as a distributed reflector that couples the forward propagating to the backward propagating light beam.

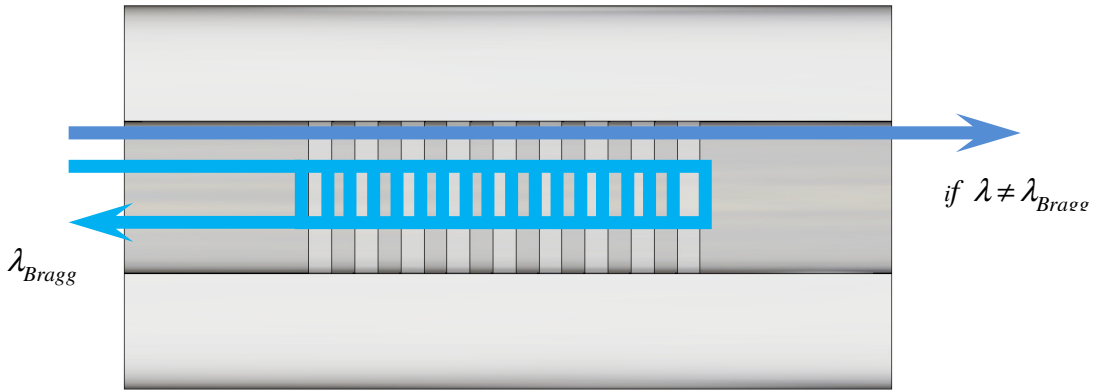


Fig 2.5 Light propagation through a FBG fiber

The wavelength, for which the incident light is reflected with maximum efficiency λ_{Bragg} , is called the Bragg resonance wavelength. The equation relating the grating spatial period and the Bragg wavelength depends on the effective index of the transmitting medium, n_{eff} , and grating period Λ is given by:

$$\lambda_{Bragg} = 2n_{eff}\Lambda \quad (2.16)$$

Both the grating period and refractive index of the surrounding medium vary according to the temperature and the applied strain, thus the Bragg wavelength varies in proportion to the changes of these parameters[10]. If designate the external parameter as X , where X can be temperature, strain, pressure or the cladding refractive index. The change of the Bragg wavelength due to the change of external parameter is [10]:

$$\Delta\lambda_{Bragg} = \lambda_{Bragg} \left(\frac{\delta n_{eff}}{n_{eff}} + \alpha \right) \Delta X \quad (2.17)$$

where $\delta n_{eff} / n_{eff}$ is the normalized sensitivity of the effective index of the mode, and α is the coefficient of physical length change due to the parameter X .

Most journal articles have included the exploitation of the FBGs sensitivity to strain and temperature. To use FBG as refractive index sensing, removal of the cladding is essential to increase the evanescent field interaction with the surrounding environment. Studies have proved that by performing chemical etching on the grated region of the optical fiber, the evanescent field from the core is able to penetrate more into the surrounding medium [11]. Hence, the fiber with smaller diameter core can lead to enhanced sensitivity, because most of the light is in the fiber fundamental mode. A.Asseh et al [8] developed a highly sensitive evanescent field FBG sensor which leads to a detectable change of 3.5×10^{-5} in the refractive index of a salt solution sample. And the sensitivity of the FBG sensor was found to be 282 nm/RIU. In comparison, other authors had previously measured a sensitivity of 7.3 nm/RIU[8] and 2.66 nm/RIU [12] in less aggressively etched fiber Bragg sensors.

2.2.1.2 Long Period Gratings (LPGs)

A Long Period Gratings (LPGs) is a periodic modulation of refractive index in a fiber core with the period on the scale of hundreds of micrometers. For a single-mode fiber, when a broadband light passes through the LPG, narrow light bands centered at certain

wavelengths are coupled with the forward propagating radiation modes as shown in Fig

2.6. The phase mis-match induced by LPG is

$$\Delta\beta = \beta_{clad} - \left(\beta_{core} + \frac{2\pi N}{\Lambda} \right) \quad (2.18)$$

where $\beta_{core} = \frac{2\pi n_{eff}}{\lambda}$, $\beta_{clad} = \frac{2\pi n_{clad}}{\lambda}$ and Λ is the grating period. The phase matching condition is met when $\Delta\beta = 0$. These cladding modes decay rapidly as they propagate along the fiber owing to the cladding-core interface, resulting in the LPG transmission spectrum.

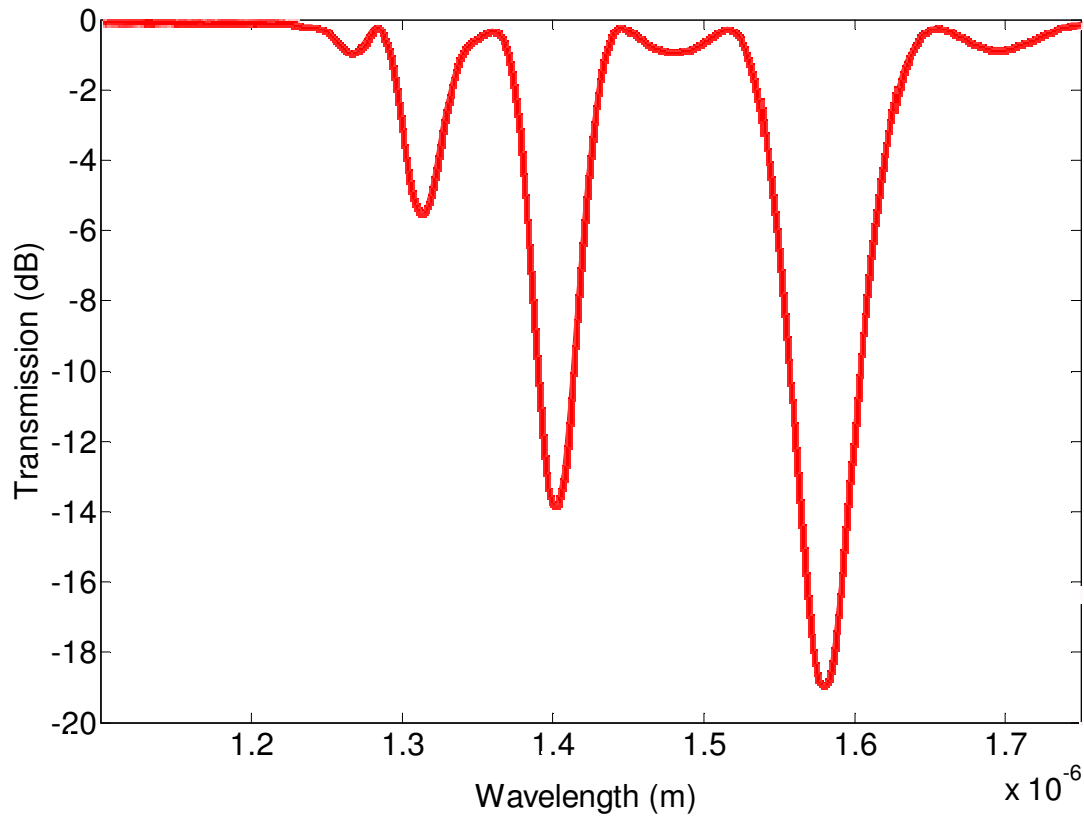


Fig 2.6 Transmission spectrum of a LPG fiber

Fig 2.6 shows the transmission spectrum plot of a LPG fiber. There are few discrete

resonance bands (or transmission dips) in the plot. Due to the modal overlaps on the dissimilar coupling coefficients, there are different peak loss value and bandwidth in the transmission bands. The minima peak corresponds to the phase matching between the guided core mode and forward propagating cladding modes. The grating period for the particular LPG is 450 μm . The ambient refractive index can be measured by tracking the wavelength shift on the highest resonant band. The wavelength and the width of the transmission dip can be custom-made during the grating fabrication process, so that the sensors can be used at a desirable operating wavelength.

LPG sensors are usually more sensitive than FBG sensors owing to the fact that they are based on the effective index difference between the guided mode and cladding modes. Any change in the cladding mode effective index will have a large impact on the mode coupling.

LPG was first demonstrated as a spectrally selective band rejection in the telecommunication industry in year 1995. After then, LPGs have also been designed for strain, temperature, and refractive index sensing[9]. Shortly after, H.Patrick et al. [13] analyzed and experimentally tested the LPGs response to external refractive index and demonstrated a LPGs chemical sensor.

LPG can be used for biosensing as well. The main disadvantage of the LPG biosensor is that the sensing transducer is sensitive to temperature and strain. The sensitivity is around 0.04-0.15 nm/ $^{\circ}\text{C}$, depending on the type of optical fiber used[14]. LPG is also sensitive to

bending strain. When the LPG is bent, the transmission spectrum changes considerably.

In worst case, the peaks in the spectrum completely disappear.

2.2.2 Interferometry

Interference occurs when two or more waves overlap to form an interference pattern. In order to have the two waves generate a stable interference pattern with each other, they must be coherence. The resulting irradiance at certain point of the interference will be the superposition of the two waves as shown in Fig 2.7. It is the time average of the squared electric field intensity.

$$I = \langle \overline{E^2} \rangle_T \quad (2.19)$$

where E is the light field intensity

$$\overline{E^2} = (\overline{E_1} + \overline{E_2}) \cdot (\overline{E_1} + \overline{E_2}) = \overline{E_1^2} + \overline{E_2^2} + 2\overline{E_1 \cdot E_2} \quad (2.20)$$

thus

$$I = \langle \overline{E_1^2} \rangle_T + \langle \overline{E_2^2} \rangle_T + 2\langle \overline{E_1 \cdot E_2} \rangle_T \quad (2.21)$$

For

$$\langle \overline{E_1^2} \rangle_T = \frac{E_{01}^2}{2} = I_1 \quad (2.22)$$

$$\langle \overline{E_2^2} \rangle_T = \frac{E_{02}^2}{2} = I_2 \quad (2.23)$$

$$\langle \overline{E_1 \cdot E_2} \rangle_T = \frac{1}{2} \overline{E_{01} \cdot E_{02}} \cos \delta = 2\sqrt{I_1 I_2} \cos \delta \quad (2.24)$$

The irradiance becomes

$$I = I_1 + I_2 + 2\sqrt{I_1 I_2} \cos \delta \quad (2.25)$$

where δ is the phase difference between the initial and the combined path.

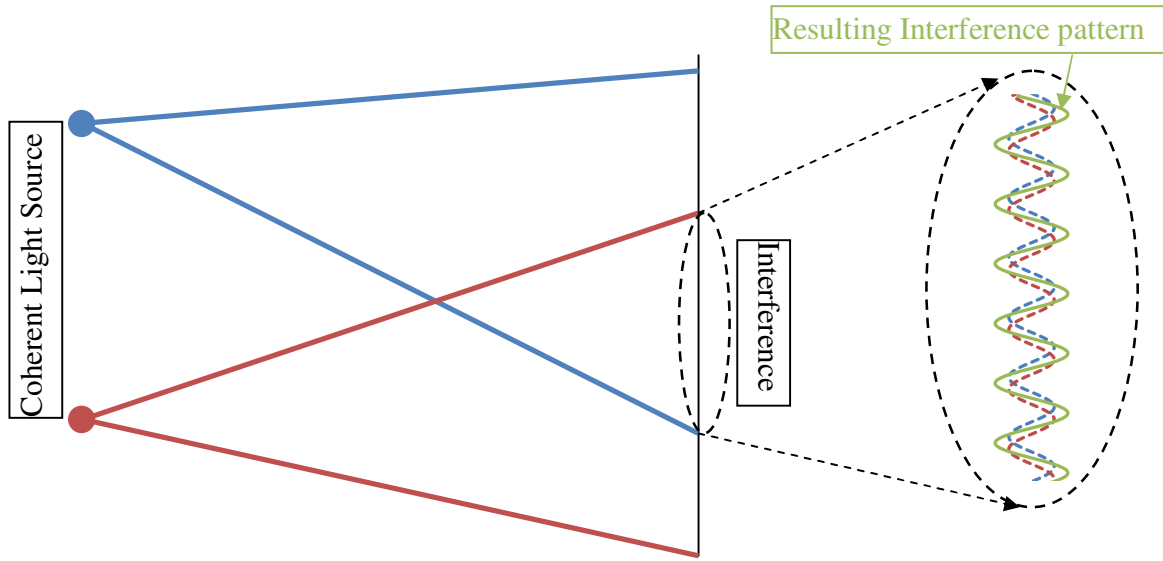


Fig 2.7 Superposition of two waves interference

Optical interferometry, which operates based on interference of one or more light beams, is one of the compact and sensitive measurement systems for external changes such as temperature, pressure, strain and others [15]. It offers various advantages like high sensitivity, high resolution and large dynamic range [15].

There are many types of interferometers to achieve interferometric-based measurements. The following introduces four types of commonly-used primary sensing element of optical interferometry: Fabry-Perot interferometer, Michelson interferometer,

Mach-Zehnder interferometer and Sagnac interferometer.

2.2.2.1 Fabry-Perot Interferometer (FPI)

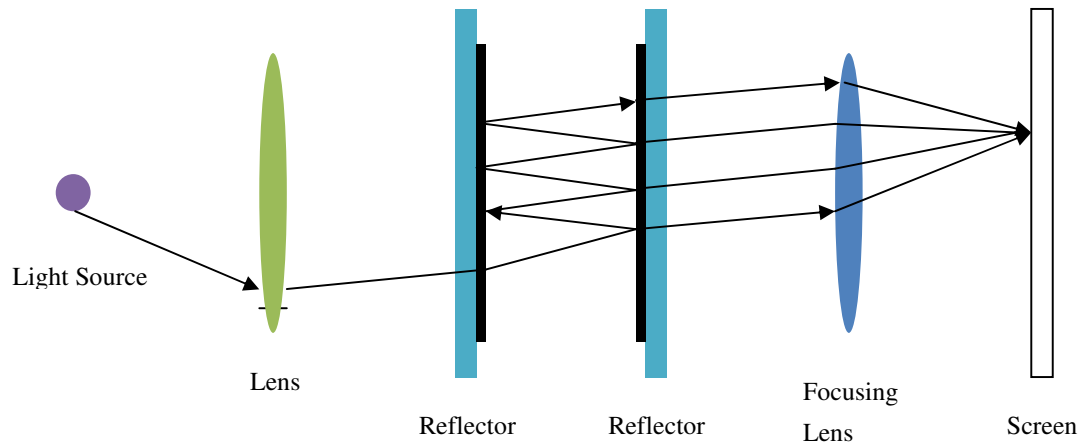


Fig 2.8 Fabry-Perot interferometer

FPI is based on two-beam interference created by two signals which are reflected by two reflectors. Usually the reflector is made of partially reflective glass (or half-silvered mirror). The two reflected surface face with each other. The light from light source is multiply reflected by the two reflectors. The multiple transmitted beams are collected by the focusing lens and interfere at the screen as shown in Fig 2.8.

In optical fiber, the FPI can be formed extrinsically or intrinsically as shown in Fig 2.9. The fabrication of extrinsic FPI in optical fiber is relatively simple. However the coupling efficiency is low. The extrinsic FPI has the merit of sensing the displacement variation owing to the fact that the phase difference can be influenced directly by the change of the external reflection surface displacement. It has been widely implemented in pressure

sensors with the extrinsic configuration[16].

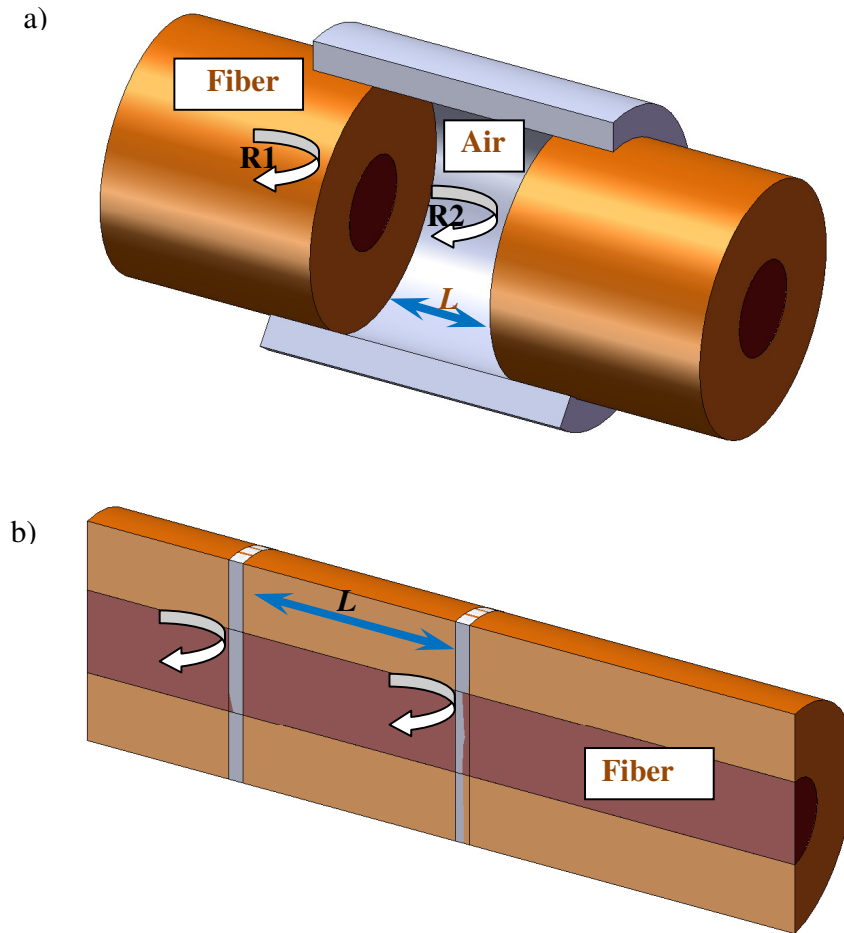


Fig 2.9 a) Extrinsic FPI; b) Intrinsic FPI

As shown in Fig 2.9 above, multiple light reflections caused by the two reflectors along the fiber interfere with each other. If the transmitted beams are in phase, constructive interference is induced which corresponds to the peak in the transmission spectrum. If they are out-of-phase, the interference is destructive. It corresponds to the transmission minimum.

In general the intensity of incident wave is the sum of the transmittance (T) and

reflectance (R). That is

$$T + R = 1 \quad (2.26)$$

The ratio of the transmitted and the incident beam irradiance is given by

$$\frac{I_t}{I_i} = \frac{T^2}{1 + R^2 - 2R\cos\delta} \quad (2.27)$$

where δ is the phase difference. The phase difference for the FPI is given by:

$$\delta_{FPI} = 2L \frac{2\pi}{\lambda} n \quad (2.28)$$

where λ is the incident light beam wavelength, n is the material refractive index in the cavity or the cavity mode, and L is the length of the cavity. Any change of the external parameters will induce the variation of the optical path length difference, resulting the phase difference of the FPI.

2.2.2.2 Mach-Zehnder Interferometer (MZI)

In Mach-Zehnder interfereometer, light beam from the light source is split by a beam splitter as shown in Fig 2.10. The two resulting beams are reflected by reflective mirror and pass through a second beam splitter before enter two detectors

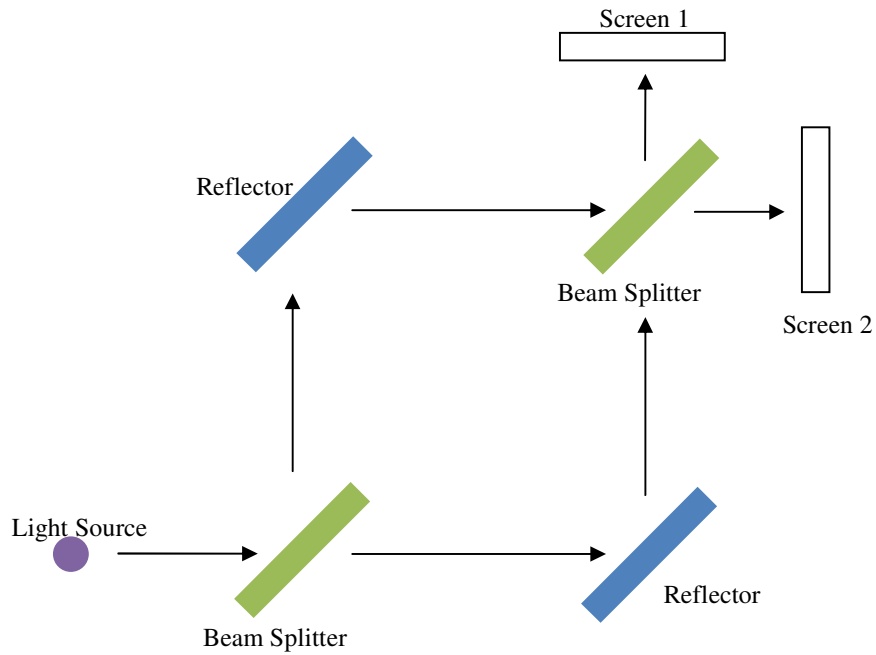


Fig 2.10 Mach-Zehnder Interferometer

In optical fiber, MZI can be formed by joining two 3-dB couplers as shown in Fig 2.11. The light from the light source is split into two in coupler 1 and recombined in coupler 2. MZI can also be formed with different in-line schemes shown in Fig 2.12. No matter which setup is used for the MZI, the two resulting beams should be in the same phase if there is no obstruction. However, the phase shifts if any one of the light path length changes caused by external parameter. Thus the relative phase shift could be determined.

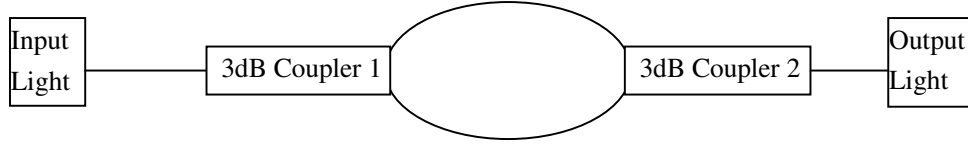


Fig 2.11 Mach-Zehnder interferometer formed by two 3 dB couplers

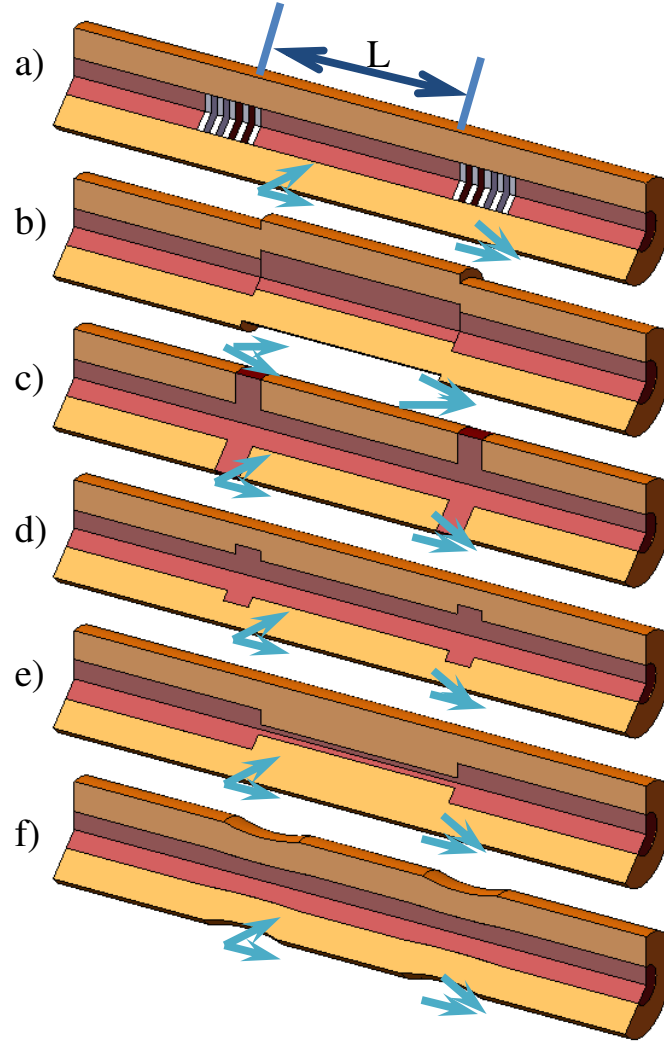


Fig 2.12 In-line MZI schemes by a) using two LPGs, b) by offset core, c) collapsing PCF airholes, d) joining MMF and SMF, e) joining small core SMF, f) tapering fiber

The phase difference is given by[17]:

$$\frac{2\pi}{\lambda}[n_{eff}^{co} - n_{eff}^{cl,i}]L = (2N + 1)\pi \quad (2.29)$$

where n_{eff}^{co} and $n_{eff}^{cl,i}$ are the effective index of the core and the i -th order cladding mode.

N is an integer.

2.2.2.3 Michelson Interferometer (MI)

The Michelson interferometer is similar to Mach-Zehner interferometer. The difference is that there is only one beam splitter in the setup. The two resulting light beams are reflected back to the same beam splitter and generate interference which is visible to the detector shown in Fig 2.13.

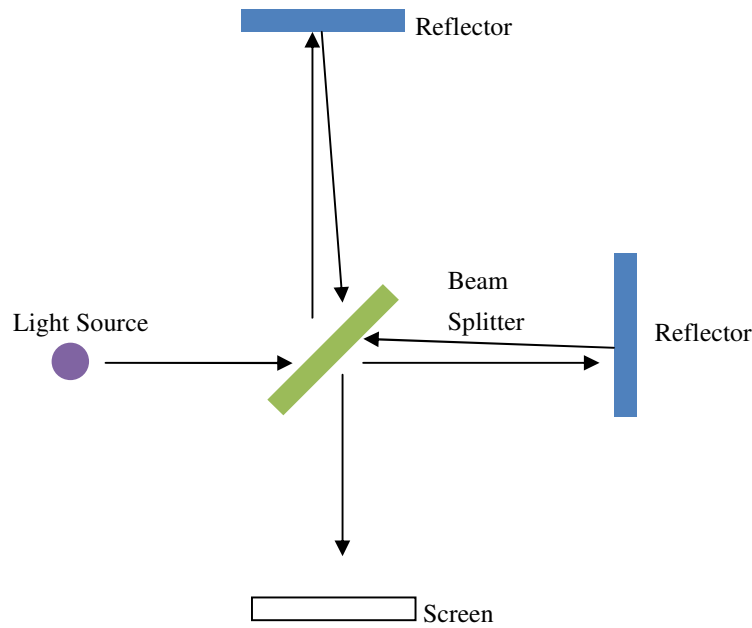


Fig 2.13 Michelson Interferometer

A MI is like a half of an MZI in optical fiber configuration shown in Fig 2.14. The main difference is the mirror at the back of the setup to reflect back the light. MIs are generally more compact for practical usage. However, the fiber length difference between the two

arms of the coupler must be within the light source coherence length, which is same for the in-line scheme.

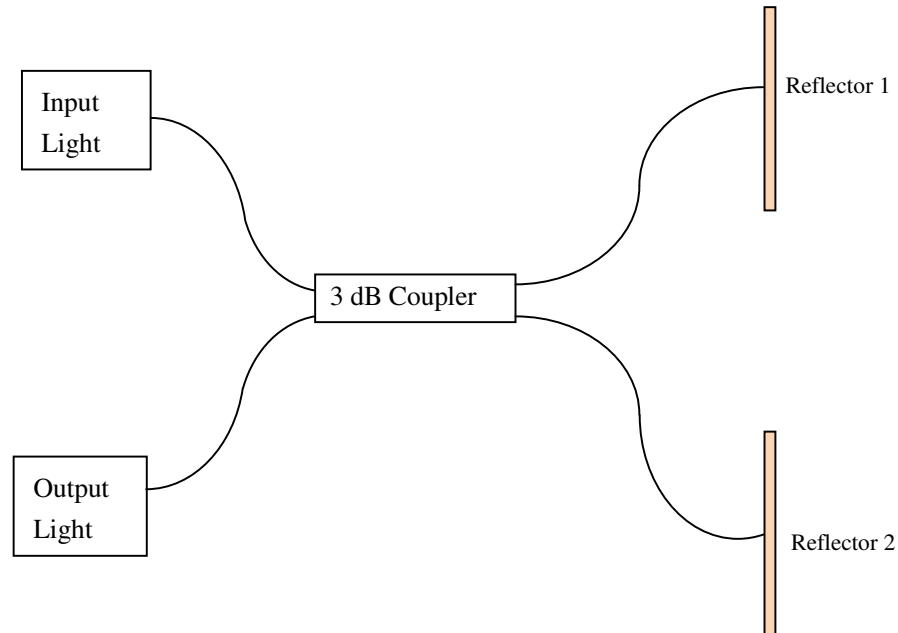


Fig 2.14 Michelson interferometer formed by 3 dB coupler

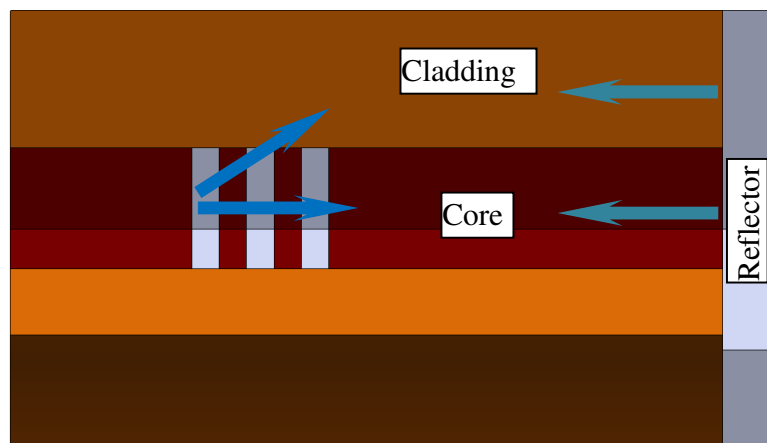


Fig 2.15 In-line Michelson interferometer

2.2.2.4 Sagnac Interferometer (SI)

Sagnac interferometers are of great interest in various sensing applications owing to their

simple structure and easy fabrication. In Sagnac interferometer, light is separated by beam splitter. The resulting light beams travel in an enclosed trajectory and return to the beam splitter as shown in Fig 2.16. And the location of the interference fringes depends on the light travelling speed during the rotation.

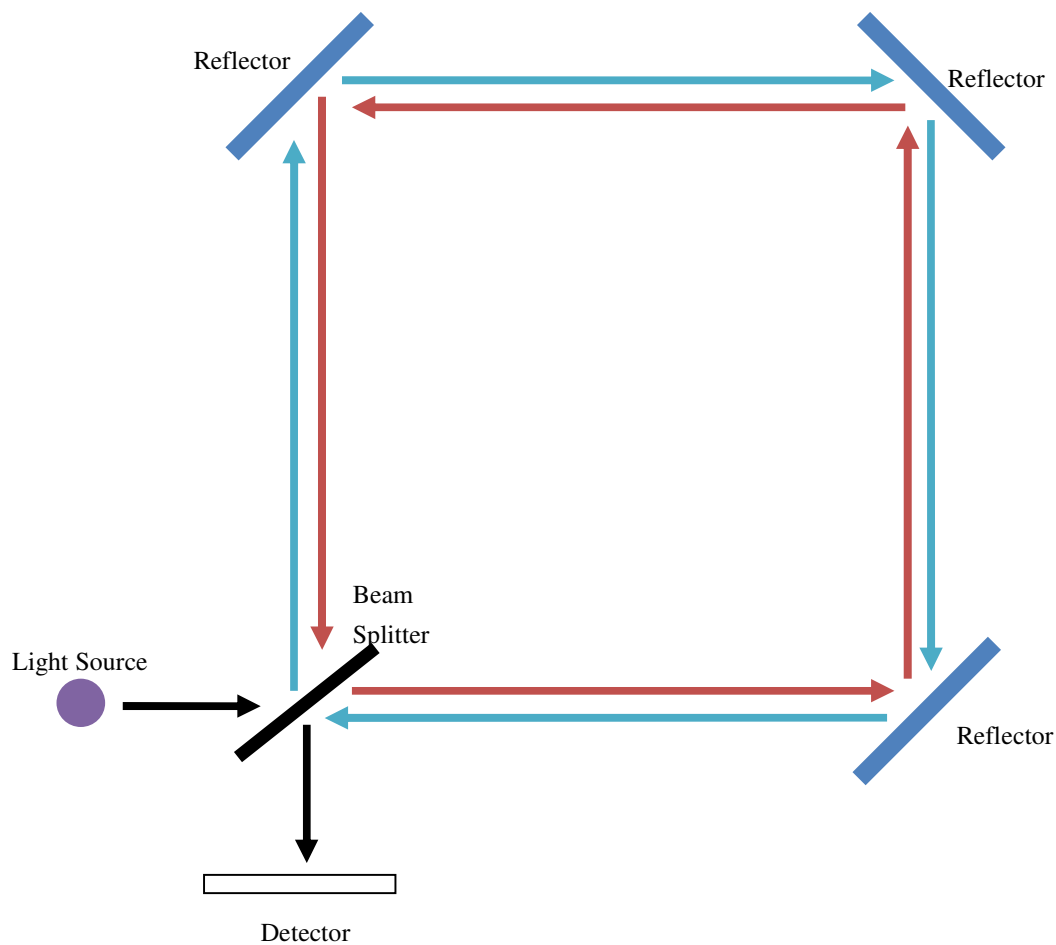


Fig 2.16 Sagnac Interferometer

In optical fiber, Sagnac interferometer is formed by joining a section of birefringent fiber and the two arms of a 3 dB coupler shown in Fig 2.17. The light from light source is split into two beams. They travel in counter directions with different polarization states and join again in the coupler.

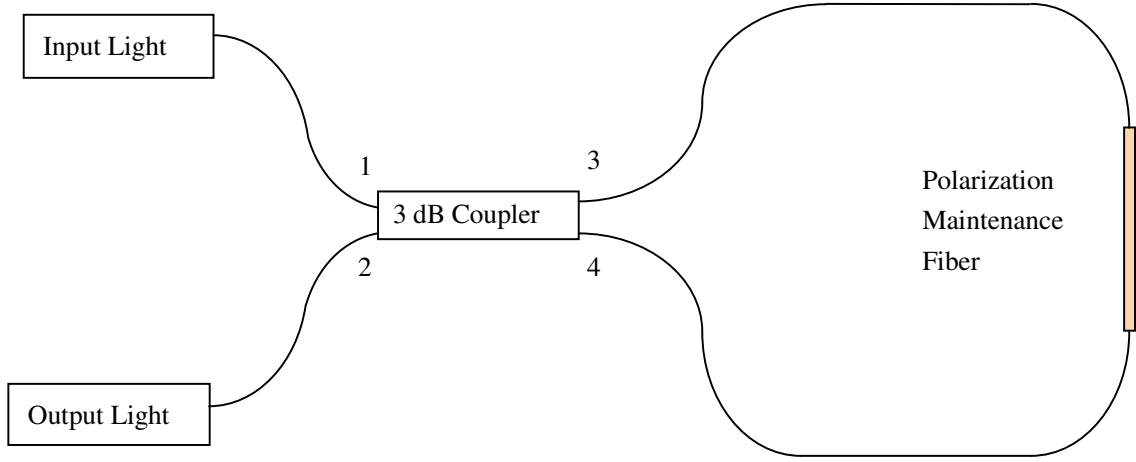


Fig 2.17 Sagnac Interferometer form by 3 dB coupler

The light split at point 3 and 4 in Fig 2.17 by the 3-dB coupler is[18]

$$E_3 = \sqrt{\frac{1}{2}} E_{in} \quad (2.30)$$

$$E_4 = \sqrt{\frac{1}{2}} H E_{in} \quad (2.31)$$

where H is the phase delay matrix. It is given by

$$H = \begin{bmatrix} e^{i\frac{\pi}{2}} & 0 \\ 0 & e^{i\frac{\pi}{2}} \end{bmatrix} \quad (2.32)$$

The transmittivity T and the reflectivity R are

$$T = [\sin(\theta) \cos(\frac{\beta}{2})]^2 \quad (2.33)$$

$$R = 1 - T \quad (2.34)$$

where $\beta = -\frac{2\pi}{\lambda} BL$ is the phase of interference. It is the function of birefringent coefficient B and length of the birefringent fiber L . θ is the clockwise propagating light

polarization state rotation angle when it enters the birefringent fiber.

Eq(2.33) indicates that unlike other interferometers, the phase difference in Sagnac interferometer is determined by the polarization state of the mode guided along the loop. Thus high birefringent optical fiber is generally used at the sensing part to acquire high phase sensitivity.

A Sagnac interferometer has shown many advantageous characteristics such as low insertion loss, independence of input polarization, large spectral bandwidth and high resistance to environmental changes resulting from the two counter-propagating light beams that travel along a common path [19]. It also has a strong noise rejection ability which is very useful in signal stabilization [16].

The strong temperature dependency of Sagnac interferometer may be a great advantage for using as temperature sensor. However, it might depreciate its sensing ability in other sensing applications. The introduction of photonic crystal fiber (PCF) can overcome the problem as PCF is made of pure silica.

2.3 Photonic Crystal Fiber

Photonic crystals are optical compounds that the refractive indexes are varies periodically and are able to manipulate the propagation of electromagnetic waves. It employs a periodic arrangement of low index material (typically air-holes) surrounding by high index background (silica). The high refractive index contrast between the silica and air

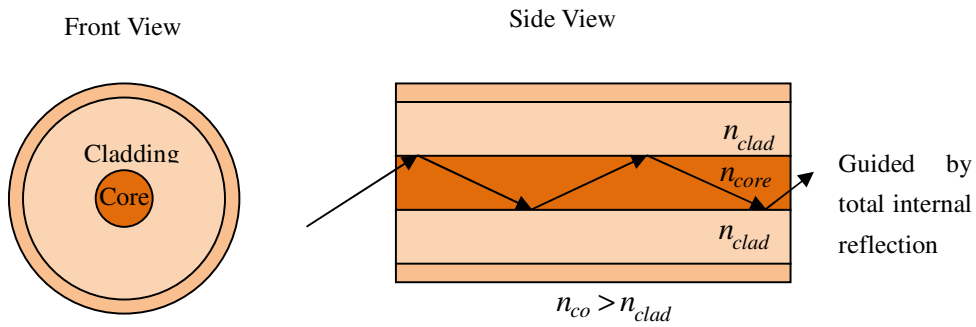
inside the cladding engenders unique optical properties which in turn improves the abilities of controlling the propagation of light. In addition, the optical properties of PCFs are sensitive to the dimension or position of the air holes in the fiber cross-section. Due to its high design flexibility, the light dispersion and nonlinear properties can be contrived and successfully used in various aspects.

The most important milestone in studying photonic crystal structure occurs in 1987. Two physicists, Eli Yablonovitch and Sajeev John co-invented the concept of photonic crystals band gap. They intended to construct a particular structure, which can block all the incoming lights from the selected wavelengths while allowing the passing of other electromagnetic waves [20]. In 1991, Philip Russell and his group proposed the new ideas of fiber which was originally known as “holey fiber”, a fiber based on the concept of having with a periodic arrangement of microstructured holes along fiber path by entrapping the light within the fiber core [21]. The emergence of PCF stimulated the curiosity of researchers in using single type of material for fabricating fibers. Philip Russell completed the first credible PCF structure drawing with his research group in year of 1995. The hexagonal structure is makes up of a densely filled arrangement of little air holes which is defectless and flawless[22].

Since PCFs were first reported by Philip St J. Russell, researchers became interested in photonic crystal structure for the purpose of obtaining a better way than the conventional fiber for transmitting the data. The mechanisms for both conventional fibers and solid

core PCFs are shown in Fig 2.18. By comparing with the conventional fiber, PCFs are able to sustain higher power and in the same time gaining a very low loss. In addition, the birefringent and dispersion properties have been enhanced too [22].

Conventional Optical Fiber



Photonic Crystal Fiber

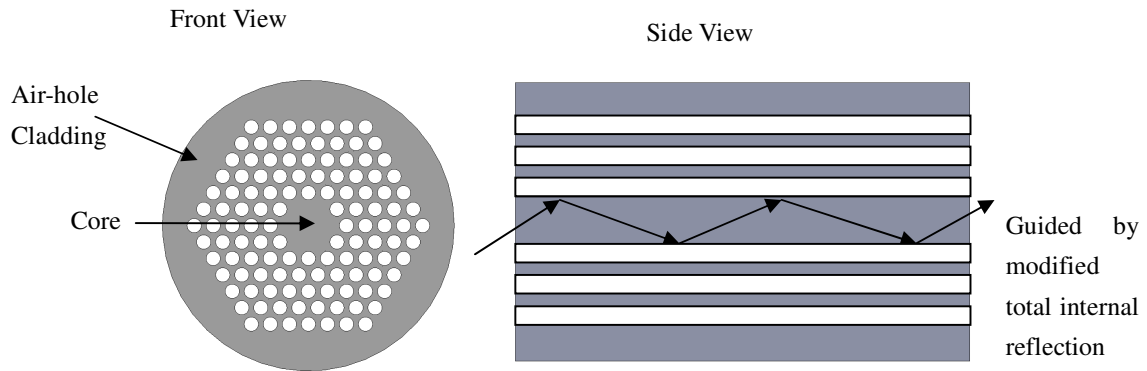


Fig 2.18 Structure of conventional fiber and PCF

PCF has been universally used in the telecommunication field, spectroscopy, microscopy, and micromachining. There are two types of PCFs, solid core PCFs (SCPCF) and hollow core PCFs (HCPCF), as shown in Fig 2.19. A SCPCF is with a higher refractive index solid core than the periodic air hole cladding. Whereas HCPCF is with an air core in the

centre of the fiber, such that the refractive index of the core is smaller than the periodic air hole cladding. In SCPCF, light is guided by modified total internal reflection (mTIR) mechanism and in hollow core PCF, light is guided by photonic bandgap (PBG) effect[23]. The general cross section structure of these two type of PCFs is shown in Fig 2.19a) and 2.19b).

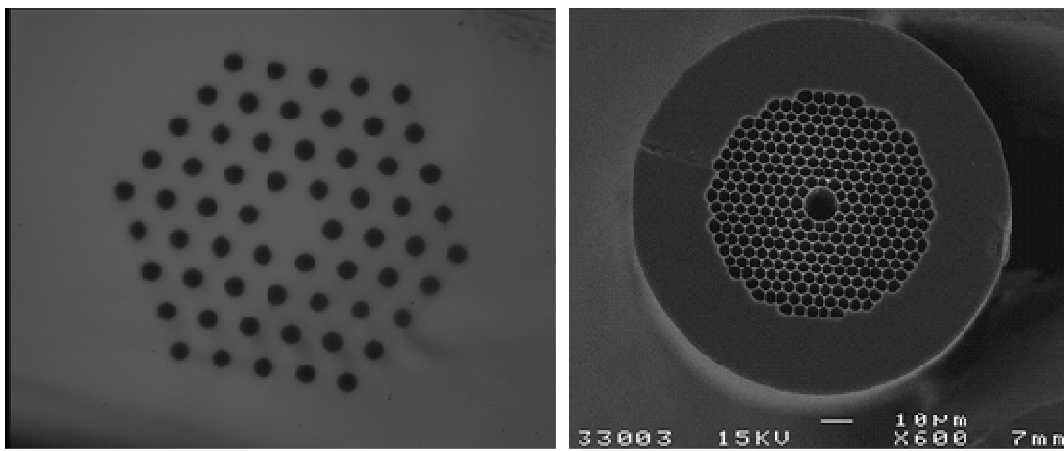


Fig 2.19 a) Solid Core PCF; b) Hollow Core PCF (Crystal Fibre A/S).

2.3.1 Modified Total Internal Reflection (mTIR)

Modified total internal reflection (mTIR) is analogous to total internal reflection (TIR) in standard optical fibers. In these conventional optical fibers, light is transmitted by TIR as its pure silica core provides a higher refractive index than its silica cladding. This positive core-cladding index contrast allows light to be confined in the core by TIR effect. Similarly, such high-index guiding mechanism is possible in solid-core PCFs. This is because the high refractive index silica core is surrounded by a photonic crystal cladding with a triangular lattice of air holes. The effective index of the microstructured cladding in solid-core PCFs is lower than the refractive index of the core. Hence, its positive

core-cladding index contrast allows light to be transmitted through a form of total internal reflection – mTIR. But the effective index contrast between the core and cladding is much higher than the conventional optical fiber. Thus the light confinement is much stronger.

mTIR happens only if the light is propagating from high index medium to low index medium and thereby it is compulsory for the average refractive index in cladding to be lower than in the core region. The average refractive index in cladding is defined as the effective refractive index calculated in the highest index mode, which is also known as fundamental space filling mode (FSM). This parameter is wavelength dependence [22, 24]. For this reason, the design parameters, for instance, the diameter or arrangement of air holes and the lattice constant can be modified to obtain the desired dispersion properties [25, 26].

The difference between conventional optical fibers and index-guiding photonic crystal fibers is that the cladding refractive index in conventional fiber is invariant across a wavelength range if eliminating the material dispersion. However, the cladding effective index of the index-guiding photonic crystal fiber strongly depends on the wavelength as shown in Fig 2.20. n_{fsm} is the effective index of the fundamental space-filling mode effective index.

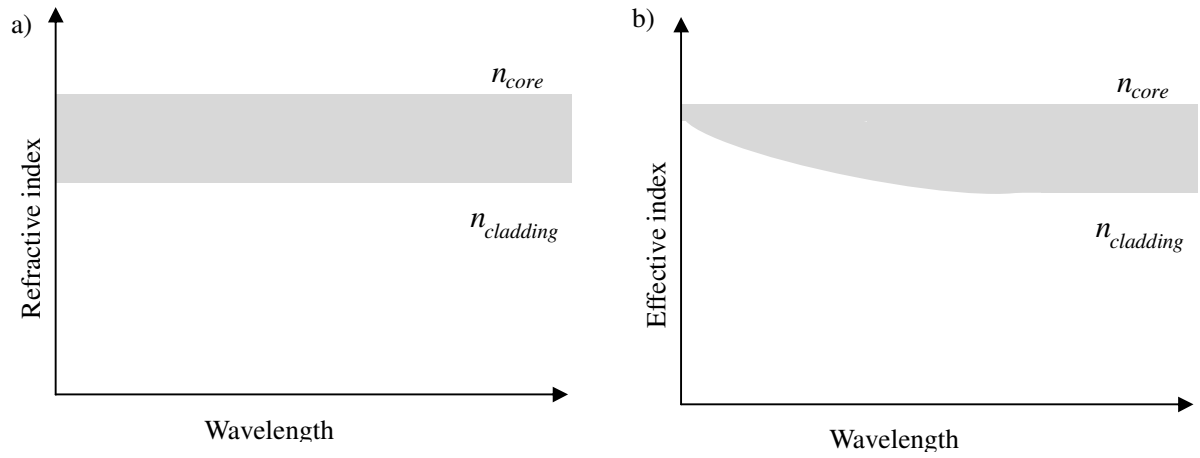


Fig 2.20 Refractive index profile for a) conventional optical fibers and b) index-guiding photonic crystal fibers.

2.3.2 Photonic Bandgap Effect (PBG)

PBG effect depends on the backscattering of coherent light into the core through the periodically arranged air hole cladding [20, 26]. Fig 2.21 displays the light guiding mechanism by PBG effect. The input light with certain wavelength is bounded inside the core region owing to the PBG in the cladding [20, 27].

Hollow Core Photonic Crystal Fiber

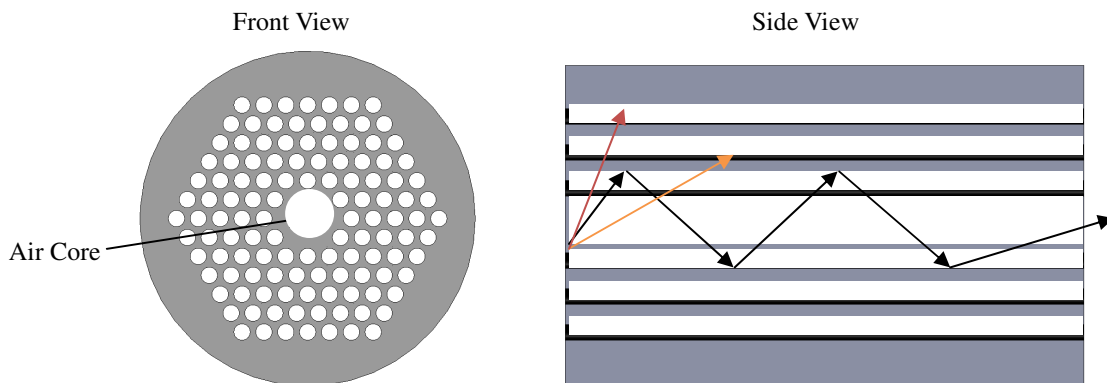


Fig 2.21 Light guiding mechanism by photonic bandgap effect (hollow core PCF)

For the purpose of deeper comprehending of the photonic band gap (PBG) phenomenon, it is necessary to understand the interaction of the molecules through macroscopic and microscopic scattering. From the macroscopic aspect, Bragg scattering occurs in a periodic dielectric material. The conditions of macroscopic resonance is governed by the condition [28]

$$m\lambda_{macro} = 2n_{lattice}D \quad m=1,2,3, \dots \quad (2.35)$$

where D is the period of dielectric structure.

For the microscopic resonance within a single unit cell, it must satisfied the equation [28]

$$m\lambda_{micro} = 2n_{airHole}r \quad m=1,2,3, \dots \quad (2.36)$$

This equation is well-illustrated in Fig 2.22. According to the diagram, if we want to get the maximum reflection of the light, the diameter of a dielectric well should be equal to one quarter of the wavelength.

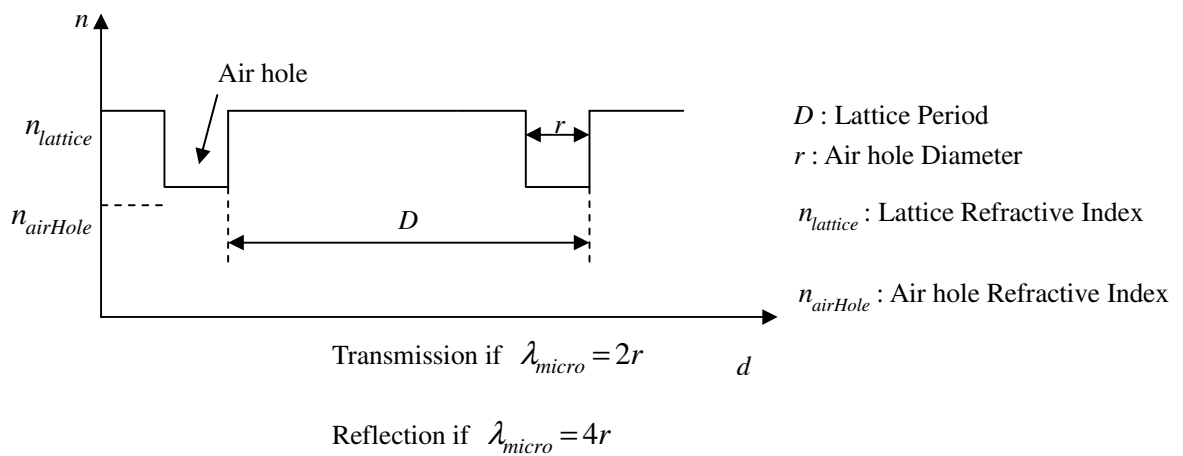


Fig 2.22 Microscopic resonance of a photonic crystal fiber

The PBG effect happens whenever the wavelength of both macroscopic and microscopic resonances coincides ($\lambda_{macro} = \lambda_{micro}$). Hence, the first order resonance of PBG is formed while [28]

$$\frac{r}{D} = \frac{1}{2} \frac{n_{lattice}}{n_{airHole}} \quad (2.37)$$

Apart from the conditions of resonance, another parameter that is important in describing the PBG effect is the propagation constant, β . There is a maximum value of β which prevents the propagation of light [28]:

$$\beta_{max} = nk_o \quad (2.38)$$

where k_o is the free space propagation constant.

Photonic Bandgap (PBG) phenomenon is the low index guiding mechanism used to transmit light in a hollow-core PCF. With its air core being surrounded by a microstructured cladding, the core-cladding index contrast would be negative, thus preventing standard TIR effect from occurring.

This unique light guidance mechanism is due to the microstructured photonic crystal cladding. The propagation of electromagnetic waves in certain frequency bands may be forbidden within the crystal if the choice of the structure, periodic lattice and the materials are appropriate [2]. The ability of photonic crystals that the propagation of photons with certain wavelengths could be inhibited is very similar to the band structure of semiconductors.

Thus, due to its periodic cladding structure, light confined in core of the hollow-core PCF undergoes a two-dimensional destructive interference process [3], where the air-hole walls act as reflectors as show in Fig 2.23. Hence, there is no propagation of light in certain wavelength regions. In other words, only certain wavelengths of light are confined in the core. These wavelengths are observed as pass bands in the transmission spectra.

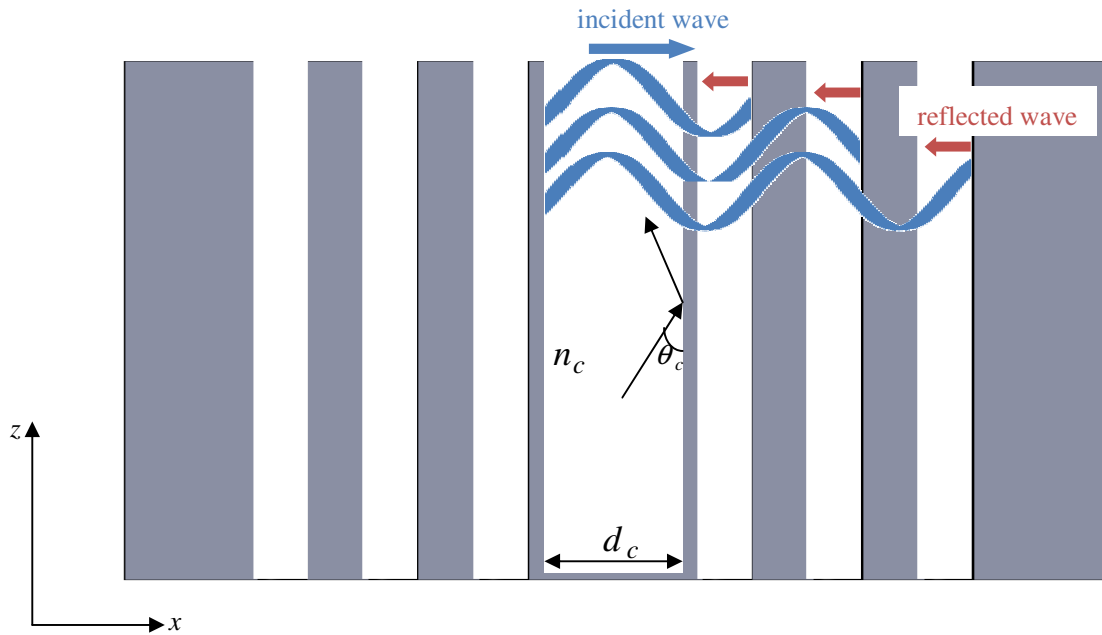


Fig 2.23 A wave incident on a bandgap material par

Consequently, the transmission spectrum obtained is seen to have several transmission windows which are defined as bandgaps[2]. In essence, when white light is shone into the fiber core, coloured modes are transmitted, indicating that only restricted wavelengths of light were guided; and this coincides with the photonic bandgaps [2].

If the air-hole arrangement is quarter-wave, the effective propagation angle θ_c of the bandgap-guided core mode is [28]

$$\sin \theta_c = \frac{\lambda}{2n_c d_c} \quad (2.39)$$

If the core diameter is much larger than the wavelength,

$$\theta_c \approx \frac{\lambda}{2n_c d_c} \quad (2.40)$$

And the effective refractive index can be calculated as

$$n_{eff} = n_c \cos \theta_c \quad (2.41)$$

This phenomenon can also be observed when a solid-core PCF is infiltrated with higher refractive index material. This is because if the material has a higher refractive index than the silica core ($n_{core}=1.45$), the effective index of the cladding will be higher than the core, resulting in PBG guiding mechanism for light transmission in the fiber.

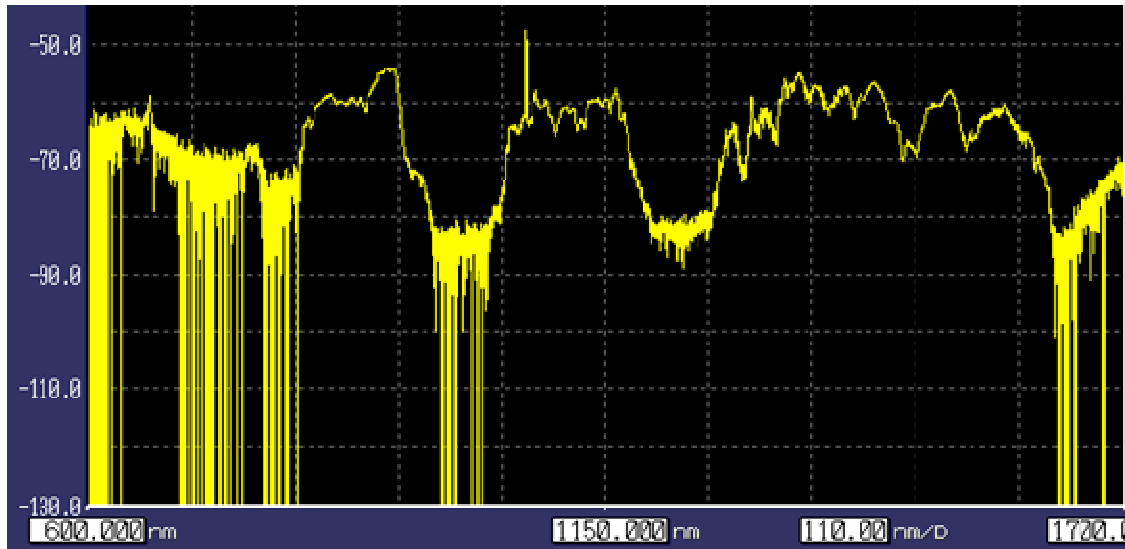


Fig 2.24 Transmission Spectrum for Photonic Bandgap Fiber.

2.4 Materials used in PCF Airholes Infiltration

2.4.1 Liquid Crystal

Liquid crystals seem to be an interesting class of material to infiltrate PCFs owing to their transparency in the near infrared spectrum and high birefringence with refractive index ranging between 1.4 and 1.6 [29].

Liquid crystalline state was first observed in 1888 by Friedrich Reinitzer, an Austrian botanical physiologist at the German University of Prague. During his research in examining the properties of several esters of cholesterol, he found a unique phenomenon in these esters. The ester was found possessing double melting point, i.e. at certain temperature it melted to a cloudy liquid which changed again to an optically clear liquid at a higher temperature. These phase changes are reversible. For the explanation, he collaborated with Otto Lehmann, a German physicist, and discovered the optical anisotropy of these esters[30]. These esters are then classified as liquid crystals. Their unique characteristic makes them become an important material in a lot of electrical applications that is indispensable to our life such as liquid crystal displays (LCD) and crude thermometer.

Liquid crystals exhibit the features from both crystalline solid and amorphous liquid. There are generally categorized into thermotropic, lyotropic and metallotropic phases[31]. Thermotropic liquid crystals undergo phase transitions when the temperature

is varied, whilst lyotropic liquid crystals perform phase transitions when the concentration of solute molecules is altered [32]. The former is mainly found in electro-optic display technologies, whilst the latter is evident in DNA and cell plasma membranes. Metallotropic liquid crystals are composed of both organic and non-organic molecules. They exhibit phase transitions when the temperature, solute concentration and inorganic-organic ratio are altered.

The liquid crystal molecules are arranged in a distinct texture under a polarized light source. Based on the ordering of the molecules, liquid crystals are categorized into three phases: nematic, smectic and cholesteric phases. Nematic phase is the most commonly used liquid crystals phase. The molecules have long-range orientational order but no positional order. Smectic phase forms layer structure that can slide pass each other. The molecules are oriented normal to the plane of layers. Similar to nematic phase, the molecules have long-range orientational order, but show more positional order than nematic phase. Cholesteric phase, also known as chiral nematic phase, is composed of optically active molecules and thus there is a spontaneous twisting of the molecules around the axis perpendicular to the director [33, 34].

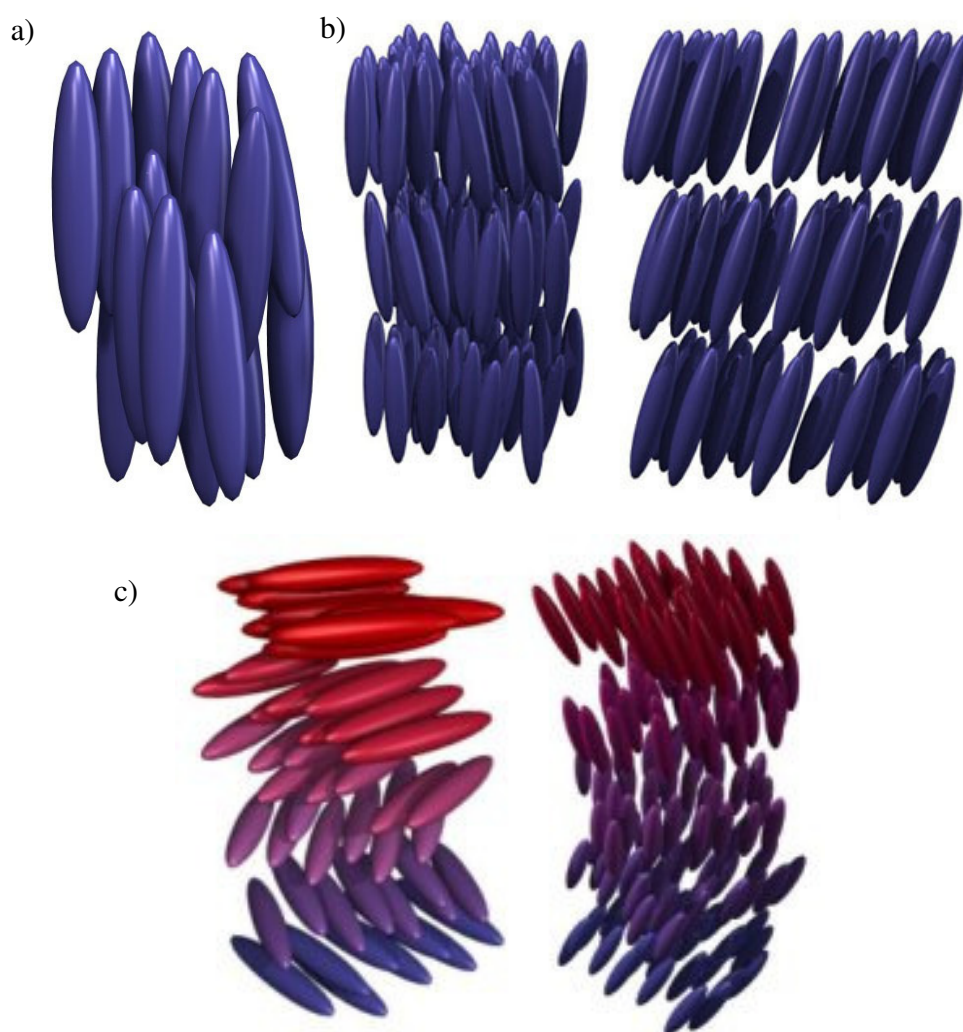


Fig 2.25 Three types of liquid crystals: a) Nematic, b) Smectic, c) Cholesteric [35-37]

The most remarkable property of liquid crystals is the highly optical nonlinearity of the molecules due to their sensitivity to the electric, magnetic and thermal effect.

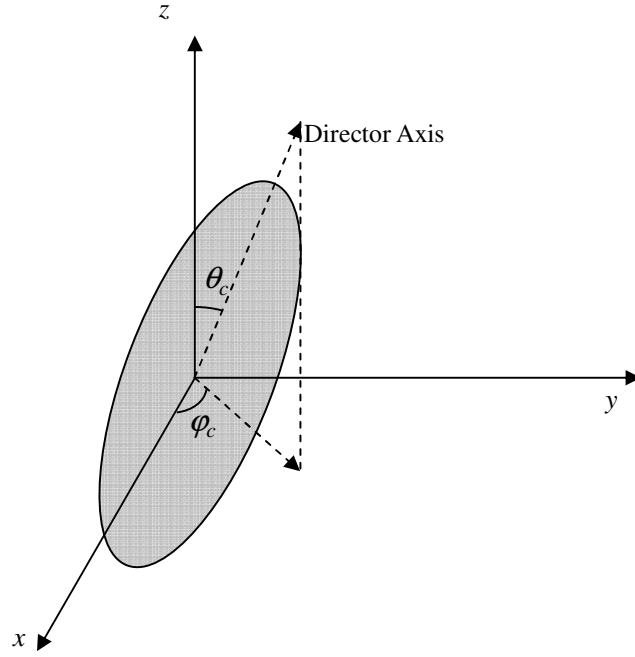


Fig 2.26 The liquid crystals director defined in the Cartesian coordinates

For example, the existence of the external electric field changes the orientation of the optic axis (director) of liquid crystals. As shown in Fig 2.26, the director is off-axis in z-direction (deviate from z-axis). The perturbed permittivity tensor in the cylindrical coordinates is given by the following equations[38]

$$\epsilon'_{11} = \frac{1}{2}(\delta_{11} + \delta_{22}) + \frac{1}{2}(\delta_{11} - \delta_{22})\cos 2\phi + \delta_{12}\sin 2\phi \quad (2.42)$$

$$\epsilon'_{12} = \delta_{12}\cos 2\phi - \frac{1}{2}(\delta_{11} - \delta_{22})\sin 2\phi \quad (2.43)$$

$$\epsilon'_{13} = \delta_{13}\cos \phi + \delta_{23}\sin \phi \quad (2.44)$$

$$\epsilon'_{21} = \epsilon'_{12} \quad (2.45)$$

$$\epsilon'_{22} = \frac{1}{2}(\delta_{11} + \delta_{22}) - \frac{1}{2}(\delta_{11} - \delta_{22})\cos 2\phi - \delta_{12}\sin 2\phi \quad (2.46)$$

$$\epsilon'_{23} = -\delta_{13}\sin \phi + \delta_{23}\cos \phi \quad (2.47)$$

$$\epsilon'_{31} = \epsilon'_{13} \quad (2.48)$$

$$\epsilon'_{32} = \epsilon'_{23} \quad (2.49)$$

$$\epsilon'_{33} = \epsilon_{33} \quad (2.50)$$

$$\delta_{11} = \epsilon_o[(n_o^2 \cos^2 \theta_c + n_e^2 \sin^2 \theta_c) \cos^2 \varphi_c + n_o^2 \sin^2 \varphi_c] \quad (2.51)$$

$$\delta_{12} = \epsilon_o[n_o^2(\cos^2 \theta_c - 1) + n_e^2 \sin^2 \theta_c] \cos \varphi_c \sin \varphi_c \quad (2.52)$$

$$\delta_{13} = \epsilon_o(n_e^2 - n_o^2) \cos \theta_c \sin \theta_c \cos \varphi_c \quad (2.53)$$

$$\delta_{22} = \epsilon_o[(n_o^2 \cos^2 \theta_c + n_e^2 \sin^2 \theta_c) \sin^2 \varphi_c + n_o^2 \cos^2 \varphi_c] \quad (2.54)$$

$$\delta_{23} = \epsilon_o(n_e^2 - n_o^2) \cos \theta_c \sin \theta_c \sin \varphi_c \quad (2.55)$$

$$\delta_{33} = \epsilon_o[n_o^2 \sin^2 \theta_c + n_e^2 \cos^2 \theta_c] \quad (2.56)$$

where ϵ' are the tensor indices, n_o is the ordinary refractive index, n_e is the extraordinary refractive index, ϕ is the azimuthal angle of the cylindrical coordinates defined in the LC-core fiber. It shows an extremely large alternation of refractive index of liquid crystals under applied electric field. As a consequence, it brings many possibilities for tuning the light propagation properties.

The investigation of the nonlinear properties of liquid crystals has also been carried out by several research groups. By doping the liquid crystals using the dyes, nanoparticles etc., their nonlinear characteristic can be enhanced[39]. The strongly anisotropic of the compounds lead to a wide range of birefringence characters that allow the liquid crystal turning into a promising material to generate various optical applications.

2.4.2 Dyes

2.4.2.1 Fluorescent Dyes

Fluorescent dyes, also called fluorophore, are chemical compounds usually contained several aromatic groups. They are able to re-emit light upon relaxation to its ground state S_0 after being excited to higher quantum state S_1 as shown in Fig 2.27. The absorption and emission wavelengths depend on their chemical structure.

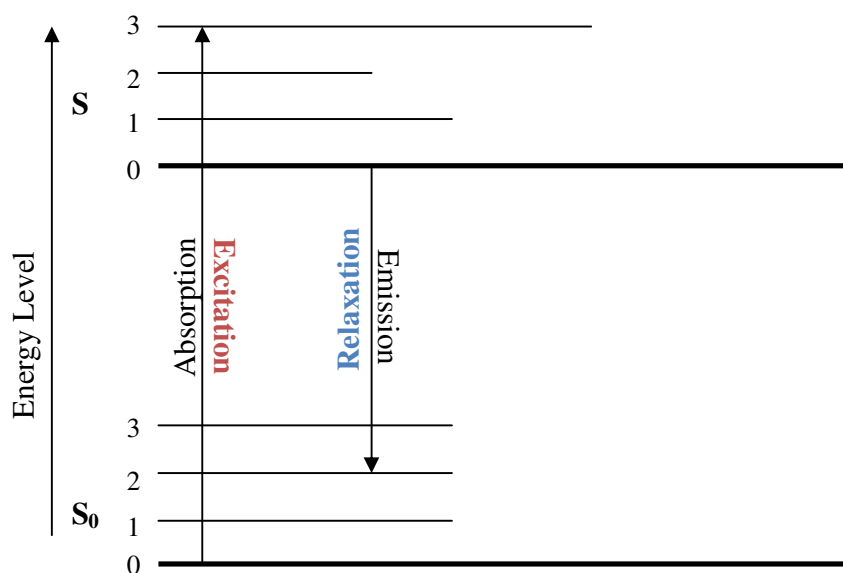


Fig 2.27 Relaxation of a fluorescent dye upon excitation

They have long been used to visualize cell biology at many levels, from molecules to complete organisms. The commonly used fluorophores are small organic dyes, fluorescent proteins and quantum dots. Small organic dyes are mainly used for labeling macromolecules. Due to the lack of specificity, most applications use antibodies in fixed and permeabilized cells. The main applications for fluorescent proteins are in antibody

conjugates for surface labeling in flow cytometry and enzyme-linked immunosorbent assay. Quantum dots are inorganic nanocrystals. They are relatively stable in a way that they can be repeated imaging of single molecules.

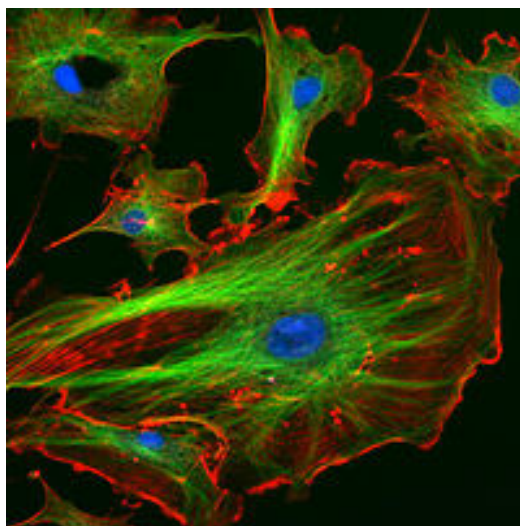


Fig 2.28 Fluorescent dye application in life science[40]

Fluorescent dyes have been applied in photonic crystal fiber for evanescent wave sensing enhancement. The important parameter for consideration is that the fluorescence photon emission decay time has to be taken into account when choosing fluorescent compounds for practical applications.

2.4.2.2 Azo Dyes

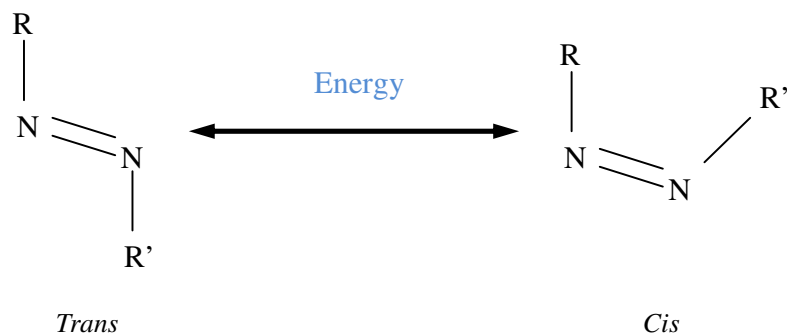


Fig 2.29 Trans-cis isomerization of Azo Dye Compounds

Azo dyes are molecules with chemical functional group $R-N=N-R'$, which R and R' can be either aryl or alkyl. They are able to absorb light at a specific wavelength in the visible region. Besides that, azo dyes own their unique properties of photo-induced birefringence and dichroism which is mainly based on the reversible trans-cis isomerization and subsequent anisotropy as shown in Fig 2.29. Under suitable circumstances, the reformation is able to generate wider spread of molecular movement and even modification of material characteristic. For the azobenzenes that are angularly distributed with the exposure of light, they will switch from *trans*-form to *cis*-form whereas those benzenes that fall at right angle to the light polarization are not able to realign and undergo *trans-cis* isomerization. Thus, it results in net reduction of azobenzenes oriented along the light polarization and accompany with an accumulation of azo dyes that redistribute perpendicularly [41]. The detailed illustration is shown in Fig 2.30.

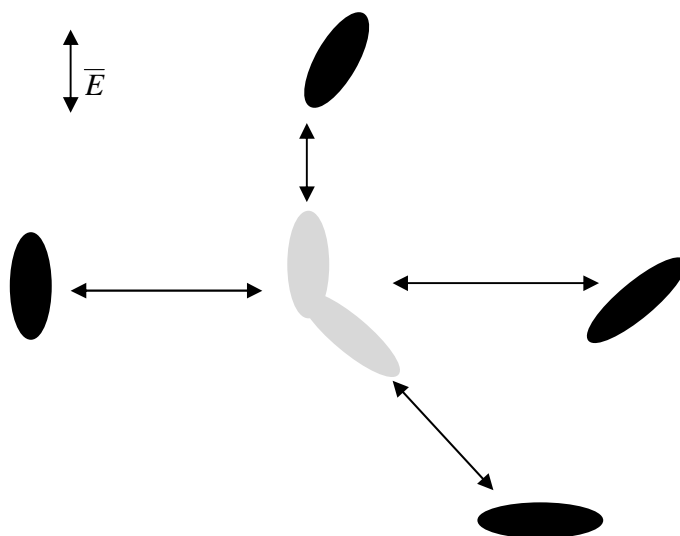


Fig 2.30 Molecules aligned along light polarization direction

2.4.3 Other Materials Used

2.4.3.1 Carbon Nanotube

A carbon nanotube(CNT) is an emerging material that made of carbon and in tube-shapes with tube diameter in nano-scale. CNTs are popular in recent years, owing to their superb electrical and thermal conductivity and strong mechanical strength that could be used in various applications. Naturally CNTs align themselves in a specific direction, which is similar to liquid crystal.

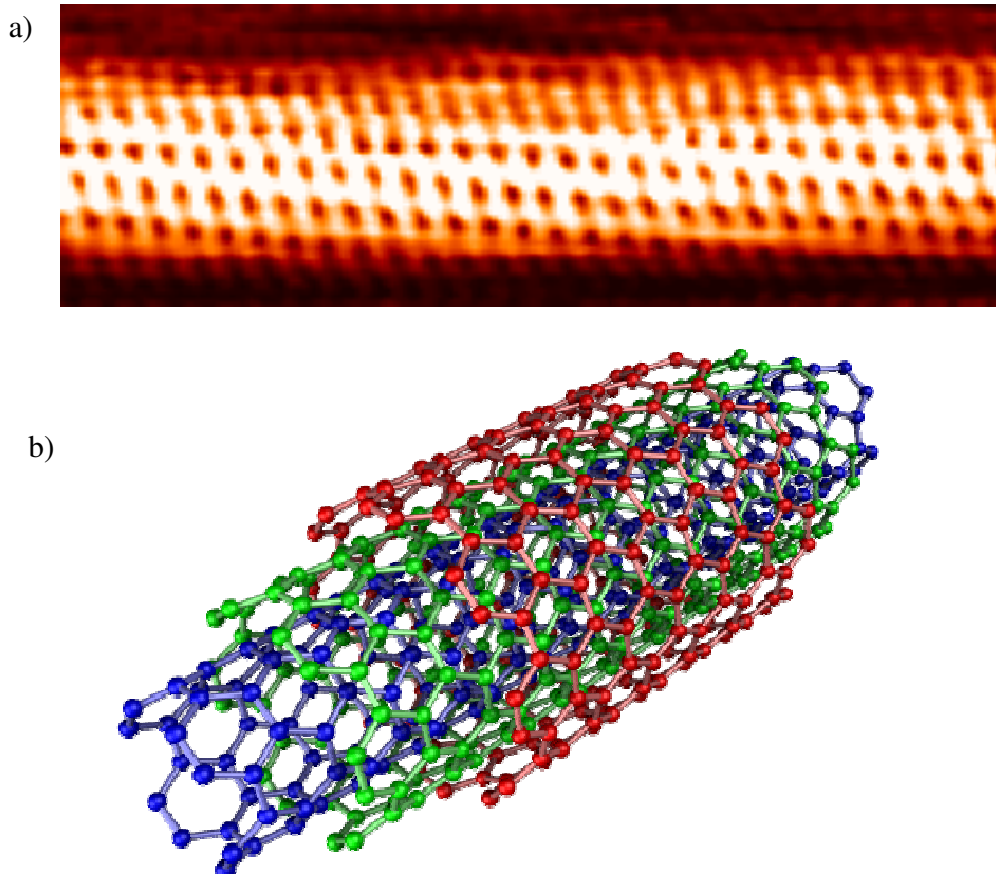
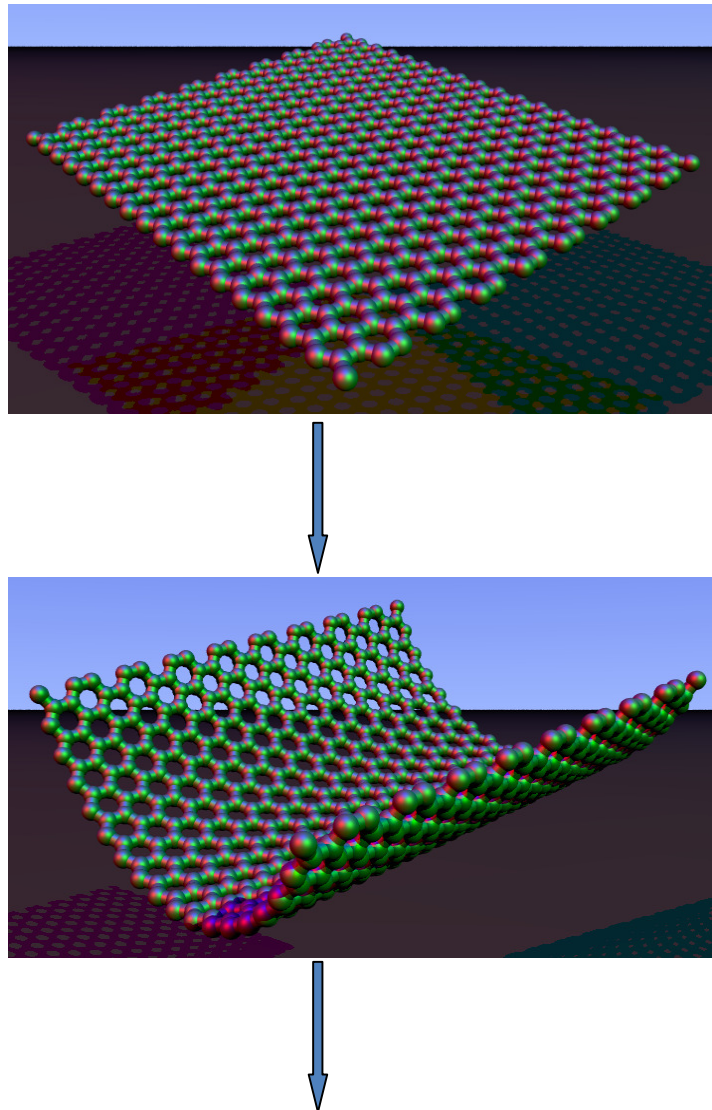


Fig 2.31 Schematic of the carbon nanotube basic unit. a) High resolution scanning tunneling microscopy image of a

helical semiconducting SWNT. b) Multi-walled CNTs [42, 43]

There are two types of carbon nanotubes in generally, single-walled CNT or multi-walled CNT shown in Fig 2.31. The diameter of Single-walled CNT is generally close to 1 nm. However the length could be million times longer than the diameter. Its structure can be conceptualized by rolling one layer of graphene (with thickness about one atom thick) into a seamless cylinder as shown in Fig 2.32. Multi-walled CNTs consist of multi-layer of the rolled graphene.



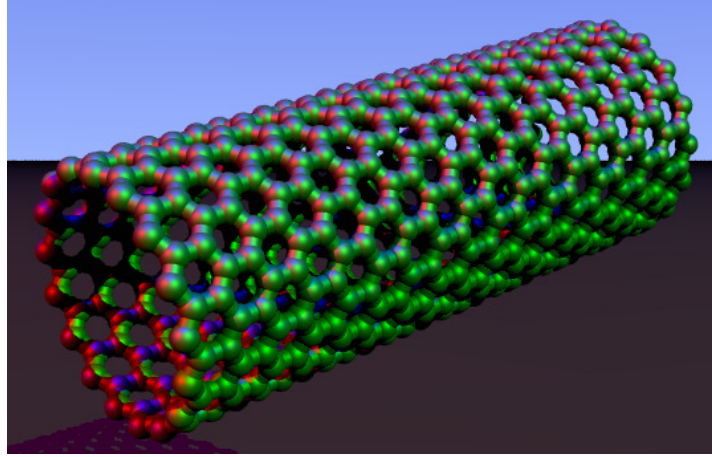


Fig 2.32 Single-walled CNT formed by rolling a layer of graphene into a seamless tube[44, 45]

CNTs have been heavily applied as optical materials for bio-sensing. By using CNTs, strong and simple resonance Raman spectroscopy could be achieved [46]. By infiltrating CNTs into PCF, the guiding properties of PCF could be modified. High performance sensors could be achieved based on the PBG modifications [47].

2.4.3.2 Nanoparticles

Nanoparticles are particles in nanometer scale and competent to act as a whole unit. Owing to the large surface area of the nanoparticles, the properties of the nanoparticles change accordingly. The physical properties depend more on its sizes other than constant. For example, the melting temperature of gold nanoparticles drops dramatically compared to gold slabs.

Nanoparticles are mostly used in biological applications such as nano-sized carriers or

bio-markers [48, 49]. Plasmonic devices could also be developed by coating nanoparticles on the walls of the PCF air-holes to promote the particle-adequate spectral characteristics [50].

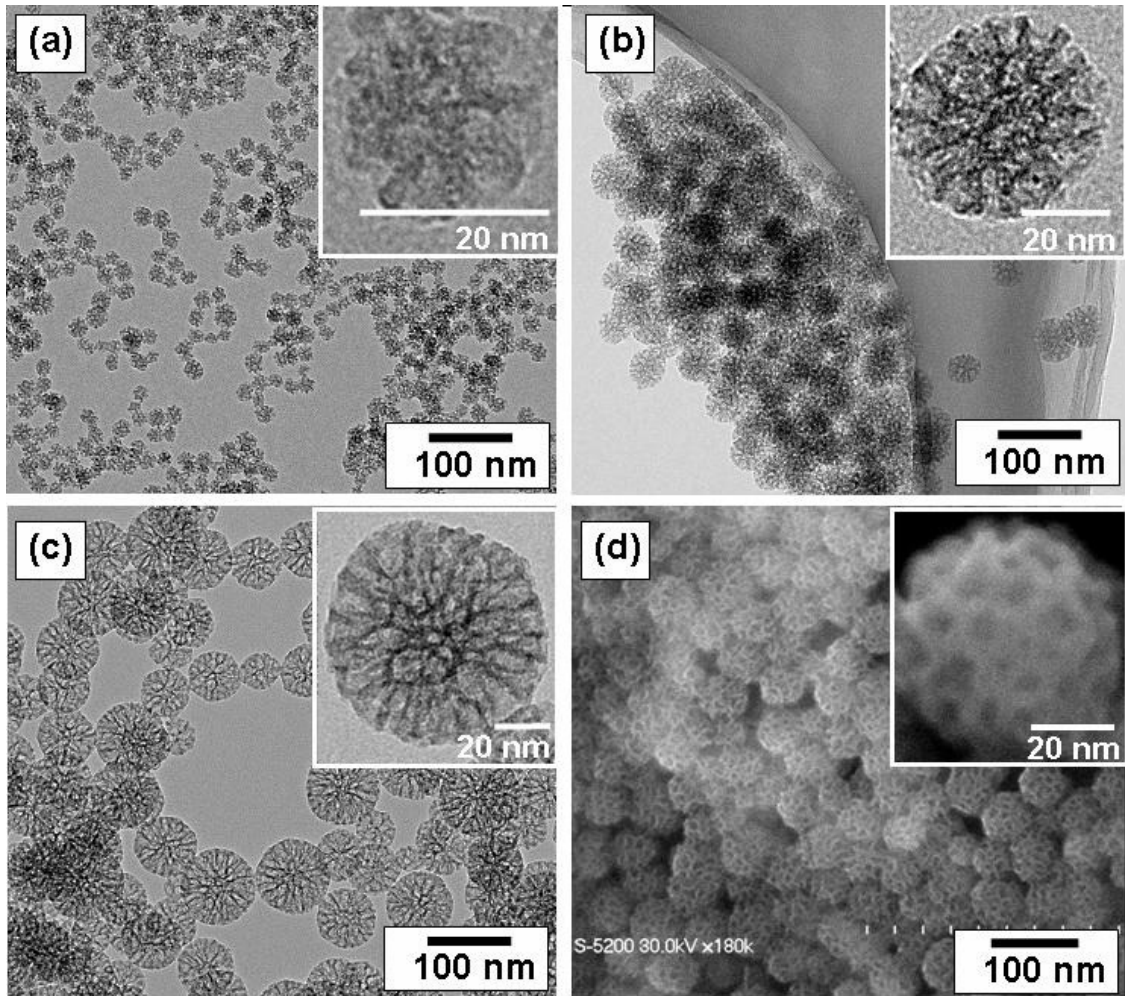


Fig 2.33 TEM images of the mesoporous silica nanoparticles with: (a) 20nm, (b) 45nm, (c) 80nm. (d) SEM image of (b) [51].

2.5 Chapter Summary

In this chapter, the basic knowledge of optical fiber, photonic crystal fiber and the various materials for integrating into PCF have been introduced. Optical fiber sensors, which

combine with other optical techniques, have been studied for decades. The major disadvantage of normal single mode optical fiber sensing is that the cladding of the fiber must be removed to increase the sensitivity at the cost of making the fiber more fragile and increasing the difficulty to couple the light back to the fiber. The emergence of the PCFs overcomes the disadvantages of the normal SMF and preserves the unique advantages of the optical fiber. Furthermore, the airholes surrounding the PCF cladding provide opportunities for other materials infiltration (such as liquid crystal, dyes, carbon nanotubes or nanoparticles) so that the sensitivity could be increased or the optical properties of the specific fiber could be tuned to meet the specific needs.

In the following chapters of this thesis, the performances of PCF sensing by mTIR and PBG are both evaluated. The tunabilities of PCF by infiltrating different materials have also been investigated as well.

Chapter 3

Photonic Crystal Fiber for Sensing

3.1 Introduction

It has been decades that optical fibers have been employed in sensing applications. Optical fiber sensors are made by modifying the fiber in a way that the desired parameters such as strain, temperature, pressure can alter the transmission power, phase, polarization or wavelength in the fiber. And the changes can be measured by optical equipments[52]. They offer the advantages of being robust and small in size, biocompatible and low cost. Besides, compared to electrical type sensors, they have higher sensitivity, higher resolution, intrinsic electrical passivity and electromagnetic interference immunity [53-55]. To achieve larger surface contact area and higher sensitivity, different methods have been approached. Chemical etching of fiber cladding, tapering of fiber probes, inscribing periodical refractive index modulation in the fiber core etc have been widely investigated[4,5,8]. Those approaches have indeed improved the performance of the optical fiber sensors. But there are some drawbacks. Most of the approaches require additional modifications to be done. It is much more time consuming. Furthermore, for chemical etching, a strong and hazardous etchant such as hydrofluoric acid (HF), is needed, which may be dangerous.

Photonic crystal fiber has recently found its applications in diverse areas of science and technology[56] such as fiber-optic communications, fiber lasers and amplifiers, nonlinear devices, high-power transmission, gas sensors, optical sensors etc[24,25]. Integrating PCF into an optical fiber sensing system provides numerous advantages. The surface contact area is maximized in the PCF airholes. Moreover the airholes in the PCF provide opportunities for sample infiltration, which shorten the distance between the sample and the fiber core. Thus the sensitivity could be enhanced. Another advantage of using PCF is that light can be confined in the fiber either by total internal reflection or photonic bandgap effect. If the surrounding refractive index is higher than the fiber core, light can be guided via photonic bandgap effect.

In the following, single mode fiber LPG refractive index sensing will be evaluated and follow by exploring different approaches of PCF sensing for showing the capabilities of sensing. The uses of the PCF as pressure, temperature and refractive index sensors have also been investigated. Light guiding mechanism for each sensing is not the same for different approaches.

3.2 Single Mode Fiber LPG Glucose Sensing¹

Among different optical fiber sensors, fiber grating sensors are one of the most popular

¹ NOTICE: This is the author's version of a work accepted for publication by ACM. The definitive version has been published in Proceedings of the 2008 International Conference on Advanced Infocomm Technology, 80, 2008, DOI: 10.1145/1509315.1509395.

techniques owing to their flexibility and high sensitivity. Studies have shown that LPG sensors can be more sensitive than FBG sensor owing to the different mode coupling between the guided mode and the cladding mode [57]. The phase matching condition that governs the LPG operation is given by [58]:

$$\lambda_m = (n_{co}^{eff} - n_{cl,m}^{eff})\Lambda \quad (3.1)$$

where λ_m is the wavelength of the m -th order of transmission dip, n_{co}^{eff} is the effective index of the fundamental core mode, $n_{cl,m}^{eff}$ is the effective index of the m -th cladding mode and Λ is the period of the grating. The effective index of the cladding modes are a strong functions of the medium refractive index surrounding the cladding. The changes of the effective index are mainly due to the material and waveguide dispersion. It is assumed that the material dispersions in the core and cladding are the same. Thus the key contributor on the effective index difference between core and cladding lies on the waveguide dispersion. Any change of the ambient refractive index modifies the effective index $n_{cl,m}^{eff}$ of the cladding modes. According to Eq(3.1), the transmission dip wavelength of the m -th order mode is dependent on the effective index of a particular cladding mode. Any change in the ambient refractive index will thus alter the value of λ_m . In addition, since the fiber cladding does not undergo the etching process, the fundamental guided mode is well confined in the fiber core and therefore is not influenced by the changes in the ambient refractive index. In this situation, the change of the transmission dip wavelength is given simply by [9]

$$\frac{d\lambda_m}{dn_{ambient}} = \frac{d\lambda_m}{dn_{cl,m}^{neff}} \cdot \frac{dn_{cl,m}^{neff}}{dn_{ambient}} \quad (3.2)$$

where $n_{ambient}$ is the ambient refractive index. Each transmission dip wavelength is expected to undergo a different shift, since the value of $dn_{cl,m}^{neff}/dn_{ambient}$ is dependent on the order of the cladding mode. Moreover, the magnitude of the wavelength shift increases as the ambient refractive index approaches the cladding refractive index [9] .

3.2.1 Experimental Investigation

The LPG was fabricated by the amplitude mask technique with periodicity of 350 μm . It used standard SMF-28 optical fiber, photosensitized through hydrogen loading. It was UV irradiated using KrF excimer laser and the growth of spectrums was monitored throughout the whole fabrication process using an optical spectrum analyzer (OSA, Ando AQ6317) and a tunable laser source (TLS, Ando AQ4321D). For the H_2 -loaded LPG, it had to go through annealing at a temperature of 85°C for at least 5 hours in order to stabilize the LPG spectrum.

Before coating the enzyme-encapsulated sol-gel on the surface of the LPG, its sensitivity to the refractive index was tested by using refractive index oil with refractive index ranging from 1.33 to 1.43. The LPG was cleaned with ethanol and distilled water after each measurement in order to eliminate the influence of the last measurement. The transmission spectra for different refractive index oil were shown in Fig. 3.1. The wavelength of the transmission dip shifts to shorter region when the refractive index of surrounding medium increases. It has a wavelength shift of 32 nm with the change of

refractive index of 0.43.

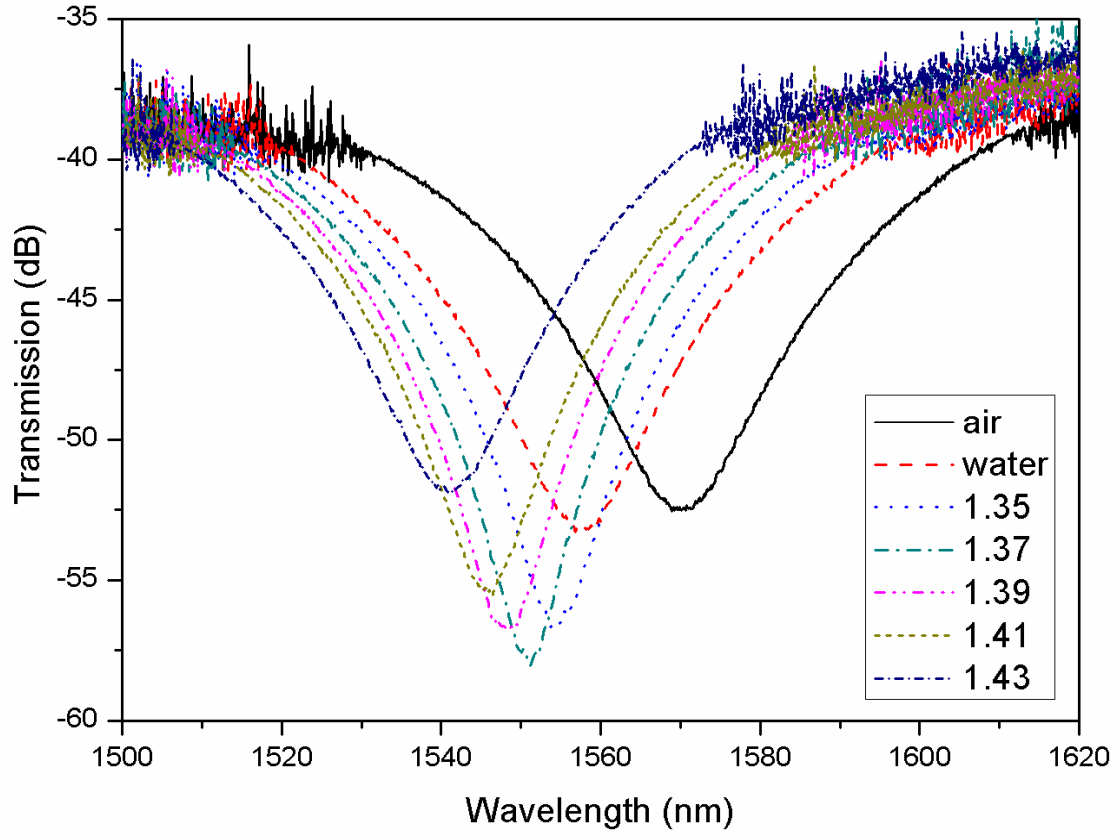
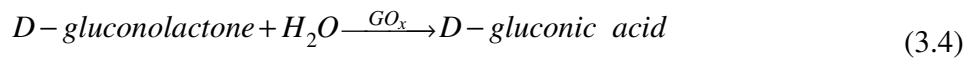
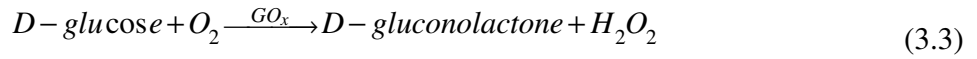


Fig 3.1 Transmission spectra for different refractive index liquids.

After testing, the LPG was prepared for the sol-gel coating. The sol gel solvent was prepared with 12:3:1 of tetraethyl-orthosilicate (TEOS): DI water: ethanol. 25 μL of 1M HCL was added to catalyze the gelation rate. The solvents were stirred at a constant rate of 500 rpm for one hour. 1.92 mg of glucose oxidase (GOx, Type X-S from *Aspergillus Niger*, Sigma Aldrich) was dissolved to 150 μL 50 mM sodium acetate buffer. The suspension in the vial was inverted several times until all the lyophilized powder had dissolved. 150 μL of prepared sol gel solution was then mixed with GOx enzymatic assay.

In the assay, a single unit of GOx catalyzes the oxidation of D-glucose by molecular oxygen into hydrogen peroxide (H_2O_2) and D-gluconolactone. But D-gluconolactone hydrolyses in water to D-gluconic acid[59]. Thus the concentration of D-glucose is determined by the refractive index changes induced by D-glucose acid.



This mixture of sol-gel solution and enzymatic assay were deposited on the LPG fiber to form a homogenous layer surrounding the fiber. When the sol-gel coating was ready, the enzymes could be encapsulated within the pores of the matrix upon gelation, and were able to undergo interactions with the specific analytes simultaneously. Fig. 3.2 shows the sol-gel matrix coating around LPG fiber.

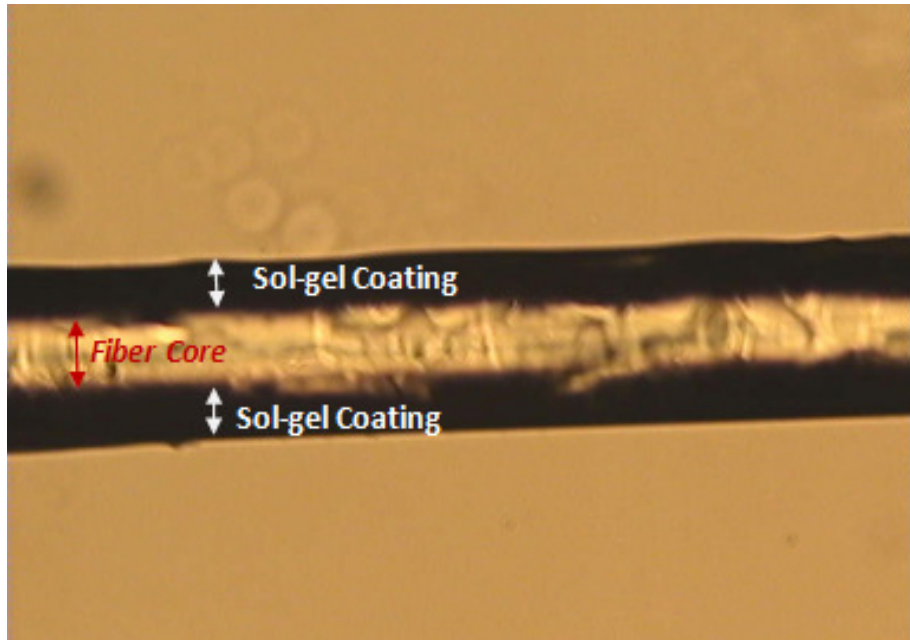


Fig 3.2 Microscope image of sol-gel coated LPG.

The schematic diagram of the experimental setup for detecting glucose concentration is

shown in Fig. 3.3. Sol-gel coated LPG fiber was hold in a fixed and straight position with certain weight added at both ends in order to eliminate the effect of external bending on the wavelength shift. One end of the LPG was connected to a broadband laser source (KOHERAS, Superk Compact) and the other end was connected to an optical spectrum analyzer. Five different concentration of glucose solutions were deposited on sol-gel matrix coated LPG fiber separately and corresponding spectrum was recorded for analyze. The glucose solution was prepared by adding various quantities of D-glucose into 100 mL distilled water separately, and stirred continuously for one hour to ensure all glucose solutions were in homogeneous state. A 1 mL glucose solution of various concentrations was deposited to sol-gel region of the LPG fiber. During the adding of glucose solution, a stabilization time of thirty seconds was allowed for the enzyme-substrate reaction to occur before acquiring transmission spectrums for analysis purposes.

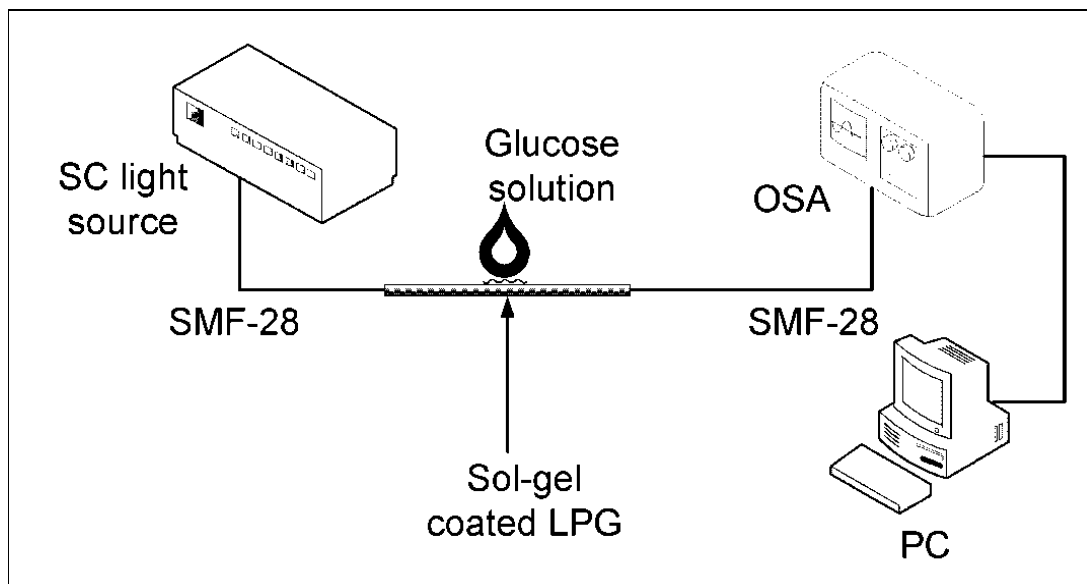


Fig 3.3 Schematic diagram of experimental setup.

The transmission spectra for different concentrations are shown in Fig 3.4. When no glucose solution is added, the wavelength value is 1567.9 nm. When the concentration of glucose solution increases, GOx oxidize glucose molecules to form D-gluconic acid. The formation of D-gluconolactone and gluconic acid changes the sol-gel matrix refractive index. Thus when glucose concentration increases, the refractive index of sol-gel matrix increases, shifting the transmission dip wavelength to blue region. The biosensor is operable as a refractometer as long as the refractive index of the coating that surrounds the grating is less than the effective index of the optical fiber and glucose oxidase are not fully consumed. Eq(3.3) shows that the resonance wavelength depends on the core and cladding effective index. When the difference between the core and cladding effective index decreases, the corresponding resonance wavelength of the grating will be of smaller value. That is the transmission dip shifts to shorter wavelength.

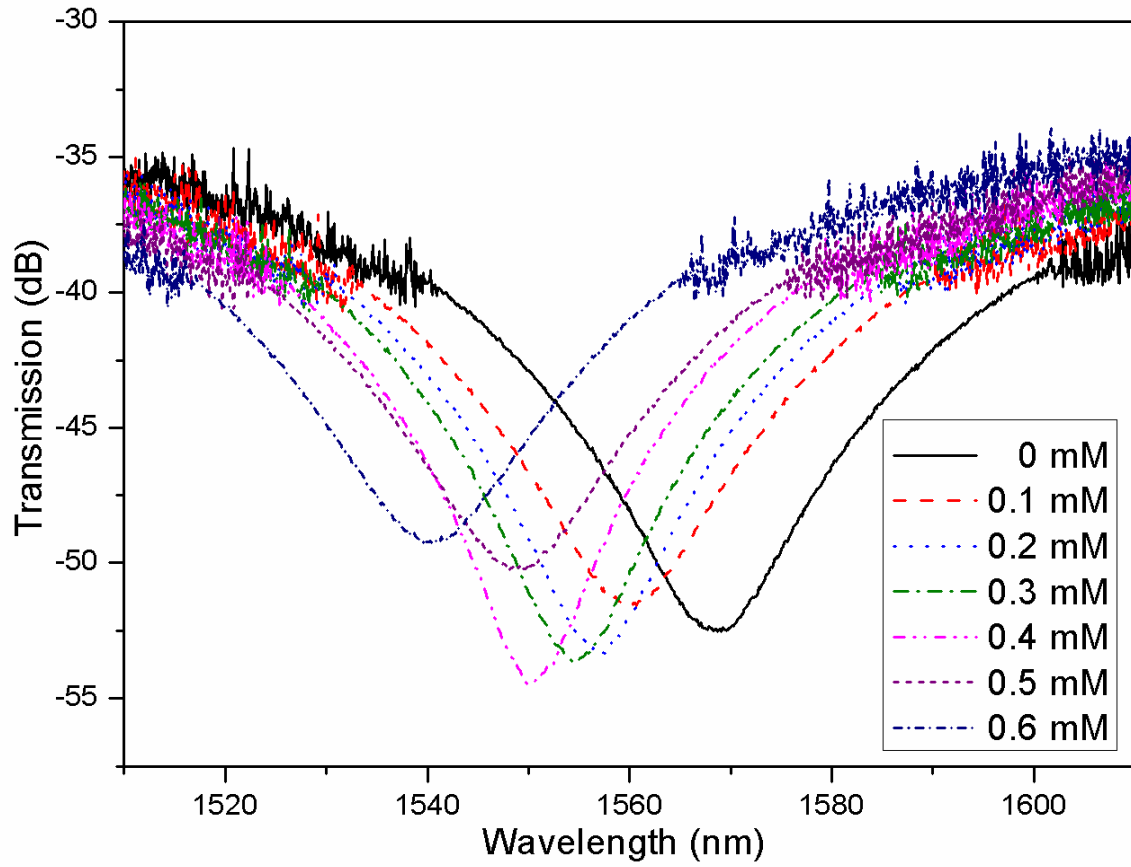


Fig 3.4 Transmission spectra for different glucose concentration

The sensitivity of this glucose biosensor is illustrated in Fig. 3.5. The sensitivity coefficient and R^2 value are calculated computationally. They are 39.8 mM/nm and 0.9752 respectively.

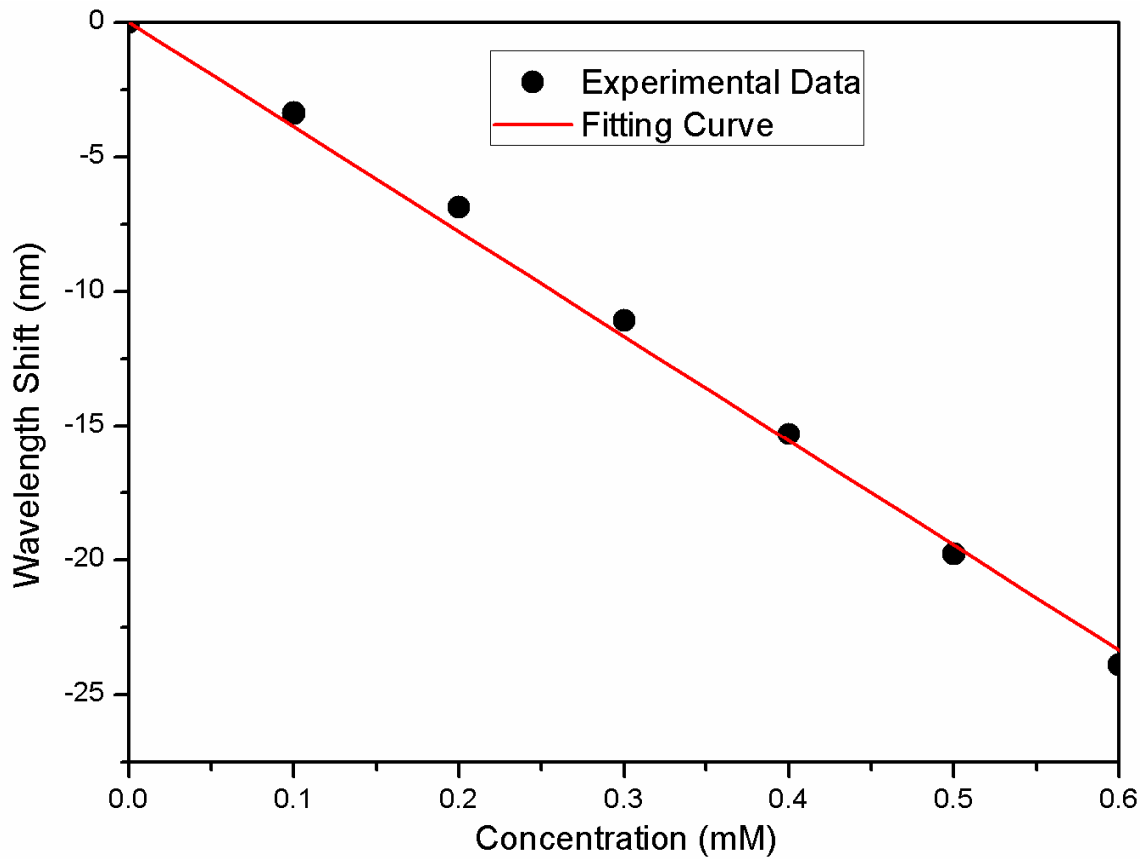


Fig 3.5 Sensitivity of the wavelength shifts for different concentrations.

Generally, LPG sensing can be designed to exhibit very high sensitivity for a particular wavelength[57]. Studies show that the sensitivity condition is different for each cladding mode. Therefore, the sensitivity of a LPG sensor for a particular wavelength could be optimized by carefully selecting a cladding mode at a fixed grating period.

3.3 PCF LPG for Pressure Sensing²

Not only in single mode fiber, LPG can also be inscribed in the special type of optical

² © 2012, IEEE. Reprinted, with permission, from Y.F. Zhang, C.C. Chan, Y.M. Chan and P. Zu, "Tilted Long Period Gratings Pressure Sensing in Solid Core Photonic Crystal Fibers", IEEE Sensors Journal, vol 12 (5), pp. 954-957, 2012

fiber, the photonic crystal fiber (PCF). Studies have shown that PCF LPG can be used as sensing. In year 1990, it was proposed that fiber axis mode coupling of the grating would be enhanced by introducing some tilted angle between the wave vector [60]. A tilt in the grating allows coupling of the core mode to co-propagating modes of different orders [61]. From then on, the tilted fiber grating has attracted numerous attentions. It has found its applications in sensing [62-64], filtering [65, 66] and wavelength division multiplexing [67, 68], etc in the past few decades.

In recent year, fiber grating has been extended to PCF, for improving the refractive index measurement [69]. In general, the tilted fiber gratings are fabricated by using phase mask method, scanning technique and point by point writing technique. However it is difficult to apply these techniques in photonic crystal fiber grating fabrication due to the existence of air-holes in the cladding. Another method to fabricate fiber grating is by using mechanical pressure, which is widely used in conventional single mode fibers[70]. By mechanically pressing a periodic structure on the fiber, the periodic refractive index modulation is formed in the core of the fiber. This technique can be easily extended into PCF long period grating (LPG) fabrication. One advantage using mechanical pressing is that the resonant wavelength dips can be adjusted by the manual change of the grating period, the pressure applied on the fiber [70] and the fluid infiltrated into the holes of the cladding layer [69].

3.3.1 Experimental Investigation

The solid core photonic crystal fiber used was from Crystal Fibre A/S. It consisted of a solid silica core with core diameter of 10 μm which was surrounded by four rings of circular air holes in a triangular lattice. To eliminate temperature variation, the whole experiment was carried out in a temperature controlled chamber. Light from a super-continuum light source was launched into one end of the PCF. The other end of the fiber was butt-coupling to a SMF-28. The SMF was connected to an optical spectrum analyzer (OSA, ANDO AQ6317B) where the transmitted light was measured. The PCF was placed in a special fiber holder (Fig 3.6(a)) which was custom-made with five fiber slots in the holder. Each slot formed different angle with the holder edge. There were five angles in total, 0°, 5°, 10°, 15° and 20°. A periodically V-grooved brass block was placed on top of the fiber holder in the middle of the PCF. The grating structure was obtained by applying a transverse force on the fiber at the block region. The force was manually controlled by a stress gauge fixture.

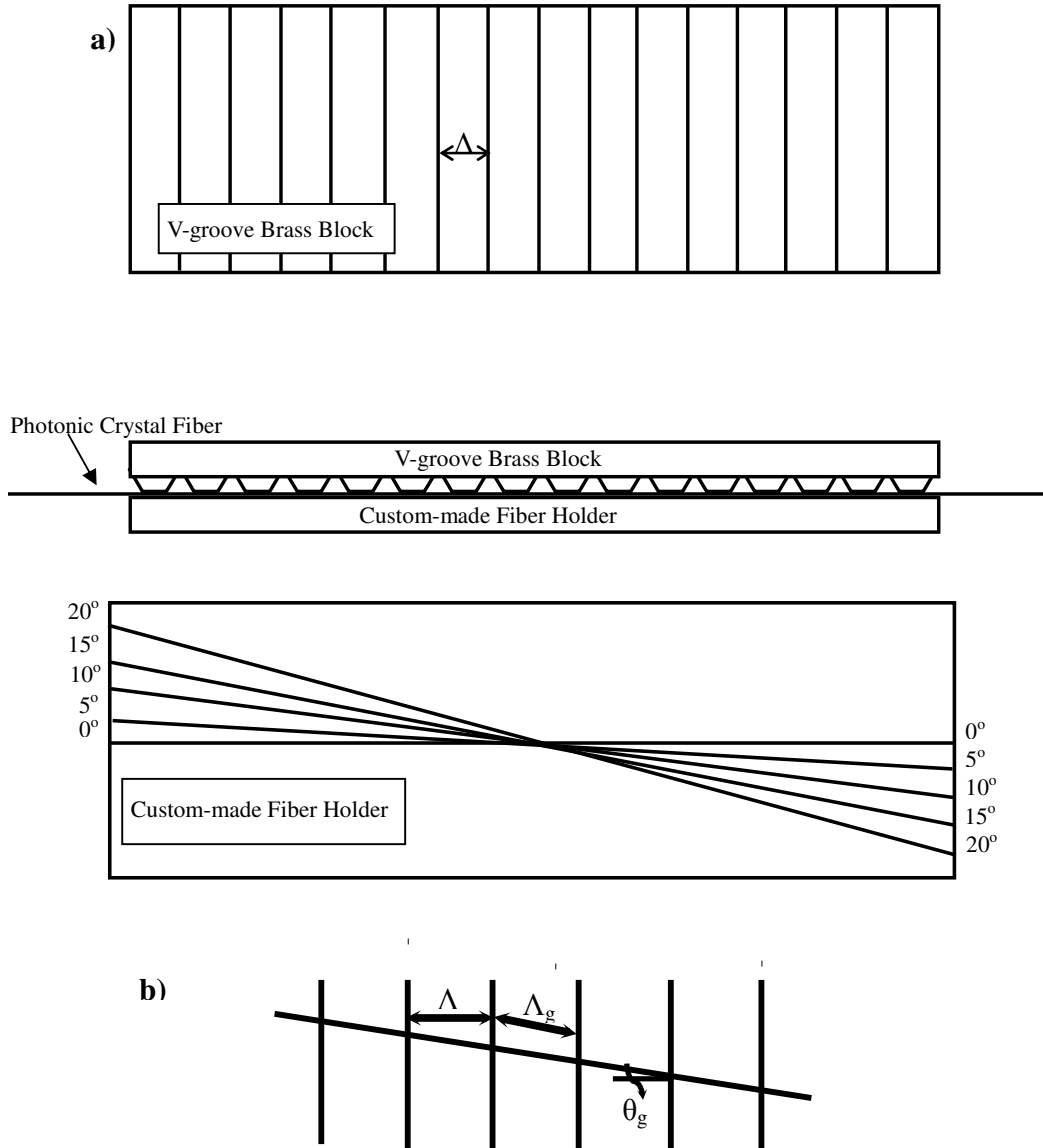


Fig 3.6 a) Grooved fixture and experimental setup for the mechanical long period grating; b) (Top View) the relationship between V-groove pitch and optical fiber grating period.

When the fiber is placed in the fiber holder, with force being exerted on the V-groove brass block, a periodic refractive index perturbation structures with period Λ are formed in the PCF of the brass block region. When the fiber is in the 0° slot, Λ is equal to the

brass block V-groove period Λ_g . When the fiber is placed in other slots of the fiber holder, Λ is no longer equal to Λ_g . As shown in Fig 3.6(b), the relationship between Λ and Λ_g becomes

$$\Lambda = \frac{\Lambda_g}{\cos \theta_g} \quad (3.5)$$

Rearranging the phase matching condition for blazed long period grating

$$\beta_{core} + \frac{2\pi N \cos \theta_g}{\Lambda_g} = \beta_{clad} \quad [71],$$

the relationship between the tilted angles and resonance wavelengths is:

$$\lambda = -\frac{(n_{eff} - n_{clad})\Lambda_g}{N \cos \theta_g} \quad (3.6)$$

where $\beta = \frac{2\pi n_{eff}}{\lambda}$, n_{eff} is the effective index of the core mode, N ($-\infty < N < +\infty$) is an integer that signifies its harmonic order, θ_g is the tilted grating angle, Λ_g is the V-groove block grating period, and n_{clad} is the effective index of the cladding mode that the core mode coupling to.

By taking the derivative of Eq(3.6),

$$\Delta \lambda = K \sec \theta_g \tan \theta_g \Delta \theta \quad (3.7)$$

where $K = -\frac{(n_{eff} - n_{clad})\Lambda_g}{N}$ for a specific resonance wavelength.

External force of sufficient magnitudes is capable of forming grating structure as depicted by the transmission dips in the spectra. In order to have coupling wavelength near 1310 nm, brass black V-groove period 400 μm is chosen. The wavelength dips in the transmission spectrum indicate the loss of light transmission power at that resonance wavelength. This loss is due to the fact that a periodical strain is induced after pressing the V-groove block, resulting periodical refractive index variation in the fiber by photoelastic effect. The light in the core scatters and couples with the forward cladding modes and radiation fields in the cladding. The coupling only occurs when phase matching condition is met.

By placing the fiber in the slanting slots of the fiber holder, blazed grating fringes form in the fiber when pressing the brass block. The angle between the grating pattern and the longitudinal direction of the PCF is the tilted grating angle, θ_g . This tilted grating allows the coupling light from the core to the different orders of co-propagating cladding modes to take place. Generally for the tilted grating angle equals to 0° , the guided LP_{01} can only couple to cladding modes of the same order. When $\theta_g \neq 0^\circ$ the transverse refractive index profile of the fiber becomes asymmetry, which strongly influences the strength of coupling between guided core mode and different order cladding modes [72].

The positions of these transmission dips move towards the shorter wavelength for larger tilted angle θ_g as shown in Fig. 3.7 as expected. According to Eq(3.6) when θ_g increases,

the refractive index modulation Λ in the fiber increases, inducing the blue-shifting of the transmission dip. The transmission dip appears at 1314.079 nm for Λ equals to 400 μm . It shifts to 1304.713 nm and 1288.873 nm when tilted angle increases to 5° and 10° , respectively. The dip further shifts towards blue side to 1258.568 nm and 1215.8878 nm for 15° and 20° respectively. These transmission dip positions meet the theoretical prediction of Eq(3.7) as shown in Fig. 3.8.

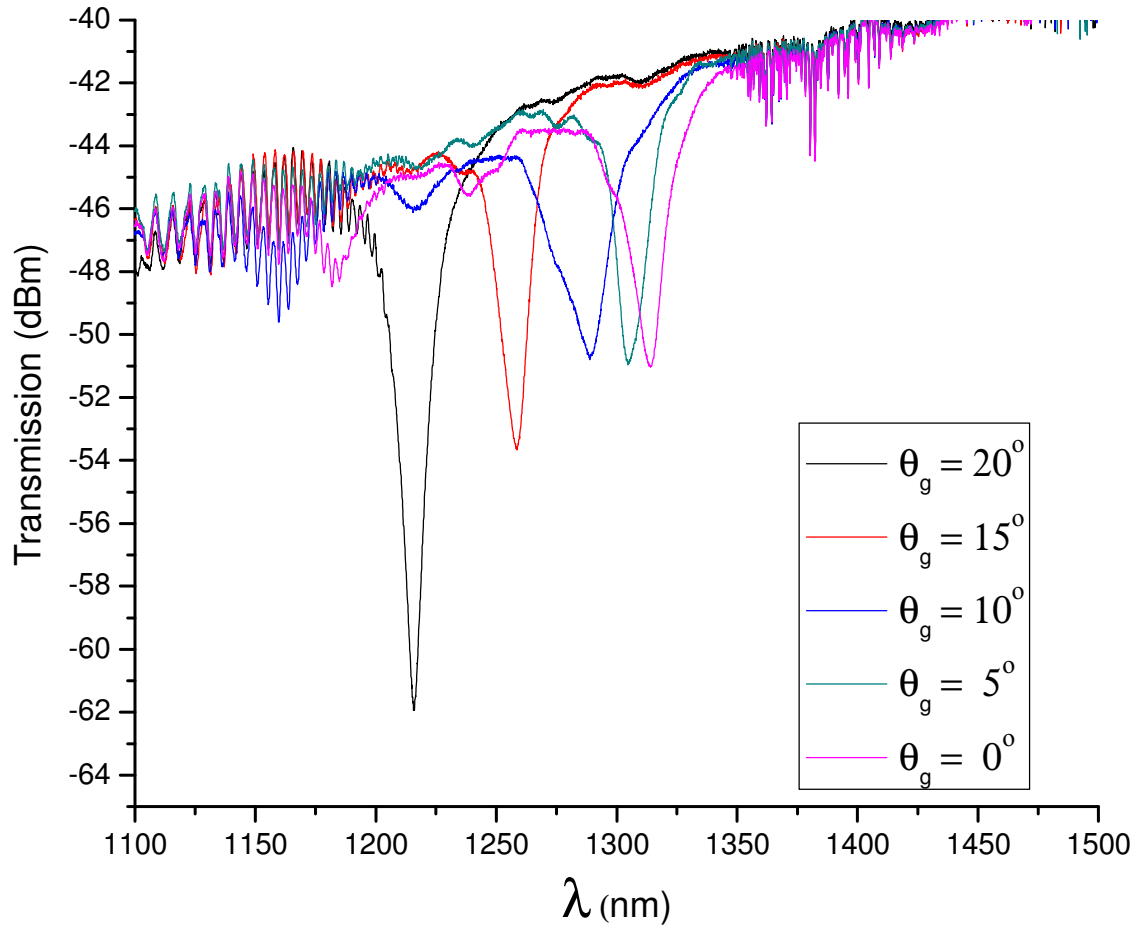


Fig 3.7 Transmission dips at 1320 nm for different tilted angles. It shows that the transmission dip shifts to the blue region when tilted angle increases

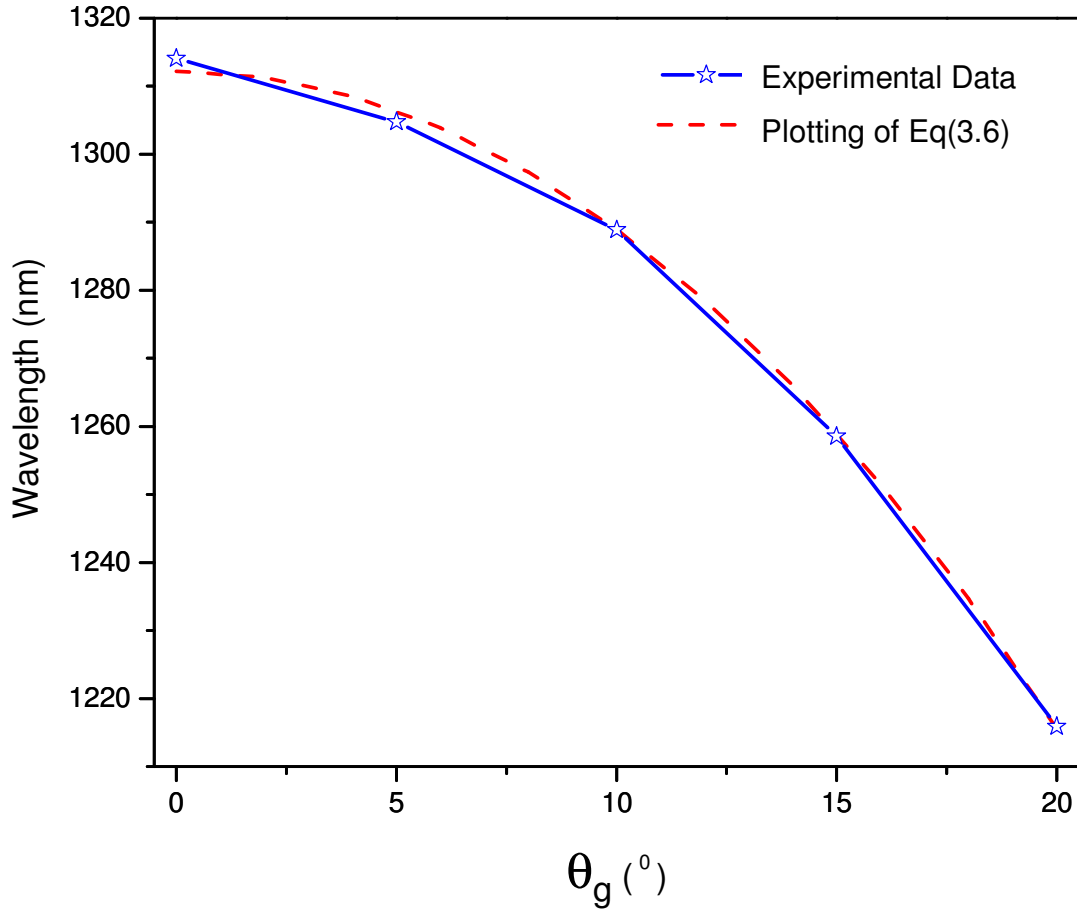


Fig 3.8 Wavelength shifts VS. Tilted angle. The experimental data fits well with the theoretical data

The relationship of $\Delta\lambda$ and tilted angle θ_g is plotted in Fig. 3.9. It shows linear relationship between $\Delta\lambda$ and titled angle. In fact, when θ_g is small, $\sec\theta_g$ is approximate to 1, $\tan\theta_g$ can be approximated as θ_g . Thus Eq(3.7) can be simplified as $\Delta\lambda = K\theta_g\Delta\theta$. It implies that when the angle of the tilted grating is small, the shifting of wavelength caused by the change of the tilted angle is approximately linearly proportional to the angle. The experimental data agrees well with Eq(3.7). A linear curve fitting has been done in Fig 3.9 as well. Eq(3.7) shows good linearity with 0.9981 linear fit R^2 value. This

linearity is useful for measuring the position of the fiber with respect to a fixture when the fiber alignment is extremely important, such as an integrated lab-on-a-chip device.

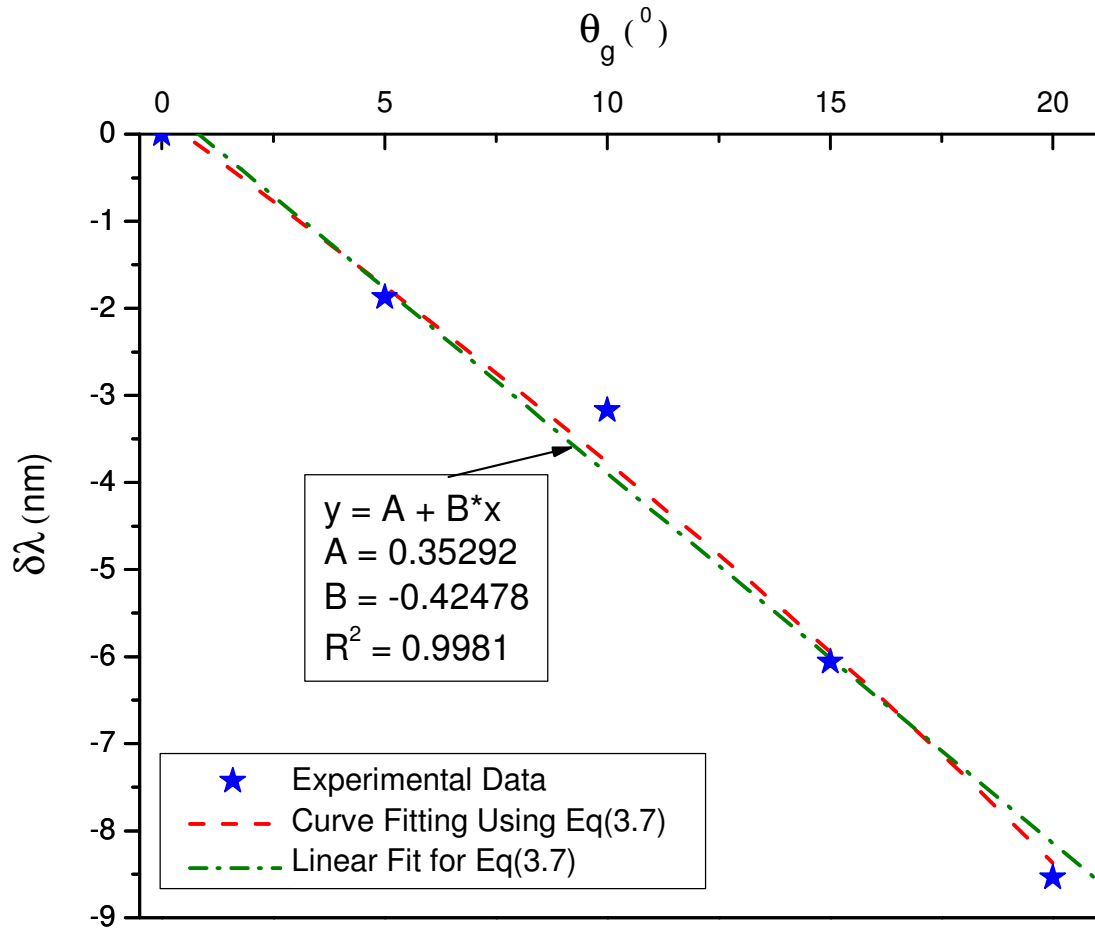


Fig 3.9 When angle is small, $\Delta\lambda$ VS. tilted angle is in linear relationship

3.4 PCF for Temperature Sensing³

In previous session, the light guiding mechanism in PCF is by modified total internal reflection (mTIR), where the effective index of the air-holes cladding is lower than the fiber core. Actually the most fascinating property of PCF is that light is able to travel in the silica core if the air-holes were filled with high index materials. Instead of mTIR, the light is trapped by photonic bandgap effect. Refractive index and other physical sensing are achievable in photonic bandgap fiber as well.

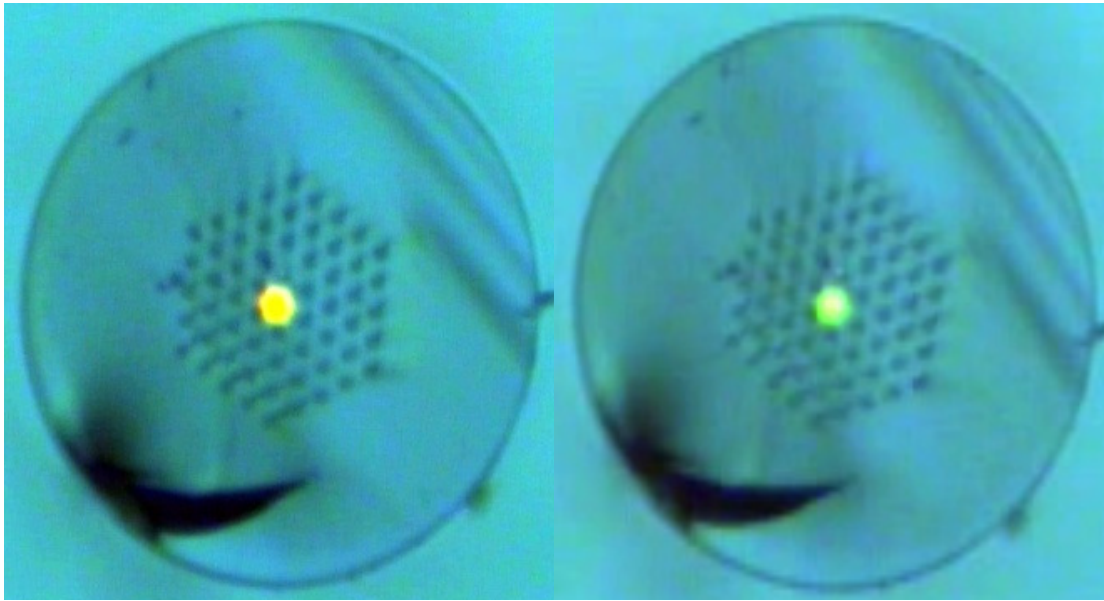


Fig 3.10 Cross section of PCF filled with refractive index oil of 1.46 at a) room temperature b) increase of temperature

³ NOTICE: This is the author's version of a work accepted for publication by ELSEVIER. Changes resulting from the publishing process, including peer review, editing, corrections, structural formatting and other quality control mechanisms, may not be reflected in this document. Changes may have been made to this work since it was submitted for publication. The definitive version has been published in SENSORS AND ACTUATORS A-PHYSICAL, 157, 2, FEB 2010, DOI: 10.1016/j.sna.2009.11.026.

Fig 3.10 shows the cross section of PCF filled with refractive index liquid of 1.46 and the changes of the transmission light color due to the variation of the ambient temperature. However, it is difficult to sense the temperature quantitatively by observing the color of the transmission light. Usually the refractive index of a substance will be influenced if the ambient temperature changes. In the following session, temperature sensing by using photonic bandgap fiber is investigated by making use of the characteristic of the refractive index liquid.

3.4.1 Theoretical Model and Simulations

By filling high refractive index liquids into the air holes of solid core PCFs, the effective index of the holey region will be increased to a level which is higher than its background material, silica. Thus the light guiding mechanism changes from modified total internal reflection to photonic bandgap effect. The position of band-edges is the parameter of interest for our sensing purpose. Its band-edges are a function of the geometry of the fiber and the index contrast between silica and filled holey region. For the same PCF geometry, the refractive index of the filled liquid alters accordingly with the influence of ambient temperature changes. Thus the shifting of band-edges results and it shifts accordingly to the refractive index variation. The wavelength shifts of these band-edges are able to be evaluated by the refractive index scaling law, which is based on scalar waveguide approximation [73-75]. For the geometry profile of the solid core photonic bandgap fiber,

the corresponding shifts for the photonic band-edges varies from λ_o to λ_t , is given by Eq(3.8), when the refractive index of the filling material changes from n_o to n_t due to the change of ambient temperature.

$$\frac{\lambda_t}{\lambda_o} = \sqrt{\frac{n_t^2 - n_s^2}{n_o^2 - n_s^2}} \quad (3.8)$$

where, n_s is the silica refractive index; n_o is the refractive index of the infiltrated high index oil at 24°C; n_t is the refractive index of the infiltrated high index oil at certain temperature.

In general, for a known refractive index liquid, the refractive index will have a constant change of refractive index unit with 1°C rise of temperature[76]. By rearranging Eq(3.8), the relationship between the shifting of wavelength and the changing of temperature is given by

$$\frac{\Delta\lambda}{\lambda_o} = \sqrt{\frac{(n_o + k\Delta T)^2 - n_s^2}{n_o^2 - n_s^2}} - 1 \quad (3.9)$$

where, $\Delta\lambda$ is the shifting of wavelength; k is temperature coefficient; ΔT is the change of ambient temperature in °C.

To visualize the relationship among wavelength shifting, temperature changing and refractive index, Eq(3.9) were plotted with refractive index ranges from 1.46 to 1.66. The graph is as given in Fig 3.11. From the graph, it is obvious that the higher the temperature, the shorter wavelength region that the band-edge shifts to. The higher the refractive index, the flatter the curve is. From that, it could be predicted that lower refractive index liquid infiltration should have higher sensitivity than higher refractive index liquid. This could be proved by comparing the slope of tangent in the curve of $\Delta\lambda$ vs. n_o . At refractive index of 1.64, the slope of the tangent at that particular point is smaller than the tangent at refractive index of 1.52. The relationship between $\Delta\lambda$ and ΔT seems linear in Fig 3.11. However, by close look at the Eq(3.9) the plotting curve in Fig 3.14, especially the line when n_o is 1.52, it is a non-linear curve with very gentle curvature.

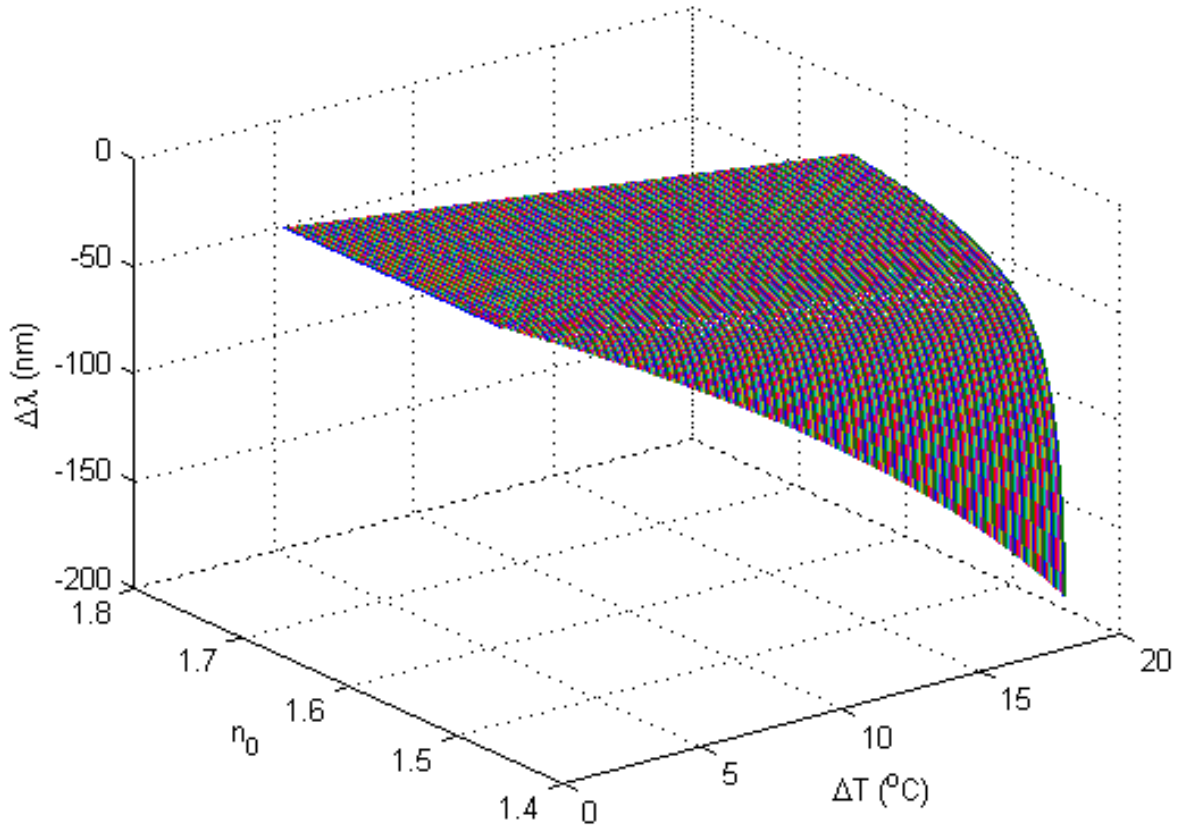


Fig 3.11 Relationships between wavelength shifting under different temperature variation for different refractive index liquid are able to get from the plotting of Eq(3.9).

3.4.2 Experimental Investigation

The schematic diagram of the experimental setup is shown in Fig 3.12. The whole experiment was carried out in a temperature controlled chamber. Light from a PCF-based broadband super-continuum light source (Koheras SuperK Compact), which offers an ultra broad flat spectrum from 600 nm to 1750 nm, was guided using a single-mode fiber SMF-28. The SMF-28 launched light into the core of the high refractive index liquid

filled solid-core PBGF via butt coupling. Two ends of a 20 cm solid-core PBGF were mounted in modified V-groove mounts in order to keep the fiber in place during the measurements. The transmitted light after the PBGF was guided using another section of SMF-28 via butt coupling. The two SMF-28s were mounted at a XYZ three dimensional translation stages which were adjusted to maximize the power collected from the fiber core. To visualize the optimized alignment, two CCD cameras were mounted at each butt-coupling point. Light transmitted from second SMF-28 was measured by optical spectrum analyzer (OSA, ANDO AQ6317B).

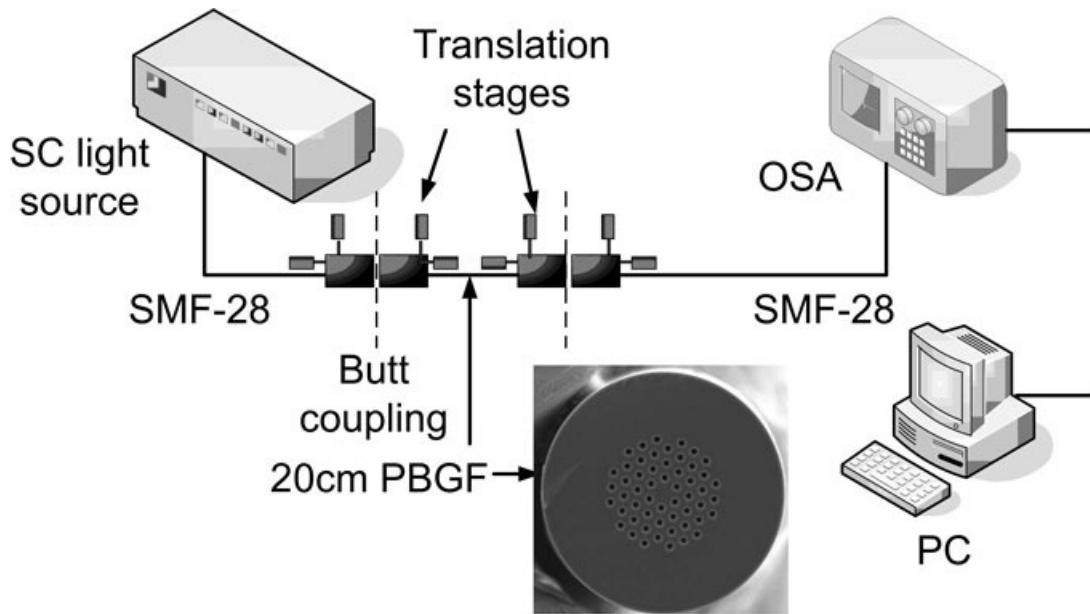


Fig 3.12 Schematic diagram of the experimental setup (SC Light Source: Supercontinuum Light Source; OSA: Optical Spectrum Analyzer; PBGF: Photonic Bandgap Fiber (solid core))

The solid-core PCF is from Crystal Fibre A/S. The cross section of this fiber is as shown in Fig 3.12. It consists of a solid silica core with core diameter of 12 μm which is

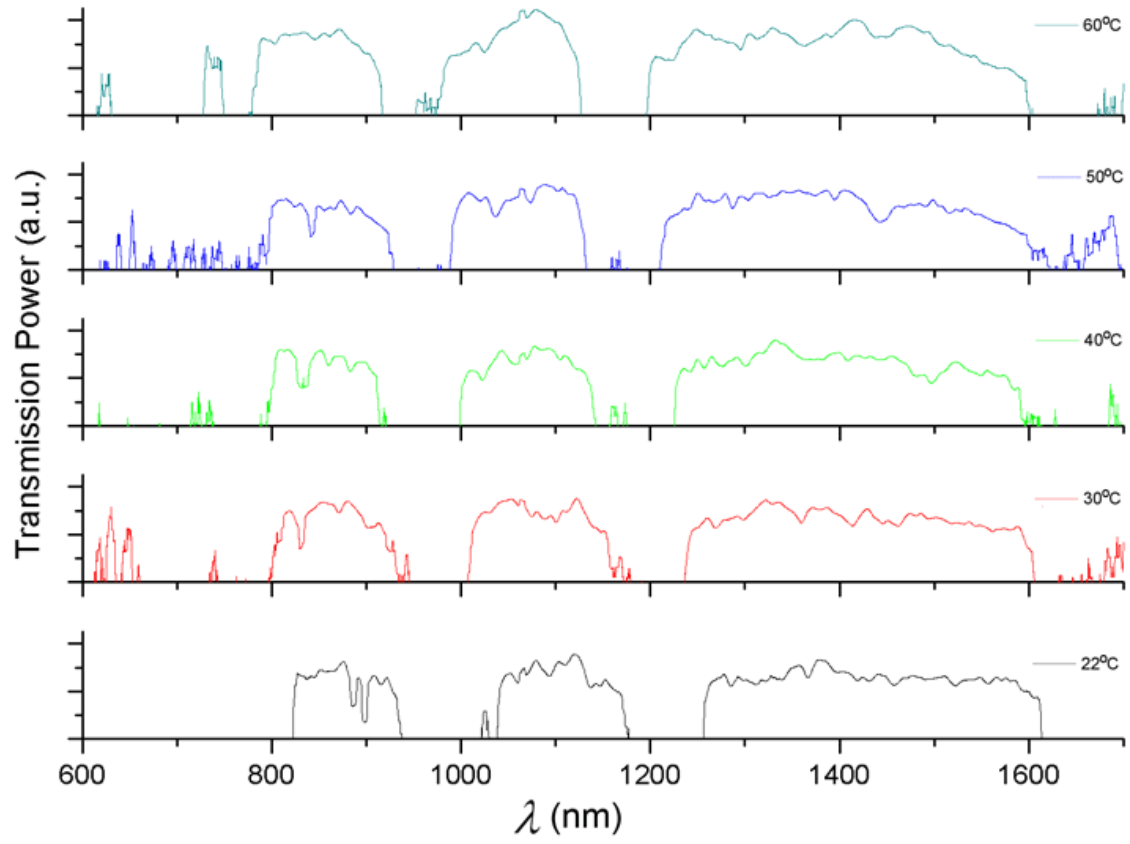
surrounded by four rings of circular air holes in a triangular lattice. The distance between the adjacent holes (pitch) is 8 μm . The refractive index of the background material, n_s , silica is 1.45. The ambient effective index inside the holey region is determined by the refractive indices of infiltrated liquids.

Because the bandgaps are determined only by the microstructure in the transverse direction, the length of the fiber should not shift the position of the band-edge. This has been proven experimentally[77]. However, the increment of the fiber length may result loss increment outside the bandgaps. To avoid certain loss, all fibers sample lengths in this experiment were kept at 20 cm.

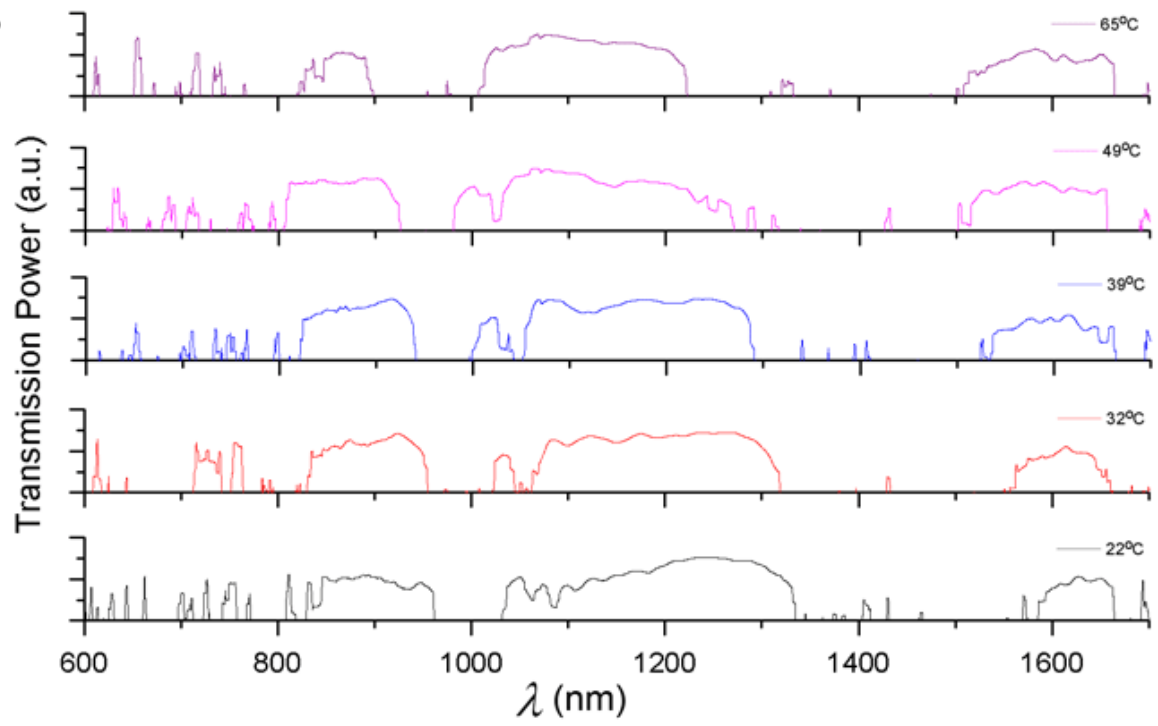
Three high refractive index liquids (Cargille Labs, temperature coefficient is $-0.0004/^{\circ}\text{C}$) with refractive index 1.52, 1.58 and 1.64 were infiltrated into solid-core PCF separately by pressure injection. According to Navier-Stokes equation, filling this 20 cm PBGF is about 10 minutes' time [78]. And it is also possible to fasten the filling process by applying external pressure at one end of the fiber [78]. The high refractive index liquids were filled into fibers by creating pressure difference at two ends of the fiber. Thus the whole infiltration process took less than 5 minutes. The fibers were observed under microscope to ensure that the whole fibers were fully filled before putting into the temperature controlled chamber. To avoid contamination, a new section of fiber was used for each high refractive index liquids infiltration.

The high index oils which have the refractive index of 1.64, 1.58 and 1.52 at 1550 nm and 24°C are used to determine the wavelength shifting sensitivities of the PBG temperature sensor. The corresponding calibrated refractive index accuracy for each liquid is ± 0.002 RIU. The normalized transmission spectra taken at different ambient temperature are plotted together and shown in Fig 3.13. In the normalized transmission spectra, the wavelengths of rising PBEs of first photonic bandgap are taken into consideration. Two kinds of phenomenon are able to be observed from these transmission spectra. First, all transmission windows of high refractive index liquid 1.64, 1.58 and 1.52 shift to a shorter wavelength when temperature increases. That is because the temperature coefficient of the high refractive index liquid is $-0.0004/^{\circ}\text{C}$. Thus rising of temperature induces decreasing of the refractive index of the high index oil. When the refractive index decreases, the transmission windows shifts to a shorter wavelength [77]. Secondly, with the increasing of the temperature, the transmission window becomes noisier, which is also the reason that the liquid refractive index inside the solid core PCF is fluctuating when this measurement is taken place. Therefore, refractive index stabilizing time should be taken into consideration during measurement. Measurement should only be taken after the high refractive index liquid temperature is in equilibrium state with the temperature of the controlled chamber.

(A)



(B)



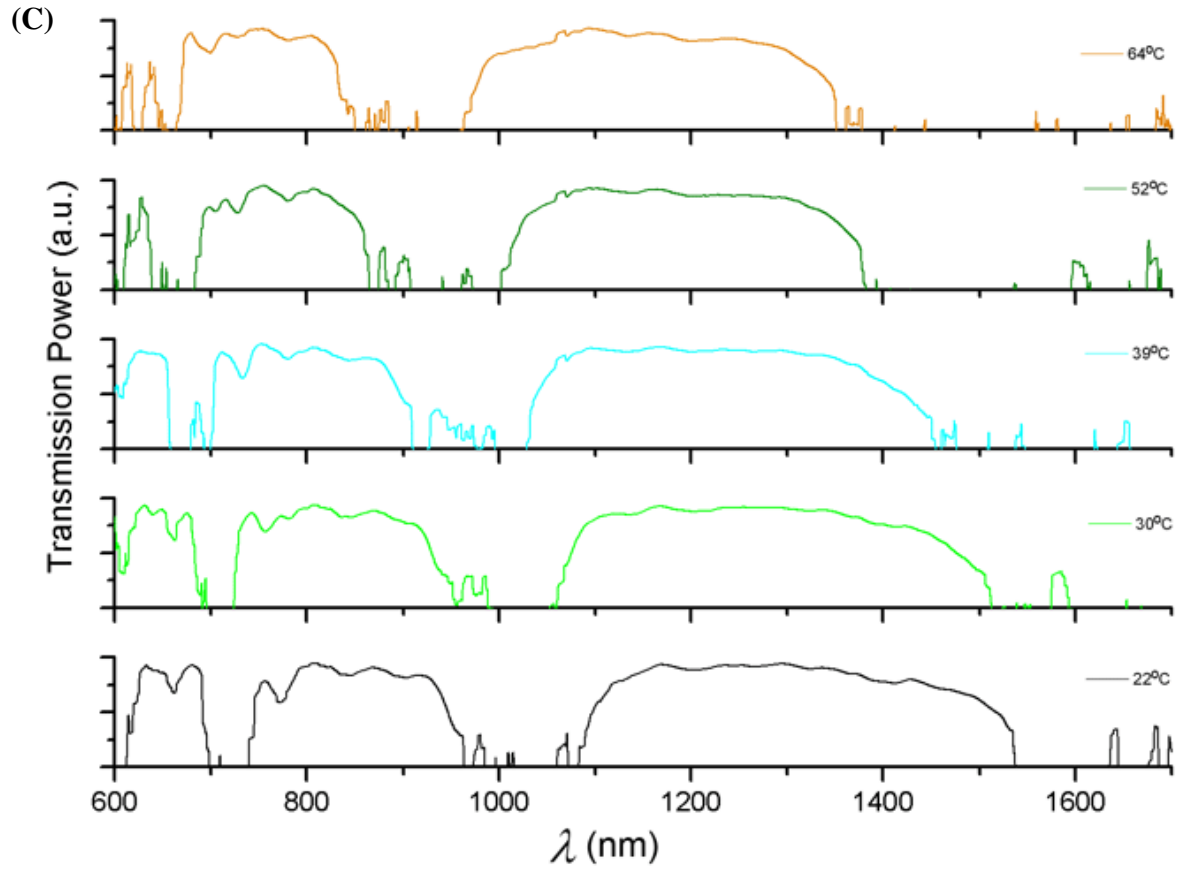


Fig 3.13 Normalized spectra of solid core PBGF with high refractive index liquid infiltration of 1.64, 1.58 and 1.52 under temperature variation as shown in (A), (B) and (C). The highest spectrum at each graph indicated the spectrum at highest temperature, whereas the lowest indicated the spectrum at 24°C. Blue shifting of transmission windows are observed.

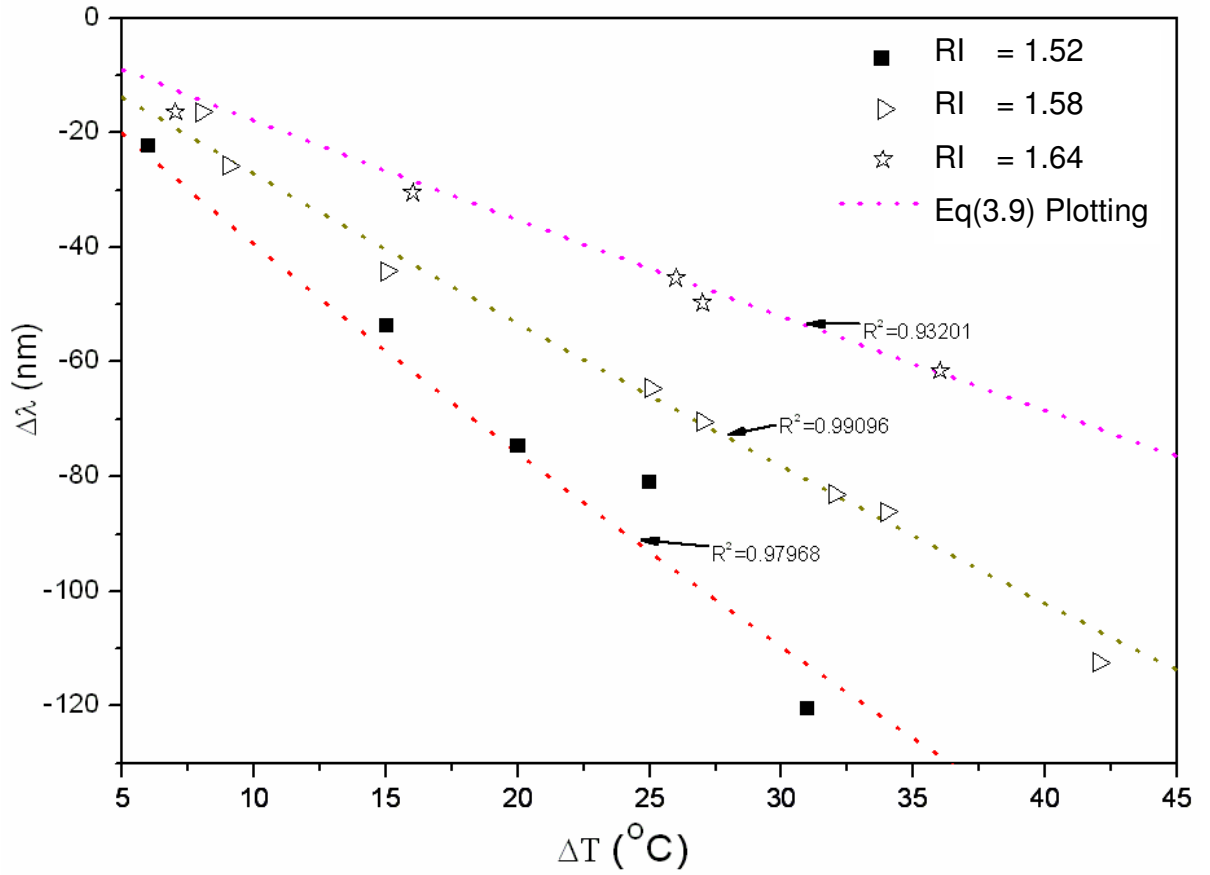


Fig 3.14 Wavelength shifts of PBEs plotted as a function of ambient temperature changes.

Data are extracted from the spectrum and plotted according to $\Delta\lambda$ and ΔT as shown in Fig 3.14. Eq(3.5) when n_o of 1.52, 1.58 and 1.64 are plotted in dotted line. Experimental data are fitted into the curves. Most experimental data shows good agreement with the curves with Pearson's coefficient of regression (R^2 Value) indicated in the graph. All R^2 values are close to 1 which indicates that they have a better fit. There is only small discrepancy between most data.

With wavelength shifts from 1255.87 nm to 1194.34 nm, the ambient temperature

changes from 24°C to 60°C. Thus, the wavelength shift of the PBEs under temperature variations for RI of 1.64 is approximated to be 1.71 nm/°C. For RI of 1.58, wavelength shifts from 1335.00 nm to 1222.60 nm when temperature varies from 24°C to 65°C. The sensitivity for RI of 1.58 is 2.74 nm/°C. For RI of 1.52, wavelength shifts from 1082.97 nm to 962.46 nm when temperature varies from 24°C to 64°C. The sensitivity for RI of 1.52 is 3.01 nm/°C. This shows good agreement with the prediction in the simulation that the lower refractive index liquid has higher sensitivity than the higher refractive index liquid.

A practical consideration is the boiling points of infiltrated index liquid, which may affect the usage of this PBG temperature sensor. When temperature goes too high, the boiling point of the index liquid can be reached. The refractive index of the liquid would be fluctuating when it starts boiling. In this experiment, these high refractive index liquids with the initial boiling points well above our highest testing temperature are chosen to avoid the refractive index fluctuation. Moreover, for the temperature of index liquid to reach equilibrium state as in the temperature control chamber, stabilizing time is needed to take into another practical consideration. Calibration is needed to be carried out before experiment starts. In this experiment, five minutes of stabilizing time was spared for each measurement to make sure that the temperatures between air-holes and chamber are in equilibrium. The shortest stabilizing time is needed for further investigation.

This work provides an alternative for temperature sensing by using PBG effect. It avoids the inconveniences of writing grating in optical fibers, especially for grating in photonic crystal fiber, and yet provides higher sensitivity than un-doped optical fiber sensors. The detectable temperature variation is limited by the resolution of the demodulation technique. If the minimum spectra variation of the measurement system is 0.01 nm, $3.32 \times 10^{-3} \text{ }^{\circ}\text{C}$ could be detected in this experiment. Doping of temperature sensitive phosphor into the fiber could also be considered to increase temperature sensitivity[79]. It could be used together with a PBG biosensor as a reference to compensate refractive index variation induced by temperature fluctuation[80].

3.5 Refractive Index Sensing Realized by Polymer Coating⁴

PCFs are typically made from pure silica with the advantage of lower loss. More recently polymer PCFs have been proposed and fabricated[81]. Certain polymer PCFs possess one advantage over silica for the purpose of biosensing. They have good compatibility with biological substances[82]. However, fabrication of polymethyl-methacrylate (PMMA) PCFs remains a high-cost production. To achieve similar biocompatibility in relatively lower-cost silica-core PCFs (SCPCF) and make use of photonic bandgap effect as sensing

⁴ NOTICE: This is the author's version of a work accepted for publication by SPIE. The definitive version has been published in Proceedings of SPIE, 7134, 713442, 2008.

mechanism, simulation on high refractive index polymer coating in SCPCF air-holes is proposed in this section.

3.5.1 Numerical Analysis and Verification

The photonic crystal fiber cross section is shown in Fig. 3.15. It consists of a solid core with diameter D and five rings of circular air holes in triangular lattice. The diameter of air holes, thickness of coating and pitch are d , d_p and Λ respectively.

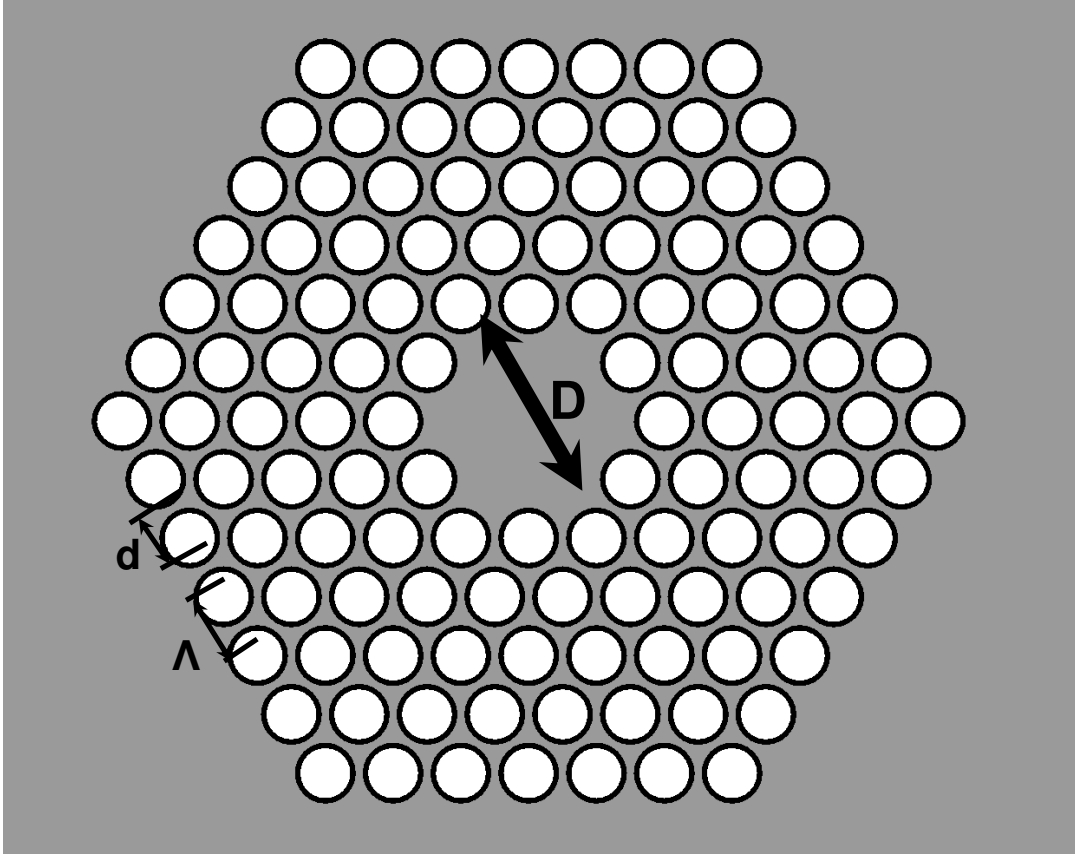


Fig 3.15 PBGF with air holes arranged in triangular lattic.

In order to evaluate the polymer coating effect, a three-layer model of air hole is proposed. The three layers include (1) background material with refractive index (RI) n_s , (2) polymer coating with RI = n_p , and thickness of d_p ($d_p = (d - d_a)/2$), (3) air filling portion with RI = n_a , and diameter of d_a . The schematic of the model and refractive index profile are illustrated in Fig. 3.16.

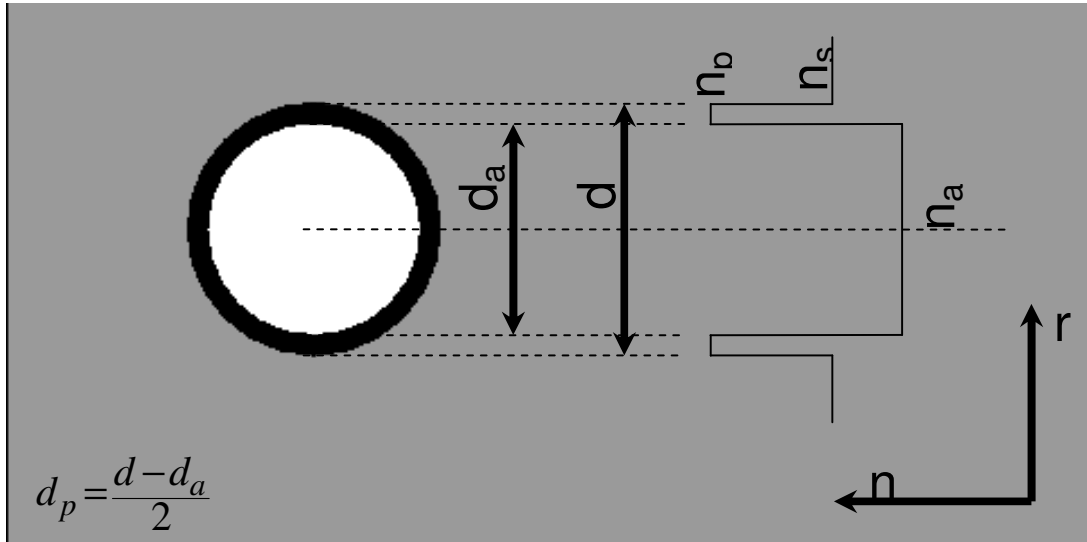


Fig 3.16 Schematic of cross section and refractive index profile.

The wavelength shifts of photonic bandgap edges were evaluated by plane wave expansion method, assuming n_s , n_p and n_a are 1.45, 1.50 and 1.00 respectively. The photonic crystal fiber in this simulation has a ratio for hole-diameter (d) to cladding pitch (Λ) (i.e. $d/\Lambda = 0.875$). Air ratio (AR) is defined as d_a/d .

Three parameters of interest for this photonic crystal fiber are coating thickness of the

polymer forming photonic bandgap effect and the positions and bandwidths of bandgaps. These three parameters are influenced by air-filling ratio and refractive index contrast between silica and polymer coatings. Filling the holes of such fiber with different thickness of polymer will change air-filling ratio and therefore shift the band gaps and their corresponding bandwidths.

When biorecognition element is immobilized on the inner surface of the holey region of photonic bandgap fiber (PBGF), the PBGF sensor is able to distinguish different solutions with different refractive index [83]. It has been demonstrated that human IgG could be detected by using goat IgG as biorecognition element [84]. For easy immobilization of biorecognition element, a layer of polymer is coated inside the holey region. Light guiding mechanism changes from index guiding to photonic bandgap effect after polymer coating with certain thickness. The formation of photonic bandgap is influenced by the polymer layer thickness and the sensitivity can be estimated by considering the shifting of photonic band-edge after polymer coating.

It has been demonstrated that uniform coating is able to be achieved experimentally by using high-pressure microfluidic chemical deposition [85]. Thus we assume that the polymer film deposited onto the holes is uniform. The waveguide loss induced by the polymer coating is minimized. The ratio between polymer thickness and air hole diameter is considered to investigate the photonic bandgap effect. Two extreme cases are

considered, one is with zero air filling ratio ($AR = 0$), which means air holes are fully filled with polymer. The other one is with large air filling ratio, which indicates a thin polymer coating ($AR = 0.9$).

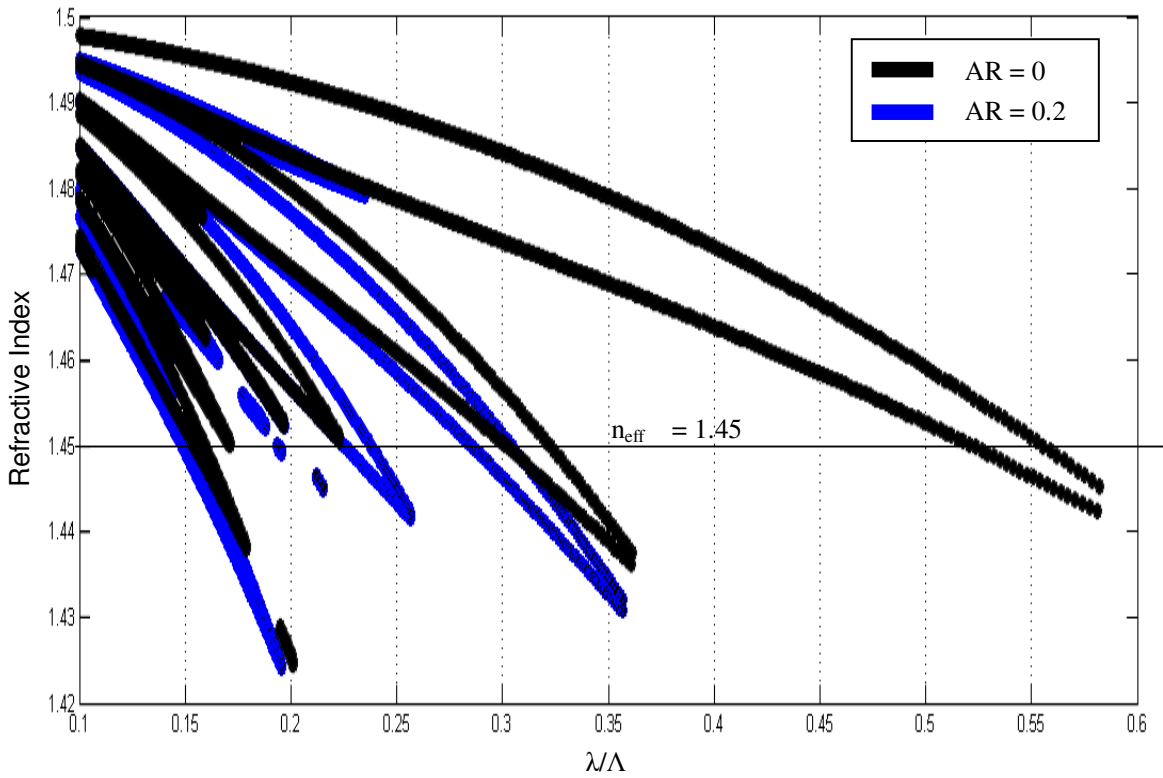


Fig 3.17 Gap map for $AR = 0$ and $AR = 0.2$.

Fig. 3.17 represents the comparative gap maps for $AR = 0$ and $AR = 0.2$. The wavelength range for light guiding inside silica core can be easily identified, which are the spans where the core line ($n_{eff} = 1.45$) crosses the gap regions. Blue shifting of bands are observed and the bandwidth of each bandgap becomes narrower with the increasing of air

ratio. Bandgaps are bounded between refractive index 1.43 and 1.50, which are approximately refractive indices of silica and polymer.

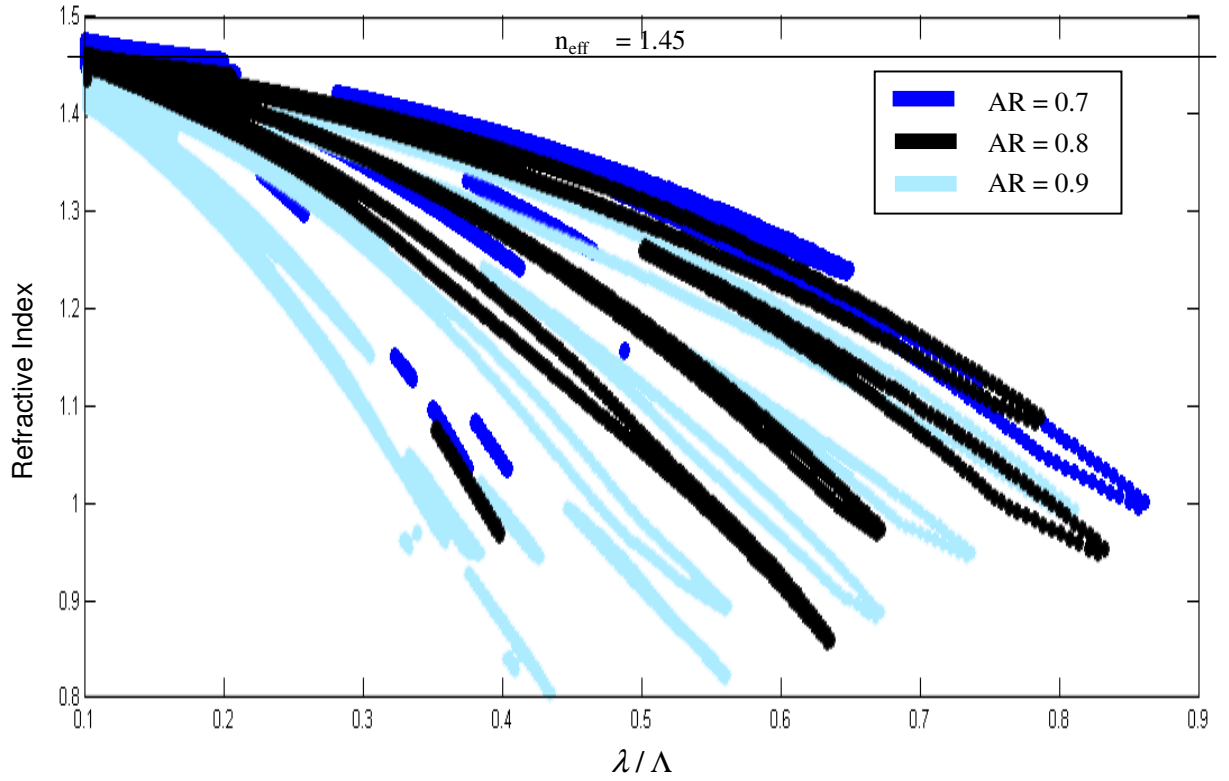


Fig 3.18 Gap map for AR from 0.7 to 0.9.

Further decrease of the coating thickness leads to no significant available band, as in the case of $AR = 0.8$ in Fig. 3.18. At $AR = 0.9$, there is no photonic bandgap effect at $n_{eff} = 1.45$. This implies that to observe photonic bandgap phenomenon in silica-core photonic crystal fiber with polymer coating, the minimum coating thickness should be $AR = 0.7$.

Furthermore, the bandwidths in Fig. 3.18 appear much narrower than in Fig. 3.17. Bandgaps shift further to blue region with the decreasing of polymer coating thickness. Moreover, the guided wavelength span also shrinks. This is because when polymer thickness becomes very thin, effective index in air holes approaches to air refractive index. Thus the generated bands will be constrained within the range of RI from 1 to 1.45.

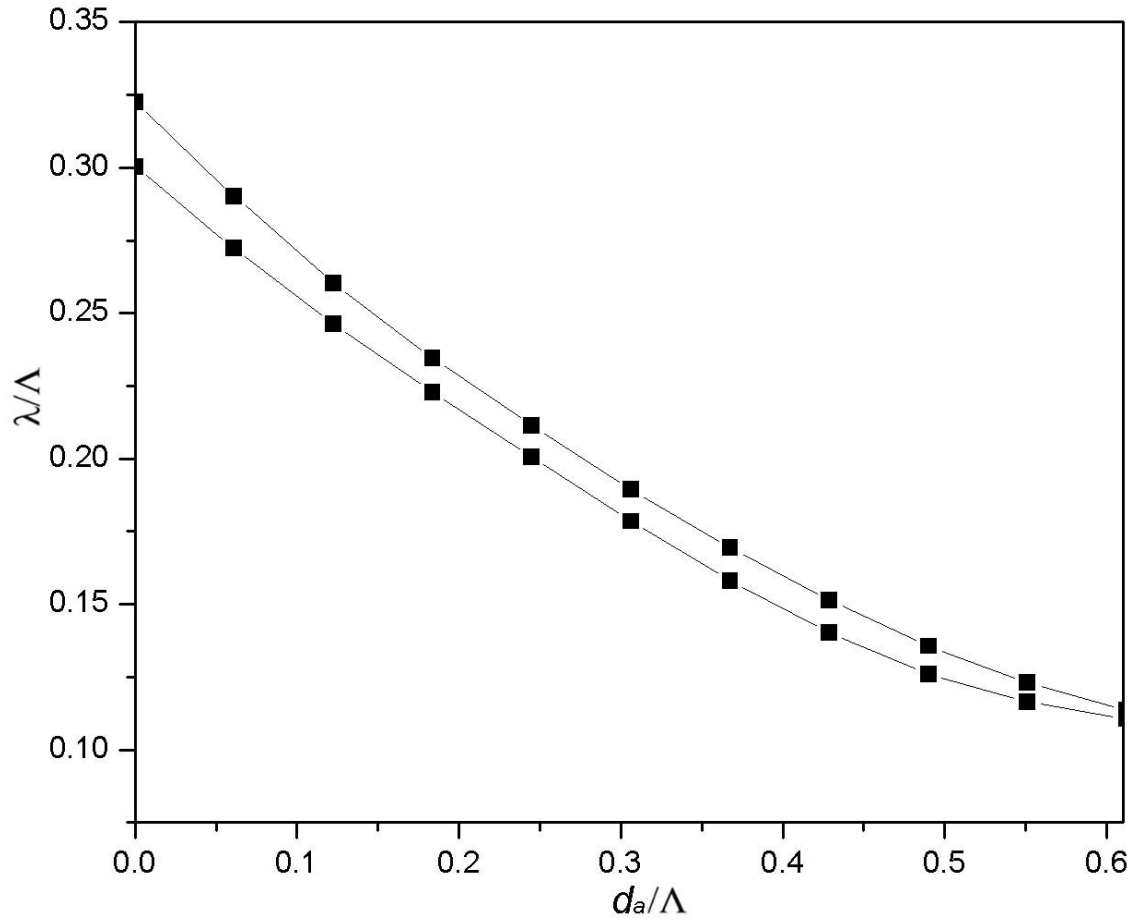


Fig 3.19 Band map for $AR \leq 0.7$.

The wavelength ranges for guiding light inside silica core as function of d_a/Λ are shown in Fig. 3.19. The sensitivity is estimated by considering with $d_a/\Lambda = 0.1$. The result shows that d_a change of 1 nm is able to obtain a wavelength shift of 0.43 nm [86]. Assuming the wavelength shift of 0.01 nm can be detected, a small d_a variation of 0.023 nm can be measured. It is obvious that the main advantage of this photonic bandgap fiber sensor is to provide high sensitivity for measuring air hole variation, which results from the large wavelength shift of photonic band edges with respect to the variation. In addition, this device is also robust because of the biocompatibility of the polymer layer. The immobilization of specific biomolecule becomes easier and hence more reproducible. Thus PBGF-based sensor can be developed for detecting specific targets by immobilizing particular detecting molecules on the polymer layer. Furthermore, the PBGF biosensor has the merit of small volume sample consumption, which is less than 1 μL [77].

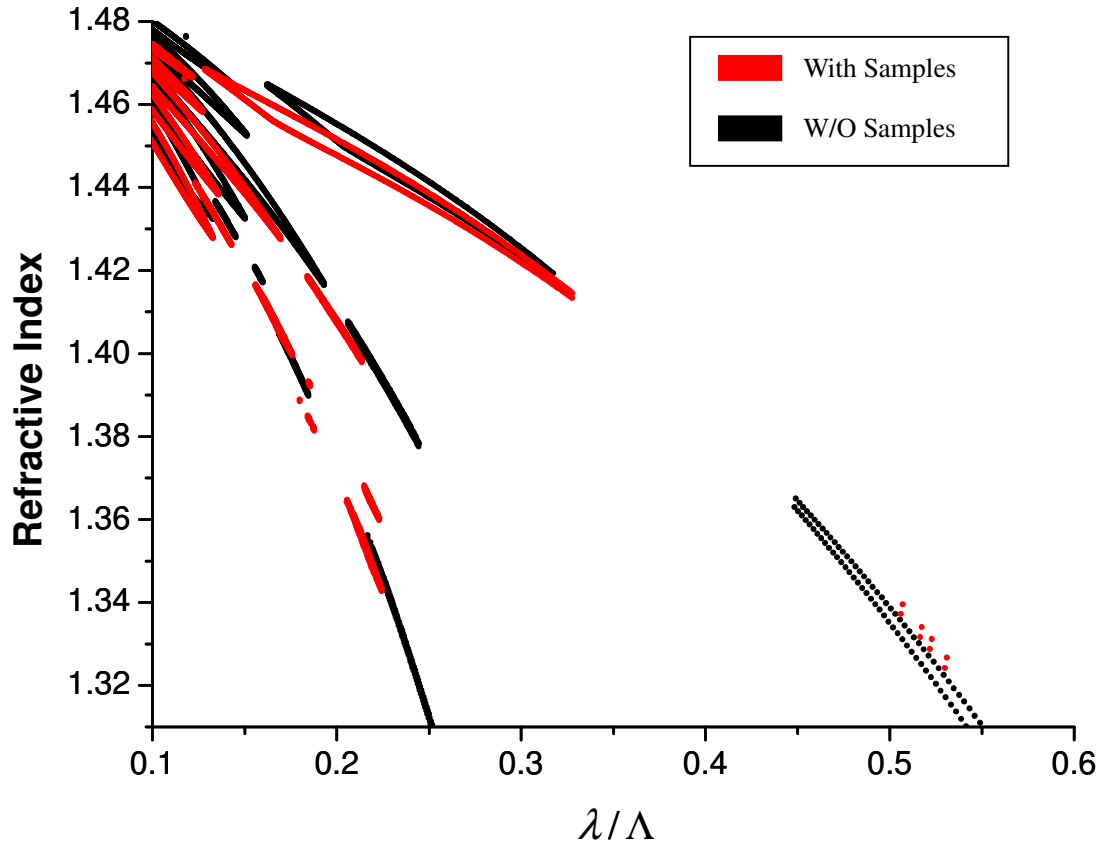


Fig 3.20 Gap map with and without filling of biological samples.

The analyte solution could be filled into the air-holes of the photonic crystal fiber after coating. Any changes of the analyte refractive index in the air-holes could be observed by photonic bandgap shifting. The red gap-map in Fig. 3.20 indicates the map after filling solution $RI = 1.35$ into air-holes of polymer-coated (with $AR = 0.6$) photonic crystal fiber. Usually the refractive index of biological solution is less than 1.45. Thus this could be represented as specific biological solution. With the changes of the biological solution concentration, the refractive index should be changed. From the gap-map, after filling of solution with lower refractive index than $RI = 1.45$, the bandgap appears red shifting.

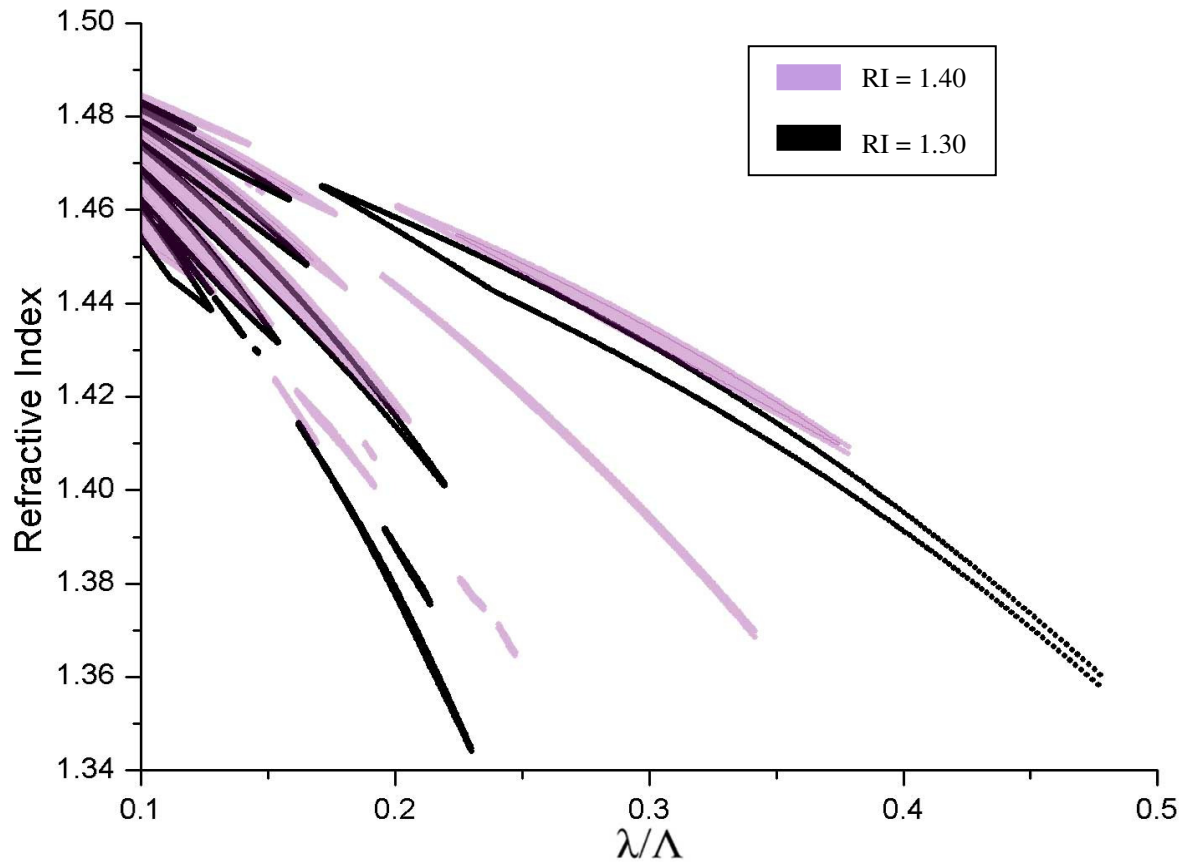


Fig 3.21 Gap map for filling of biological solution with lower refractive index.

The refractive index variation of the solution incurs bandgap shifting. The bandgap continues red shifting with the increasing of the refractive index of the solution from 1.30 to 1.40 as shown in Fig. 3.21.

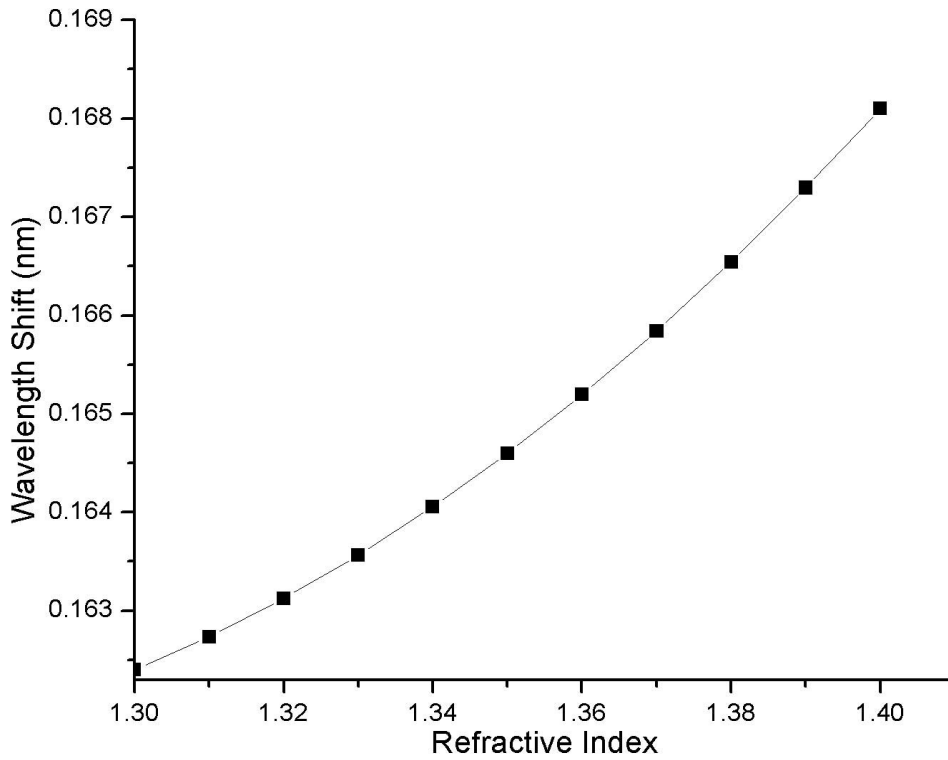


Fig 3.22 Wavelength shift of the falling PBE as a function of biological solution refractive index.

Further investigation proves that the shifting of wavelength is about 0.0065 nm, if the changing of surrounding refractive index is 0.1 when AR is 0.6 as shown in Fig. 3.22. Even though the wavelength shift of the falling photonic bandgap edges and surrounding biological solution refractive index is approximately linear relationship, the PBG fiber with AR = 0.6 polymer-coating is not so sensitive to surrounding refractive index change as our previous simulation work [86]. Thus the thickness of polymer coating is crucial so that the sensor could benefit from the high sensitive photonic band edge shifting without compromising the sensitivity.

There is one important practical consideration. The minimum detectability of analyte may be limited by temperature effects too. Based on the knowledge that the temperature coefficient for liquid is around $-0.0004 \text{ RIU/}^{\circ}\text{C}$, the wavelength shift of the falling PBE under temperature variation is approximated to be $2 \text{ nm/}^{\circ}\text{C}$. Therefore, it is necessary to perform the experiment in a temperature-controlled environment. On the other hand, it has been demonstrated that the evanescent wave is only intense at the silica-solution surface and vanishes completely after a short distance from the surface [87]. Therefore, in close proximity to the inner surface of the holey region of the PBGF, i.e., the coated polymer layer, the band gaps are most likely to be influenced significantly by the refractive indices, rather than the average refractive index in the pores.

3.6 Chapter Summary

In this chapter, optical fiber for sensing has been investigated. Long period grating optical fiber has been used to detect glucose concentration with sol-gel technique. To increase the sensitivity, PCF is recommended owing to the fact that the sample is closer to the fiber core if infiltrated into the air holes surrounding the PCF. Other than that, grating structure can also be inscribed inside the PCF. However, the inscription in PCF is not an easy task. Thus inscribing LPG with the effect of substantial pressure on the PCF in the presence of a V-groove block is suggested. These LPGs couple light from the core mode to the cladding modes at the resonance wavelength. By manually controlling the

mechanical fixture, tilted grating structure can also be formed. The position of the fibers to the V-groove plates has formed tilted long period gratings (LPGs) that are diagonally inscribed in the fibers. This tilted grating allows the light coupling from the core to the co-propagating cladding modes to take place. The resonance wavelength appears to blue-shift when the tilted angle, θ_g , increases.

Besides measuring pressure, PCF can be used in temperature measurement as well. By infiltrating high index liquid into the airholes of PCF, the light guiding mechanism can be transformed into photonic bandgap guiding. The photonic band-edge shifts when the ambient temperature changes. It shows that with increase of temperature, the photonic band-edge appears blue shifts. The sensitivities are different for different refractive index liquid infiltrated. Higher sensitivity could be achieved by filling lower high-refractive index liquid.

Another way to utilize the PCF air holes is to coat the air holes surface with certain substance that could provide other opportunity for PCF sensing. Simulation of coating high refractive index polymer on the surface of PCF airholes has been done as well. Coating polymer on the air hole surface can improve the bio-compatibility and the affinity of enzyme immobilization. By coating high index polymer, the light is confined by photonic bandgap effect. Meanwhile, the simulation also indicates that for the polymer coated PBG fiber to be used as refractive index sensors, the air filling ratio of the coating

must be higher than 0.6.

In this chapter, PCF are used as transducer for direct sensing. In fact, PCF can do more than that. In the following chapter, tuning properties can be obtained by infiltrating liquid crystals into the air holes. With the additional tuning properties, PCF will have the potential to be integrating into lab-on-a-chip device not only as a waveguide or a transducer but also as a switch simultaneously.

Chapter 4

Properties of the Photonic Liquid Crystal Fiber

4.1 Introduction

Similar to traditional optical fiber, external application of mechanical forces can change the refractive index profile of the fiber. Besides that, the air-holes of the PCFs provides more means for refractive index profile modification, such as infiltrating different liquids into the air-holes and coating of the air-holes with certain materials. All the approaches can change the mode field diameter of the PCFs thus provides different opportunities for optical sensings. These approaches have been covered in Chapter 3. Actually since the invention of photonic crystal fibers, a variety of investigations have been carried out to identify suitable materials to infiltrate into the air holes. These materials include gases and fluorescent dyes[78,82,86]. PCF is competent as a sample carrier that can guide light over a long distance. However, PCF can do more than it claimed by integrating interesting materials in its airhole channels. In recent years, it has been identified that liquid crystals are one of the interesting class of materials to infiltrate the PCF[89]. The presence of the liquid crystals provides a mean of tunability and controllability to the fiber. Its high birefringence with wide range of refractive indices and dependencies on

temperature and electric field can make it an interesting material to be used for different applications.

The presence of liquid crystal in a PCF transforms the fiber into one known as the photonic liquid crystal fiber (PLCF). The liquid crystal molecules generally align parallel to the fiber longitudinal axis due to their permanent dipole moment after infiltration[89]. The propagation of light, being an electromagnetic wave, is dependent on the direction of the axis of the liquid crystal molecules. Consequently, the orientation of the liquid crystals can be altered by changing surrounding temperature or using an external electric field to influence the light transmission through the fiber. Thus in this chapter the temperature and electrical effect on photonic liquid crystal fibers will be investigated.

4.2 Effect of External Electrical Voltage on Photonic Liquid Crystal Fiber

4.2.1 Electro-optics of Nematic Liquid Crystals

Liquid crystal molecules are elongated in shape as such that they are optically anisotropic. In general their optical refractive index profiles are represented as elliptical in shape. And the refractive indices in x , y and z directions are denoted as n_x , n_y and n_z , respectively. Usually the z axis is the director axis, which is the axis of symmetry. In uniaxial crystals such as nematic liquid crystal, the refractive index in x axis is the same

as in y axis, thus the refractive index z axis is denoted as n_e and x, y axes as n_o , which o stands for ordinary and e for extraordinary.

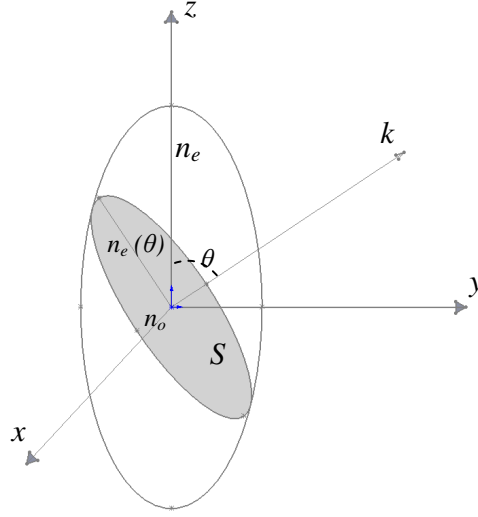


Fig 4.1 Ellipsoid representation of Liquid crystal molecules

If light travels along direction k at an angle θ with the director axis, the plane passes through the origin and is perpendicular to k . There are two orthogonal polarization vectors in the plane. One of the vectors is in the x - z plane and the other one is in the y - z plane. The refractive indices for the two vectors in the molecules are defined as $n_o(\theta)$ and $n_e(\theta)$, respectively. $n_o(\theta)$ and $n_e(\theta)$ are defined as the shortest and the longest axis in the plane S .

From Fig 4.1, it can be found that $n_o(\theta)$ is independent of the propagation angle, which is

$$n_o(\theta) = n_o \quad (4.1)$$

However, $n_e(\theta)$ is related with the propagation angle θ [88].

$$n_e(\theta) = \frac{n_e n_o}{\sqrt{n_e^2 \cos^2(\theta) + n_o^2 \sin^2(\theta)}} \quad (4.2)$$

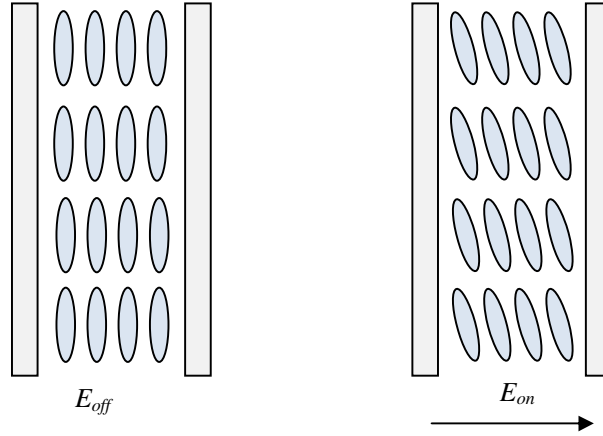


Fig 4.2 Liquid crystal re-orientation upon voltage application

As described above, liquid crystals are elliptical in shape. Thus they are optically anisotropic. As such, they have some interesting properties which are largely affected by their anisotropic nature. Their physical properties are dependent on the direction and the alignment of their molecules. In general, upon application of an external electrical field, the orientation of liquid crystals will be perturbed, giving rise to the changes of the optical refractive index as shown in Fig. 4.2.

4.2.2 Experimental investigation

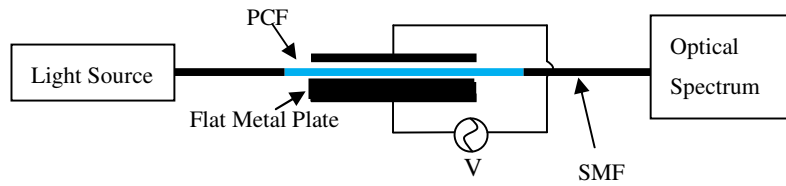


Fig 4.3 Experimental Setup

The experimental setup is illustrated in Fig 4.3. In the experiment, 20 cm of the fiber was used. Liquid crystals (E7) were infiltrated into the fiber by capillary force. The infiltration length was controlled at about 2 cm. After LC infiltration, the two ends of the PCF were spliced with the single mode optical fiber. The fusion power and time were optimized to minimize the collapse of PCF air holes and reduce transmission power loss. One end of the single mode fiber pigtail was connected to a super-continuum light source and the other end was connected to an optical spectrum analyzer. The PLCF region was placed between a metal plate and an electrode. The electric field was applied by using a high voltage power generator which operating at 1 kHz.

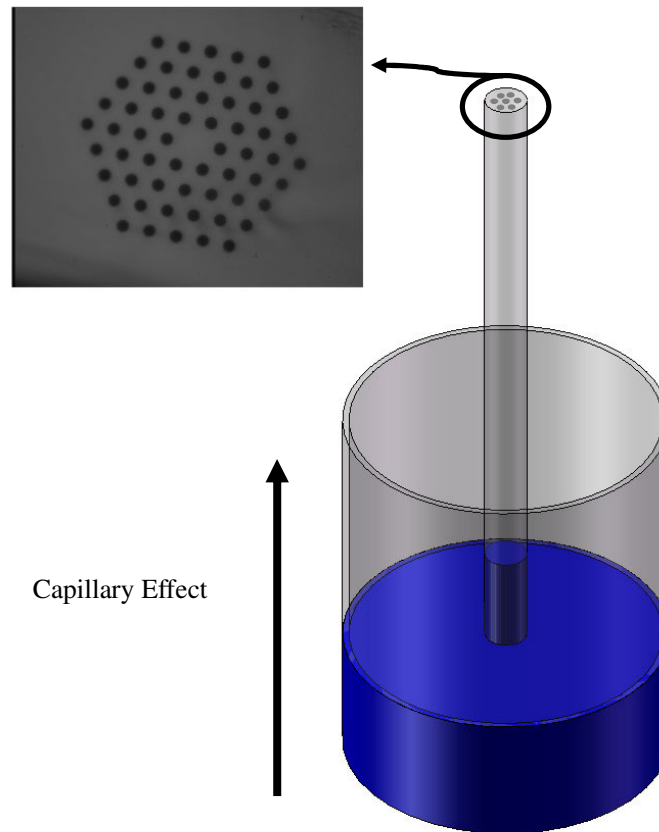


Fig 4.4 Liquid Crystal was infiltrated by capillary force.

Upon the application of electric field to the PLCF, the refractive index of E7 changes due to the reorientation of LC director axis. No matter which direction the electric field is applied to, it generally gives rise to the changes of refractive index in all three directions, owing to the close interactions between the neighboring molecules.

Before the application of the electric field by the high voltage power generator, the super-continuum light source was turned on and the corresponding transmission spectrum was recorded by the optical spectrum analyzer as a control data. There were four photonic bandgaps between the wavelength range of 600 nm to 1600 nm as shown in Fig 4.5. The first transmission band was about 400 nm wide, ranging from 1200 nm to 1600 nm.

Two experimental schemes were set up and tested. In the first setup, a flat metal plate was used. Fig. 4.5 shows the transmission spectrum of setup 1 under different voltage levels. It shows that with the increase of the applied voltage level, the transmission power drops. Before the application of any external voltage, the long axis of liquid crystals is deemed to orientate along the long axis of the PCF. At the beginning of electric field applied, there is not much change in the transmission bandgap. The liquid crystal molecule distortion that caused by the applied field do not induce appreciable change to the refractive indices. However, after increasing the applied voltage to 1000V, the

orientation of the molecules is dramatically altered by the applied electric field, inducing transmission power loss.

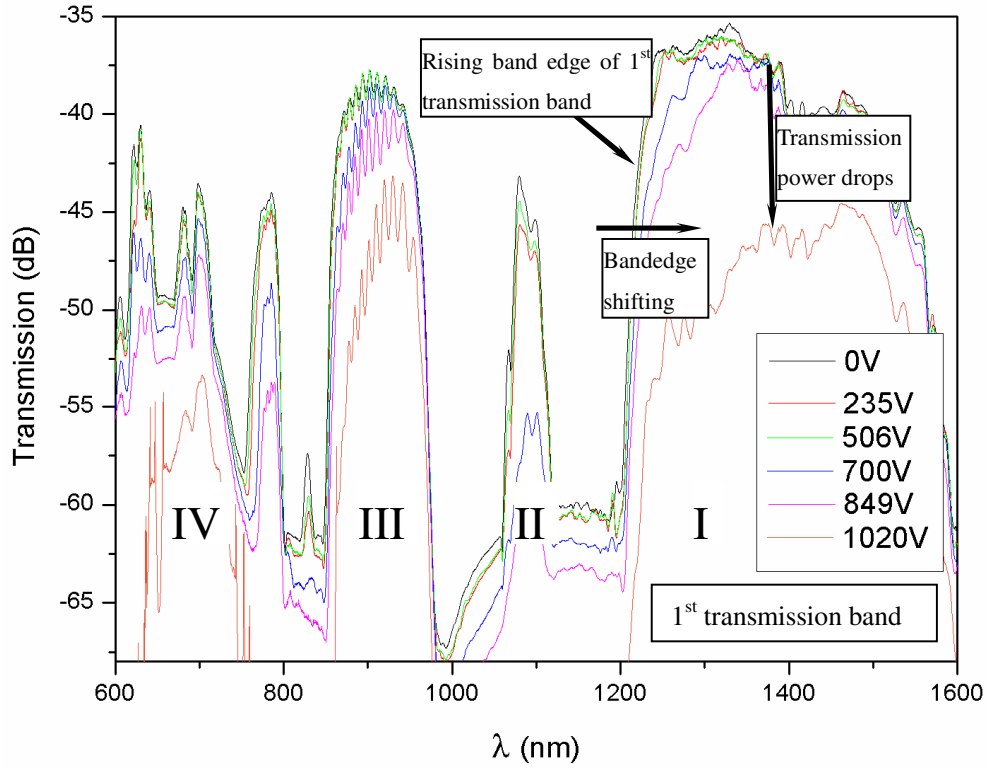


Fig 4.5 Transmission spectra of PLCF with different voltage levels

It could also be observed that the rising edge of the first transmission bandgap slightly shifts to longer wavelength in Fig 4.5. It is another indication that there are some changes of the refractive index in the PLCF as $n_e(\theta)$ changes its value when LC was experiencing director axis reorientation.

Refractive indices and dielectric constants are the two major physical parameters that characterize the electrical responses of liquid crystals to the external applied fields. The change of transmission spectrum is due to the refractive index changes in the PLCF under

the applied electric fields. The response of different materials depends on their dielectric anisotropy.

The dielectric constant ϵ is defined by the Maxwell equation[88]

$$\overline{D} = \overline{\epsilon} \cdot \overline{E} \quad (4.3)$$

where \overline{D} is the displacement current, \overline{E} is the electric field, and $\overline{\epsilon}$ is the tensor.

The material for the PCF is silica, which is an isotropic material. The dielectric tensor is expressed as

$$\epsilon_{si} = n_{si}^2 \times \begin{bmatrix} 1 & 0 & 0 \\ 0 & 1 & 0 \\ 0 & 0 & 1 \end{bmatrix} \quad (4.4)$$

On the other hand, the responses of liquid crystals are highly dependent on the direction and the frequencies of the electric field due to the molecular and energy level structures of nematic molecules. The dielectric tensor for uniaxial nematic LC is

$$\overline{\epsilon} = \begin{bmatrix} \epsilon_{\perp} & 0 & 0 \\ 0 & \epsilon_{\perp} & 0 \\ 0 & 0 & \epsilon_{\parallel} \end{bmatrix} \quad (4.5)$$

Thus the displacement current for two principle axis are

$$D_{\parallel} = \epsilon_{\parallel} E_{\parallel} \quad (4.6)$$

$$D_{\perp} = \epsilon_{\perp} E_{\perp} \quad (4.7)$$

For liquid crystal that we used in the experiment, E7 is positive uniaxial liquid crystals. Thus the director axis will tend to align along the applied electric field. As a result, the extraordinary wave of the input light travelling through the LC will experience phase shift if LC molecules reorientate.

The phase shifting of the transmission bandgap in setup 1 has been plotted in Fig 4.6. LC reorientation angle and the corresponding phase shifting has been simulated by using BeamPROP. Fig 4.6 shows the rising bandedge shifting under different applied voltage levels and the corresponding simulated LC orientated angle. The experimental result agrees well with the simulated result as shown in the figure.

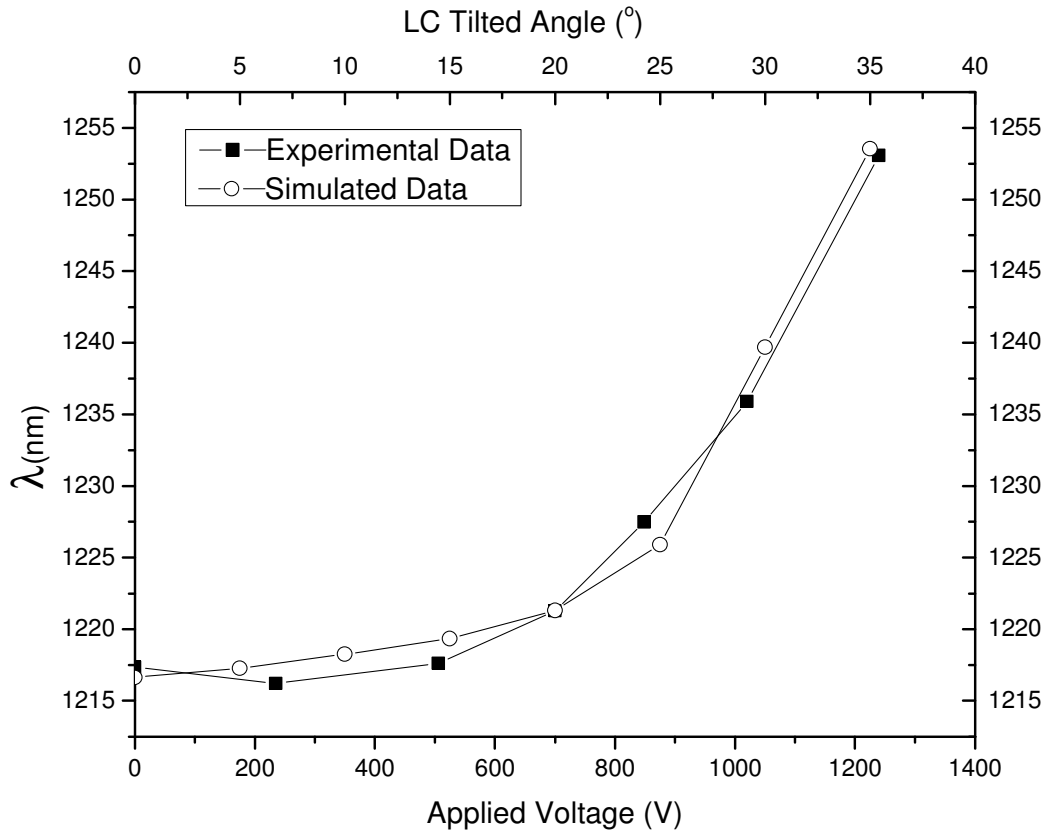


Fig 4.6 Rising Bandedge Shifting and simulated LC reorientated angles

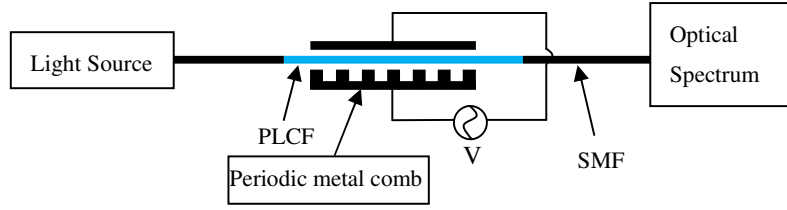


Fig 4.7 Experimental Setup

In Fig 4.5, it shows that the shifting of the transmission bandedge is not significant in the experimental setup 1. To have better observation on the effect of LC re-orientation and the effect on the refractive index changes, the PLCF was sandwiched between a periodically comb electrode plate in setup 2 as shown in Fig 4.7. The period of the periodic metal comb is $600\text{ }\mu\text{m}$.

When the liquid crystals are infiltrated into the PCF, the liquid crystals are arranged in a planar manner, such that its director axis is aligned along the fiber axis. The liquid crystal molecules stay planar aligned because of their elastic torque. When an electric field is applied over the PLCF, the liquid crystals in the electrode region will reorient towards the perpendicular direction of the fiber longitudinal axis. Thus the refractive index in this region is different with the region without electrode, generating a periodical refractive index modulation along the PLCF. This induces the LPG structure in the fiber. Fig 4.8 illustrates the formation of LPG structure.

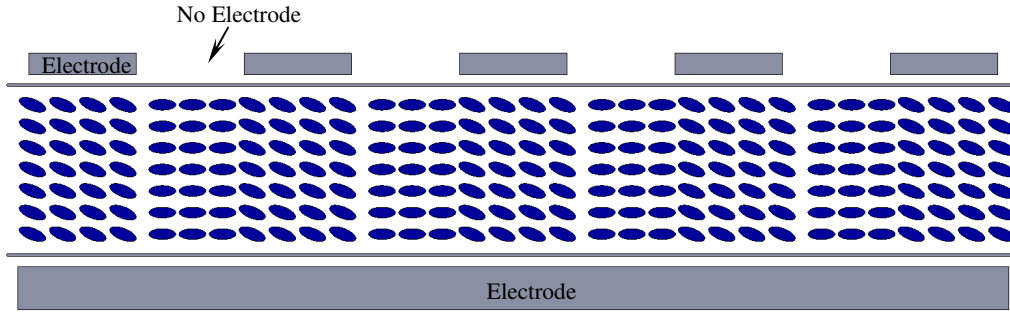


Fig 4.8 Formation of LPG structure

The index modulation causes the coupling of the core mode and the cladding mode along the PLCF, inducing the transmission dip in the first bandgap as shown in Fig 4.9.

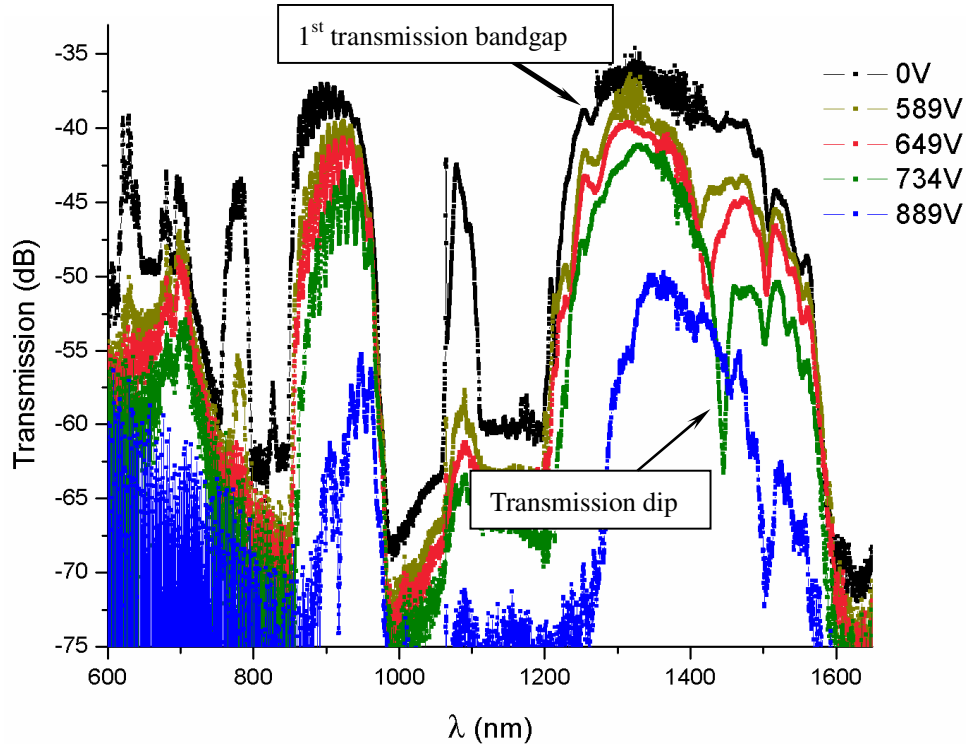


Fig 4.9 Transmission Spectrum of PLCF sandwiched between periodic electrodes

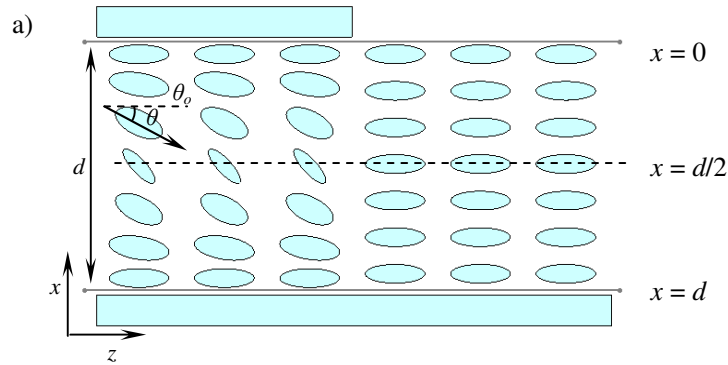
The resonance wavelength of the electric induced grating is given by

$$\lambda_{res} = \Lambda \left(n_{eff,h} - n_{eff,l} \right) \quad (4.8)$$

where Λ is the grating pitch, $n_{eff,h}$ is the effective index of the electrode region and $n_{eff,l}$ is the effective index of the region without electrode.

It has been proven experimentally that LC molecules tend to align themselves parallel to the PLCF longitudinal axis[89] after infiltration, that is $\theta = 0$ at the airhole surfaces. Upon external electric field application, the reorientation is governed by the basic physical principle that the director axis will tend to align the molecules in a new configuration so that the total free energy is minimum. However, the actual reorientation by the applied electric field is more complicated. Owing to the boundary conditions, the reorientation angle θ of the director axis vary as a function of the distance between the airhole surfaces under an applied field perpendicular to the PLCF. The maximum orientation angle will be at the center of the airholes. The reorientation profile can be approximated by a sinusoidal function[88].

$$\theta = \theta_0 \sin\left(\frac{\pi x}{d}\right) \quad (4.9)$$



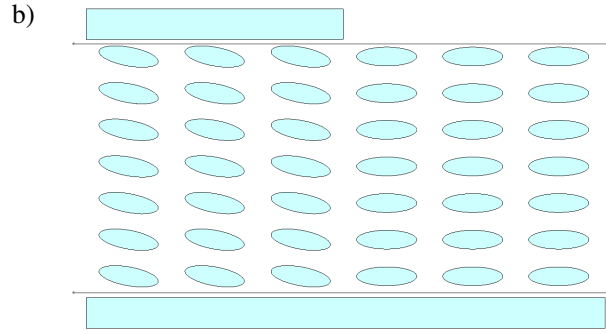


Fig 4.10 a) Individual LC director axis starts to reorientate if the first threshold meets, inducing twist profile of LCs.

b) Bulk LCs start to reorientate after the second threshold meets

From the reference of [88], it indicates that there are two thresholds corresponding to the significant changes in the reorientation, director reorientation angle θ and the bulk reorientation angle ϕ , respectively. When the applied voltage is just above a first threshold, the director axis will tilt along the applied electric field direction. But the original twist profile of the LC molecules are collectively preserved which means that the bulk reorientation angle ϕ remains unchanged. When the applied voltage increases to a higher value, the bulk reorientation angle starts to align with the direction angle θ shown in Fig 4.10, which in turn affects the effective index.

In the experiment, we assume that there is no cross-talk between the regions with and without electrode. So that $n_{eff,h} = n_e(\theta)$ and $n_{eff,l} = n_o$. And Eq(4.8) becomes

$$\lambda_{res} = \Lambda(n_e(\theta) - n_o) \quad (4.10)$$

Increasing the strength of the applied electric field causes the shifting of the resonance wavelength. And the light attenuation increases. This phenomenon is shown in Fig 4.9,

where the depth of the dip increased with the amount of voltage applied. In addition, shifting in the resonance wavelengths can also be observed, where the position of the loss dip shifts towards the longer wavelength (red-shift). The resonance wavelength is shifted from approximately 1450 nm to 1500 nm due to the changes of the cladding effective index. With the increase in electric field strength, the bulk LCs tend to tilt normal to the PLCF longitudinal direction. As θ becomes larger, the refractive index difference $(n_e(\theta) - n_o)$ between the two alternate regions along the PLCF increases. While the period Λ remains fixed, the value of the resonance wavelength in Eq(4.10) will increase as well. Thus when the director reorientation angle becomes larger, the transmission dip will shift to longer wavelength region. The change of effective index due to reorientation of the director axis follows Kerr effect, which means the refractive index changed is quadratic in the applied electric field [90]

$$(n_e(\theta) - n_o) = \lambda_o K E^2 \quad (4.11)$$

where λ_o is the optical wavelength, K is the Kerr constant and E is applied electric field.

By substituting Eq(4.11) into Eq(4.10), the new resonance wavelength due to the refractive index change becomes

$$\lambda_{res} = \Lambda \lambda_o K E^2 \quad (4.12)$$

By taking the derivative, the relationship between the shifting of the resonance wavelength and the applied voltage becomes clear. That is

$$\Delta\lambda_{res} = 2\Lambda\lambda_o KE\Delta E \quad (4.13)$$

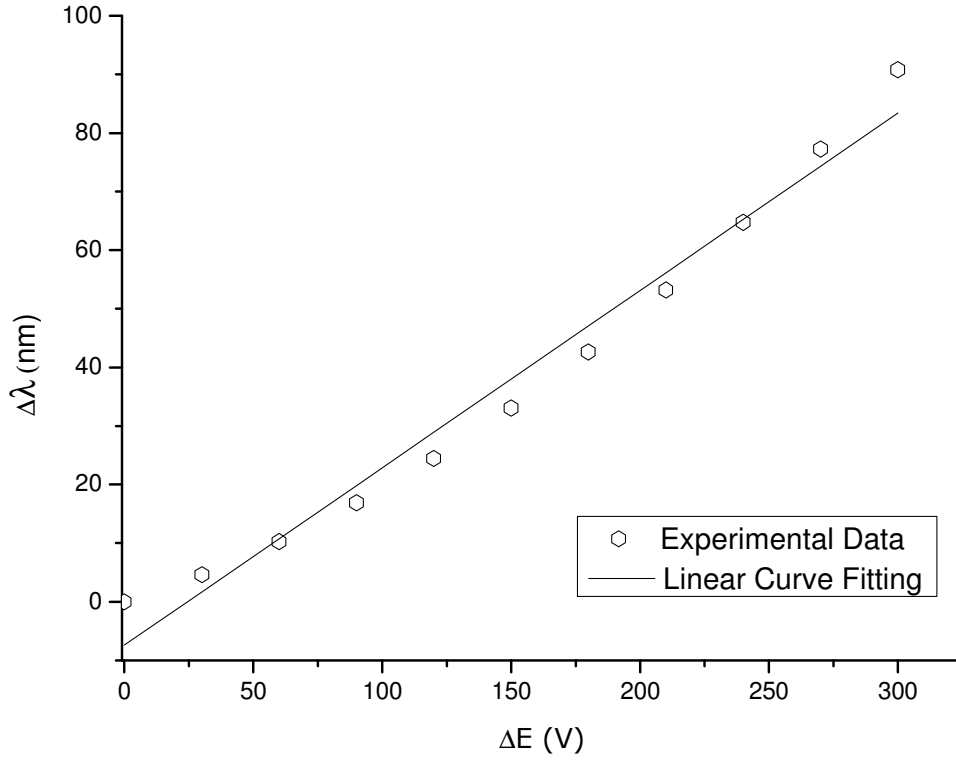


Fig 4.11 Shifting of the long period grating transmission dip with the increase of the applied voltage

Fig 4.11 shows the transmission dip response of the liquid crystal reorientation in the PLCF with respect to the applied voltage. It can be observed from the plot that the wavelength of transmission dip shifts to the red region when the applied voltage increases. Theoretically, the shifting of the resonance wavelength is in linear relationship with the change of the applied voltage. However, these experimental data is slightly offset from the linear curve fitting. This is because we assume that there is no cross-talk between the electrode and non-electrode region of the LPG structure. However, there is no clear cut of the director axis orientation at the boundary of the two alternate regions in

actual scenarios. Thus the relationship between the resonance wavelength and the change of applied voltage will not be as perfect linear fit as the theoretical prediction.

It could also be observed that the span of the resonance wavelength shifting is much larger than the rising bandedge shifting. This is because the transmission dip induced by the LPG structure is sensitive to the refractive index perturbation. Small changes of the refractive index difference will induce a significant shifting of the transmission dip. That is the main reason that LPG is popular and has been employed in different types of fiber optic sensors.

Apart from the shifting in the resonance wavelength, attenuation in the transmission intensity is also observed when the electric field strength is increased. This can also be accounted for the changes made to the effective index of the cladding modes, and the coupling of light to the cladding region of the fiber. The refractive index modulation along the PLCF gives rise to the bulk refractive index changes upon voltage applied as well. Furthermore, this form of attenuation was also noticed when the experiment was repeated. Nevertheless, in both experiments, there is no memory effect. Transmission spectra will return to their original positions when the electric field is switched off, making this a candidate for switchable devices that functions like an optical switch.

4.3 Effect of Temperature on Photonic Liquid Crystal Fiber⁵

In particular, liquid crystals have high birefringence (up to 0.5) and high dielectric anisotropy (up to $50\epsilon_0$) [29], thus allowing them to exhibit high-electro optic (as described in Section 4.2) and thermo-optic effects, which will be introduced in the following.

Nematic LCs, such as E7 that we used in our previous experiment, are known as a kind of thermotropic LCs. Due to the fluidity of the liquid crystal molecules, the increasing of temperature would induce rotation of the molecules. The corresponding refractive index changes is given by [91]

$$\Delta n_T = \frac{\partial n}{\partial T} T \quad (4.14)$$

The temperature change gives rise of spectral shift and liquid crystal phase transition from nematic to isotropic. Studies of the nematic LCs refractive indices show that the thermal index gradients ($\partial n_{\perp} / \partial T$ and $\partial n_{\parallel} / \partial T$) become very large near the phase transition temperature.

4.3.1 Experimental investigation

⁵ © 2012, IEEE. Reprinted, with permission, from Y.F. Zhang, C.C. Chan, M.X.A Chia and P. Zu, “Temperature Effect of Liquid Crystal in Photonic Bandgap Fiber-Based Sagnac Loop”, IEEE Sensors Journal, vol 12 (5), pp. 1609-1610, 2012.

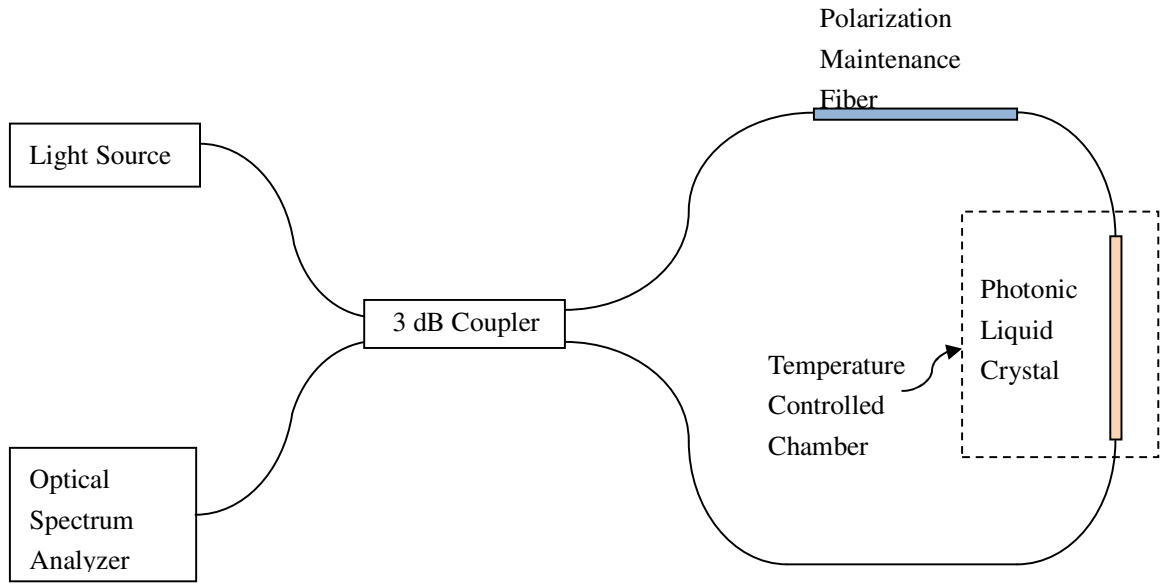


Fig 4.12 Schematic diagram of experimental setup

The schematic diagram is shown in Fig. 4.12. The PLCF was prepared using the same method as in Section 4.2. The two ends of PLCF were spliced with PMF and the coupler forming an optical fiber Sagnac loop. The splicing power was optimized to avoid overheating and PCF air hole collapse which would result LC leakage. The PLCF region was placed in a temperature controlled chamber after splicing.

The coupler in the Sagnac loop splits the input light from the light source into two beams, causing the two light beams to propagate in opposite directions in the loop. One light beam circulates in a clockwise direction while the other beam circulates in an anti-clockwise direction in the loop. The birefringence properties of the PLCF and PMF induce optical path difference of these two counter-propagating light beams. Eventually, the two light beams meet each other at the coupler again where interference occurs due to

the optical path difference. The corresponding interference spectrum can be observed at the optical spectrum analyzer.

The normalized interference spectrum of the Sagnac loop can be given by[92]

$$P = \frac{1 - \cos(\frac{2\pi BL}{\lambda})}{2} = \sin^2(\frac{\pi BL}{\lambda}) \quad (4.15)$$

where L and B are the total length and the birefringence of the PMF and PLCF. The changes of the ambient temperature around the PLCF affect the surface orientation of the LCs, which induces the changes of the PLCF birefringence. As a result, the output transmission interference spectrum will be changed. The change of the interference spectrum that induced by the birefringence change due to temperature effect can be written as [93]

$$P = \sin^2(\frac{\pi L}{\lambda}(\Delta n(T_0) + \frac{d\Delta n}{dT}(T - T_0))) \quad (4.16)$$

The wavelength spacing, D , between two adjacent transmission minima can be obtain by

$$D = \frac{\lambda^2}{BL} \quad (4.17)$$

The wavelength spacing is determined by the birefringence and the PMF and PLCF length in the Sagnac loop. For a fixed length of PLCF and PMF, the changes of the LC birefringence induced by temperature variation are of nonlinear relationship [88]. Thus the resulting wavelength shifting should be nonlinear as well.

The length of the PMF in this experiment was fixed at about 40 cm. Three different Sagnac loops with different PLCF lengths were prepared. The PLCFs were prepared separately by dipping the PCF in LC solution for about 30 minutes, 1 hour and 2 hours. The two ends of the PLCFs were then spliced with SMFs. The measured PLCF lengths after splicing were 1 mm, 8 mm and 66 mm. Since only the PLCF region was in the temperature controlled chamber, the changes of the optical fiber Sagnac loop output were mainly affected by the liquid crystal re-orientation due to temperature effect. And the phase difference between the two counter propagating light beams in the Sagnac loop was mainly affected by the change of the PLCF birefringence. The measured wavelength spacings between two adjacent minima for these samples are 17.52, 11.20 and 10.82 nm, respectively. It agreed well with Eq(4.17) that the longer of the PLCF, the narrower of the wavelength spacing of the Sagnac loop.

When the temperature in the chamber increases, a shifting of the interference pattern is observed. Shown in Fig.4.13 are the shiftings of the transmission spectra with 1 mm PLCF when temperature increases. It is observed that the transmission spectra shift towards longer wavelength when temperature increases. Usually when the temperature increases, the optical fields will have the transient responses of the molecules. These transient responses of LC molecules are usually manifested in the form of the momentarily molecules emission and absorption spectra shifts. Accordingly the effective molecular polarizabilities also translate into the refractive indices change.

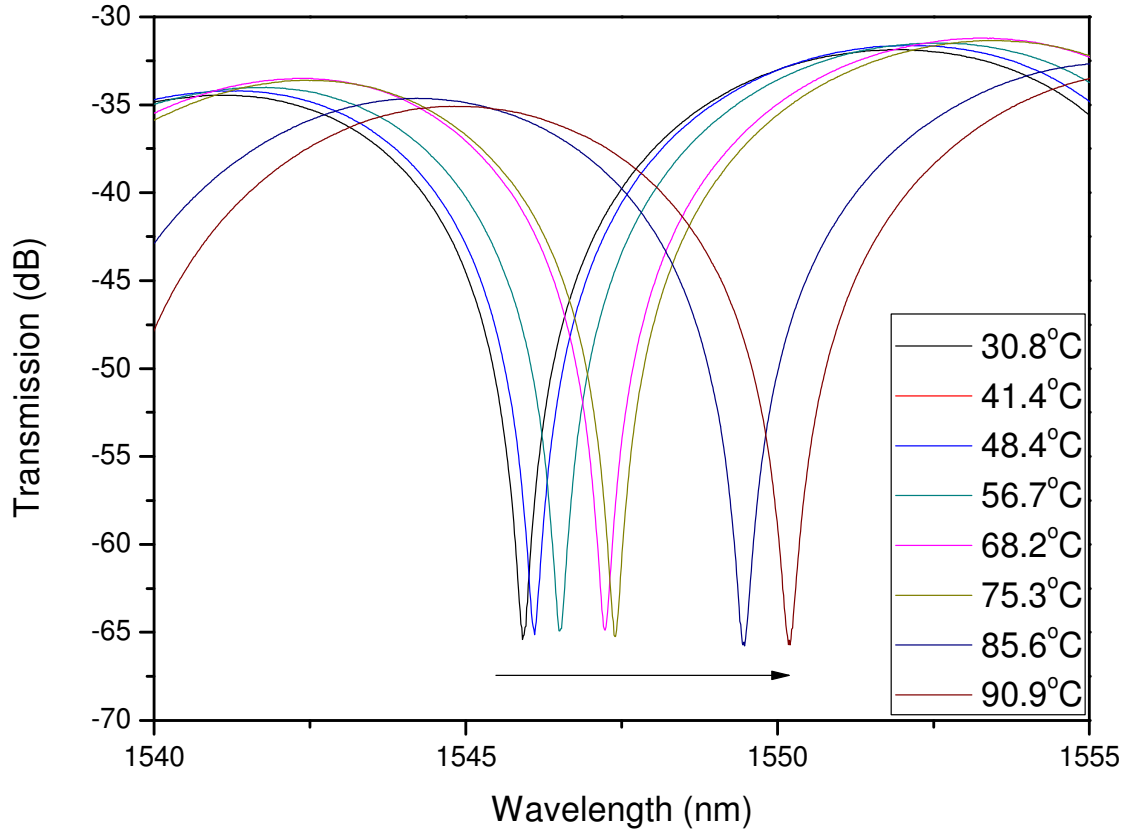


Fig 4.13 Transmission spectrum shifting for 1 mm PLCF

To understand liquid crystal physics under such circumstance, it will be more convenient to discuss in terms of the dielectric constants (ϵ_{\perp} and ϵ_{\parallel}), as the two principal refractive indices n_{\perp} and n_{\parallel} of a uniaxial liquid crystal and the anisotropy ($n_{\parallel} - n_{\perp}$) are related to the dielectric constants. ϵ_{\perp} and ϵ_{\parallel} can be obtained from

$$\epsilon_{\parallel} = \epsilon_l + \frac{2}{3}\Delta\epsilon \quad (4.18)$$

$$\epsilon_{\perp} = \epsilon_l - \frac{1}{3}\Delta\epsilon \quad (4.19)$$

where $\epsilon_l \sim 1 + C_1\rho$ and $\Delta\epsilon \sim C_2\rho S$. That is the temperature dependence of the dielectric constants and the corresponding changes of refractive indices is due to the

density ρ dependences, the order parameter S of the liquid crystal at that temperature, and C_1 and C_2 are constants.

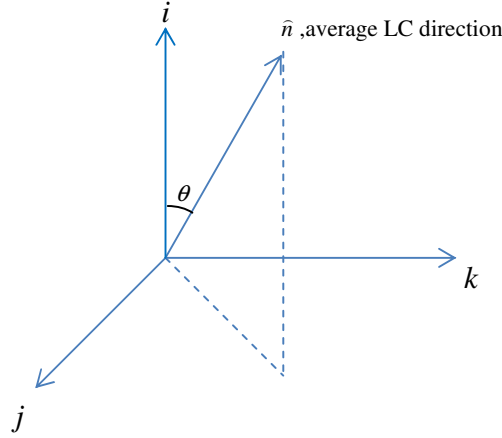


Fig 4.14 Coordinate system of microscopic order parameter of a nematic liquid crystal molecule

The order parameter S is defined by

$$S = \frac{1}{2} \langle 3 \cos^2 \theta - 1 \rangle \quad (4.20)$$

It is an average value over the whole system to define the LC phase, where θ is the average bulk LC direction shown in Fig 4.14. For a perfectly aligned liquid crystal, $\langle \cos^2 \theta \rangle = 1$ and $S = 1$; However, if in a perfectly random system, $\langle \cos^2 \theta \rangle = \frac{1}{3}$ and $S = 0$.

Generally the S value for a typical LC sample range from 0.3 to 0.8. However, there will be decreasing of S value when the temperature increase. It will experience a rapid drop to 0 when LCs undergo a phase transition from mesophase to isotropic phase. It could be observed from Fig 4.13 that there is a rapid shift of the transmission dips from 75.3°C to 85.6°C. With the increase of temperature, the wavelength shifting is observed in a

nonlinear relationship with the temperature. This is because LCs are in a completely random and isotropic phase when $S = 0$.

Total shift of 4.68 nm and 6.44 nm were achieved for 8 mm and 66 mm PLCF for about 40°C increment of temperature (from 26°C to 66°C). It shows that with PLCF length becomes shorter, the degree of transmission dip shifting decreases as shown in Fig. 4.15.

In order to have more shifting of the transmission spectrum when same degree of temperature increases, the longer of the PLCF is recommended. However, increase of LC infiltration length in PCF will result the increment of power loss. To avoid this certain loss, it is recommended to keep the PLCF length less than 70 mm.

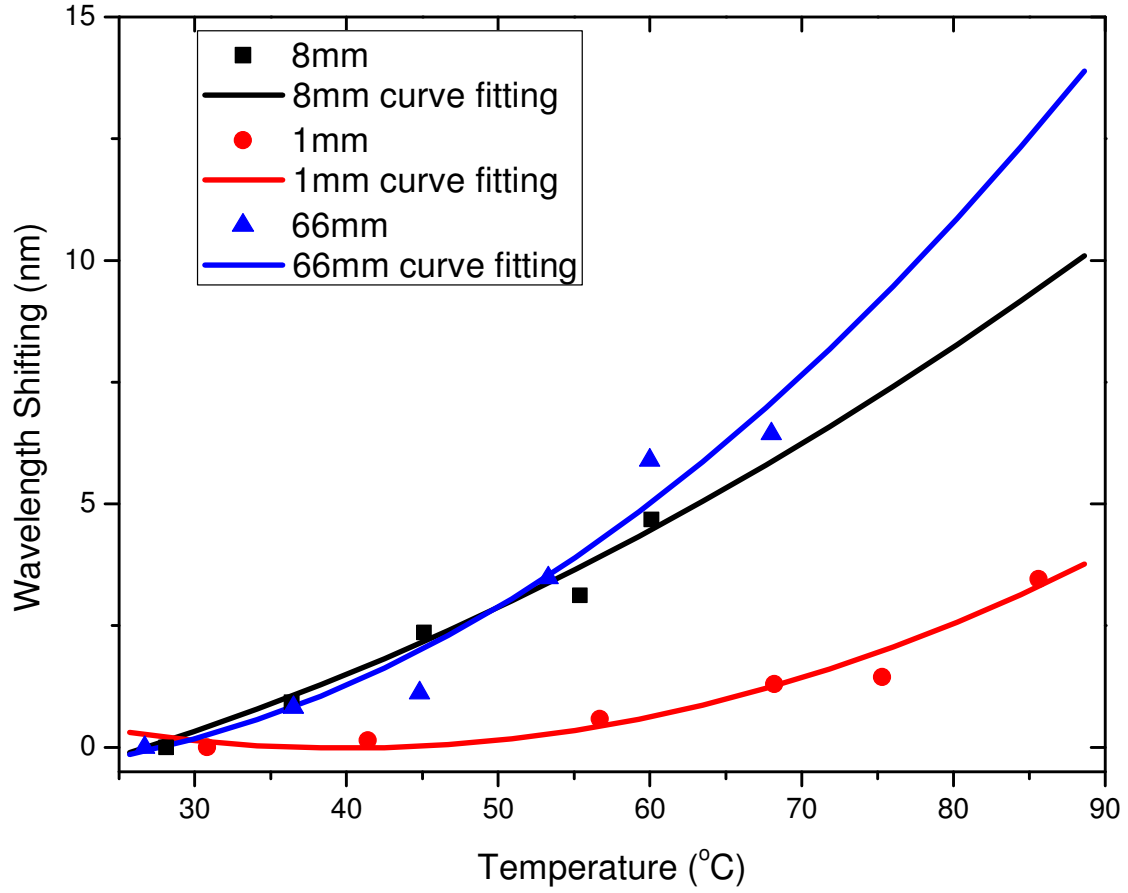


Fig 4.15 Degree of transmission dip shifting for different PLCF lengths

In general, the main feature to distinguish liquid crystals from other samples is that the physical properties of LCs are dependent on the orientation of the director axis. In most situations, LC director axis reorientation upon increasing of temperature often accompanies fluid flows, which these processes are necessarily coupled, and vice versa. When the flow is in the steady state, a stable director axis orientation is induced by the flow with an angle θ_{flow} determined by the viscosity of the LCs.

4.4 Chapter Summary

In summary, increasing the voltage across the PLCF in the presence of a periodically comb metal plate has formed LPG structure in the fiber, which results grating dips in the spectrum. When the strength of the electric field is increased, the position of the dip shifted towards the longer wavelength. In other words, the resonance wavelength has red-shifted. Furthermore, there is substantial loss in light intensity as the voltage across the PLCF increases. This behavior observed is resulted from the orientation of the liquid crystals in the PLCF perpendicular to the light transmission direction.

The increase of ambient temperature will also cause the change of the refractive index of liquid crystals due to the fluidity nature of the material, which in turn change the effective index of the PLCF region. Sagnac loop was setup to observe the effect of refractive index changes. It was observed that the interference was having red-shift after temperature increase. And there was big transmission loss observed near the LC phase transition temperature.

The LC orientation not only can be affected by changing of temperature and applying electrical field. It can be affected optically as well. The experimental demonstration and detailed discussion will be carried out in Chapter 5.

Chapter 5

Investigation of the Photonic Liquid Crystal Fiber Optical Modulation

5.1 Introduction

Photonic crystal fiber provides more opportunities for various applications compared to traditional optical fibers. In Chapter 4, we understand that by filling of liquid crystal into photonic crystal fibers, external changes of temperature or electrical voltage will change the birefringence of liquid crystals thus inducing transmission spectrum shifts. It makes PLCF a candidate for temperature measurement or other applications related to electrical voltage. Other than parameter measurements which have been demonstrated in Chapter 3 and chapter 4, there are other properties of PLCF which make it competent as optical filter.

As described in Chapter 4, birefringence is a unique property of LC because the molecules are elongated in shape and in ordered orientation. The birefringence, Δn , is a continuous function of wavelength with the application of some external fields [94]. Thus one of the main applications of infiltrating LCs into the cladding air holes of PCF is to manipulate the molecular orientation of LCs in the fiber as the large and controllable

birefringence of LC gives PLCFs their tunability.

However, it is inherently difficult to manoeuvre the LC which is located in the micron sized air holes within the cladding. Moreover, the initial alignment of LC molecules is dependent on the surface boundary conditions, where the LC molecules will arrange in a specific orientation such that the free energy is minimized[95]. Typically, the LC molecules are aligned mainly along the direction of the optical fiber[96]. But this alignment is not highly ordered as the aligning force is only provided by the capillary surface of the fiber[88].

In Chapter 4, we have demonstrated that the birefringence of LCs can be easily modulated by temperature or electric field. In this chapter, optical modulation of LC molecules will be investigated.

Studies by other groups have shown that doping LC with certain azo dyes can improve the order of LC in PCF [103-105]. This is because azo dye molecules generate anchoring force and the cylindrical air holes surface provides planar anchoring forces. Under the effect of the combined anchoring forces, a uniform and highly ordered LC orientation will be formed [89]. In this chapter, a noncontact photoalignment method is employed in this study. The nematic LC solution is doped with certain azo dye. And the modulation of LC alignment is attained by the application of an external optical field, which is facilitated by azo dyes.

5.2 Liquid Crystal Orientation Realized by Applied Laser Power

5.2.1 Introduction

Generally by applying an optical field, the electronic structure, density and molecular orientation of LCs can be easily perturbed if the optical Freedericksz threshold is met after exposed to laser [97]. When the applied optical field is the polarized light, the LC molecules will be realigned if they are in nematic phase. If they are in isotropic phase, they will be aligned into an order manner. The perturbation can induce bulk refractive index changes.

First reported in 1990, it is found that by adding small amounts of anthraquinone dye in liquid crystal, the corresponding optical Freedericksz threshold will be reduced by more than two folds, which is 50 W/cm^2 instead of normally observed few kW/cm^2 [98]. Generally, by carefully adjusting the dissolved concentrations and selecting different types of dyes, the doping of LCs will result in modifications of both their linear and non-linear optical properties. A prominent effect is that the dissolved dye will increase the LCs absorption at some particular wavelength region.

In Chapter 2, the azo dye molecule structure has been described as elongated in shape, which is similar to LCs. However, the dye molecules have an extended conjugated system that strongly absorb visible light, which in turn to change or affect the orientation

of the host liquid crystal if the dye molecules themselves experience some physical or orientational changes after photon absorption. Since the azo dye inside the liquid crystal of PLCF reduces the Freedericksz threshold of the laser-induced reorientation, the amount of time to achieve Freedericksz transition should be different for different exposure intensities.

5.2.2 Experimental investigation

To determine the optimum exposure intensity to be used for further investigation, the PLCF samples were exposed under different laser power for more than 10 minutes. The transmission spectrum was recorded for analysis. A Sagnac loop configuration was used. As described in Chapter 4, Sagnac loop is sensitive to the LC reorientation as it affects the polarization of the PLCF. The schematic diagram is shown in Fig 5.1. It consisted of a 3dB coupler, a section of polarization maintaining fiber (PMF) and a short length of photonic liquid crystal fiber (PLCF) which was prepared by infiltrating dye-doped LC in PCF (LMA-10, NKT). The dye-doped liquid crystal was prepared by mixing the liquid crystal (E7, Merck) and azo dye (Methyl Red, MR, Aldrich) homogenously at the ratio of 99.3 : 0.7 wt% in ultrasonic machine.

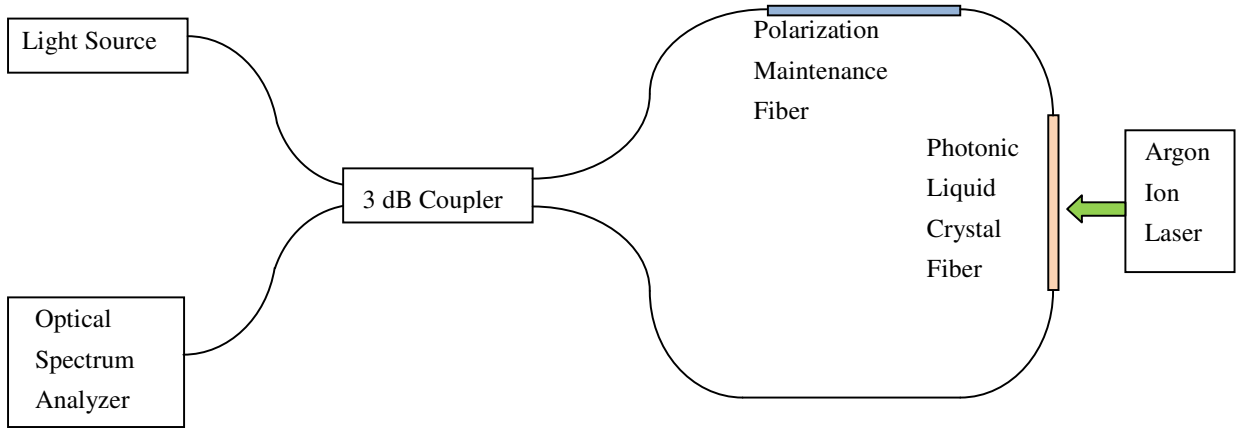


Fig 5.1 Experimental Setup for measuring the optical tuning properties of PLCF in a Sagnac loop

The 3dB coupler splits the light from light source equally into two counter propagating waves. The birefringence of the PMF and the anisotropy of LC in the PLCF induce optical path difference between the two orthogonally polarized waves. This causes interference when the two counter propagating waves meet in the coupler again and results in the interference spectrum[99]. Consequently, the normalized output transmission can be obtained which is described by the following

$$T = \frac{1}{2}(1 - \cos \phi) \quad (5.1)$$

where ϕ represents the phase difference between the two counter propagating waves, which can be further described by

$$\phi = \frac{2\pi LB}{\lambda} \quad (5.2)$$

and the wavelength spacing, D (which is the wavelength range between two adjacent output minima) of the sinusoidal transmission spectrum is given by

$$D = \frac{\lambda^2}{BL} \quad (5.3)$$

where λ is the operation wavelength, which is 1550 nm in our experiment. $LB = L_{PM}B_{PM} + L_{LC}B_{LC}$, where B_{PM} is a constant that introduced by the PMF, L_{PM} is the length of PMF inserted into the Sagnac loop. L_{LC} and B_{LC} are the length and the birefringence of the PLCF, respectively. The length of PLCF and PMF are controlled at about 30 mm and 49 cm in the experiment to adjust the interference band in the range of 1535 nm to 1560 nm. B_{LC} is the birefringence of the methyl-red-doped liquid crystal E7, which equals to $(n_e(\theta) - n_o)$.

When in the absence of Ar^+ laser light, liquid crystal molecules in the PLCF tend to align themselves along the fiber axis. The individual alignment is subjected to the surface boundary conditions [100, 101]. As illustrated in Fig 5.2, upon application of the laser, MR molecules absorb the laser light. Upon photoexcitation, the dye molecules will exhibit *trans-cis* isomerism (shown in Fig. 5.3). The azo molecules are in the *trans* form when they are in ground state. They will transform into *cis* form when they are in excited state. The excited dye molecules in turn exert an intermolecular torque on the LC molecules. The intermolecular torque can be stronger than the optical torque [102]. Upon meeting the Freedericksz transition field strength condition, LC molecules, which still in the nematic phase, reorientate their director axis to a new configuration through the dipolar interaction with MR molecules in order to minimize the free energy in the total system.

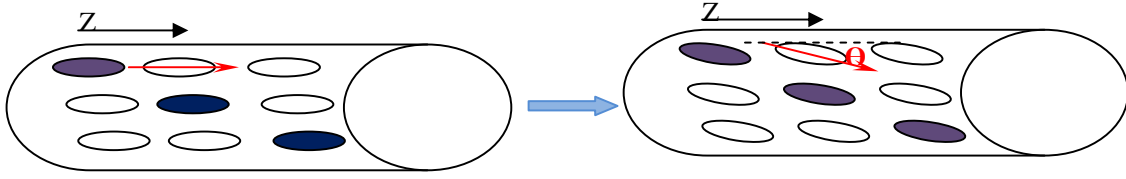


Fig 5.2 Liquid crystals will be photo-aligned by azo dye (Methyl Red, MR) under the irradiation of Argon ion laser

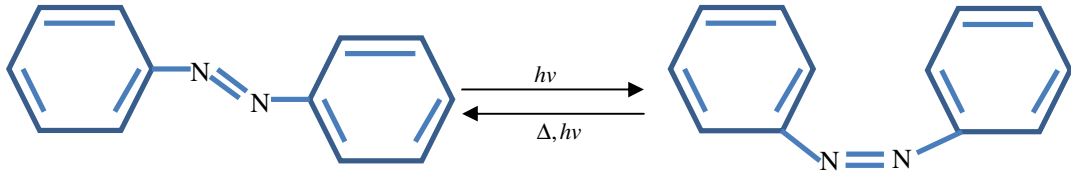


Fig 5.3 Molecular structural changes associated with trans-cis isomerization

The torque balance equation after the minimization of the total free energy is [98]

$$K_1 \frac{d^2\theta}{dy^2} + \frac{\Delta\epsilon \langle E_{op}^2 \rangle}{8\pi} \sin 2(\beta + \theta) = 0 \quad (5.4)$$

where θ is the reorientation angle, E_{op} is the optical field, $\langle E_{op}^2 \rangle = \frac{|E|^2}{2}$, K_1 is the Frank elastic constant. And $(\beta + \theta)$ is the angle between the laser propagation vector and the perturbed director axis as shown in Fig 5.4.

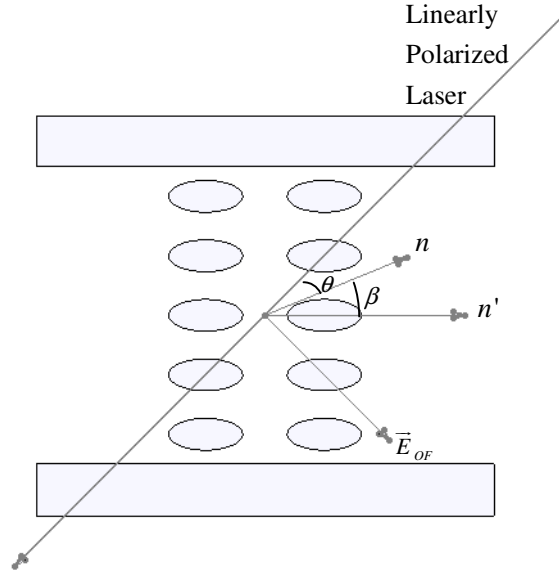


Fig 5.4 LC reorientation under the irradiation of linearly polarized laser beam, \vec{E}_{OF} is optical field, β is the original angle between LC director axis and optical field, θ is the reorientation angle

Due to the large birefringence of nematic LCs, a small change of the director axis orientation will give rise to sufficiently large refractive index change to generate appreciable optical effects. If θ is small, Eq(5.4) can be written as

$$\left[\frac{8\pi K_1}{\Delta\epsilon \langle E_{op}^2 \rangle} \right] \frac{d^2\theta}{dy^2} + (2\cos 2\beta)\theta + \sin 2\beta = 0 \quad (5.5)$$

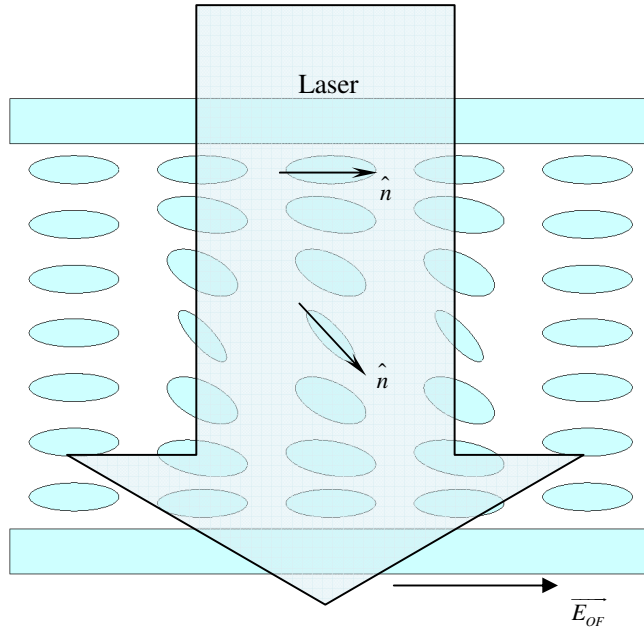


Fig 5.5 LC director axis reorientation profile inside the PLCF air holes

Usually the reorientation is small at the boundary and maximum at the center as shown in

Fig 5.5, thus the reorientation angle along transverse direction of PLCF is

$$\theta = \frac{\left[\Delta \epsilon \langle E_{op}^2 \rangle \right]}{16\pi K_1} \sin 2\beta (dy - y^2) \quad (5.6)$$

As a result, the refractive index change that the incident laser will experience is

$$\Delta n = n_e(\beta + \theta) - n_e(\beta) \quad (5.7)$$

where $n_e(\beta + \theta)$ is given by[88]

$$n_e(\beta + \theta) = \frac{n_e n_o}{\sqrt{[n_e^2 \cos^2(\beta + \theta) + n_o^2 \sin^2(\beta + \theta)]}} \quad (5.8)$$

where n_e and n_o with values of 1.7017 and 1.5055 respectively are the extraordinary and ordinary refractive indices of E7. For small θ , the change in the refractive index Δn can

be expressed as

$$\Delta n = n_2(z) \langle E_{op}^2 \rangle \quad (5.9)$$

which is proportional to the square modulus of the optical electric field.

Therefore, when the order parameter of LCs is modified by MR *trans-cis* isomerization, a change in the birefringence occurred. The new alignment of the LC molecules changes the PLCF air holes effective index owing to the birefringence properties. Thus the optically modulated birefringence will result in a change of both the transmission spacing and minima wavelength of the interference fringes. As a result, an obvious phase shifting of the transmission dips occurs as shown in Fig 5.6.

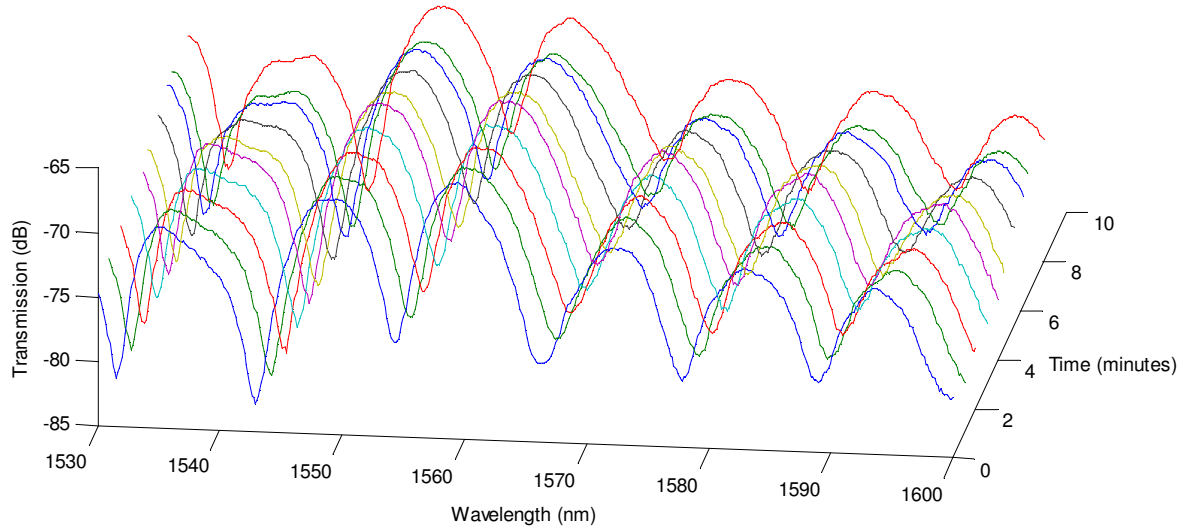


Fig 5.6 Shifting of the interference spectrum versus the irradiation time of the PLCF under Argon ion laser.

The speed of the transmission minima shifting is slow initially, and then a fast shifting speed starts at about 4 minutes after irradiation as shown in Fig 5.7. After 8 minutes,

another fast phase shifting is observed. This can be explained by the two competing forces aligning the LC molecules in the PLCF. Before the green laser light beam irradiation, the planar anchoring force provided by the capillary boundary of PLCF is the only force aligning the LC molecules. This force aligns the LC molecules with their director mainly pointing in a direction parallel to the capillary tube axis [103]. However, another aligning force arises when dye-doped PLCF is excited by the laser beam. This force is the anchoring force exerted by the adsorbed dye molecules. The force aligns the LC molecules with their director axis perpendicular to the laser beam polarization direction[104]. Since the aligning directions of these two forces are different, they compete with each other in aligning the LC molecules. In the initial stages of the experiment, the planar anchoring force dominates over the dye-induced anchoring force. It resists any changes to the initial planar alignment of the LCs as shown in Fig 5.8. This explains the slow variations of the interference spectrum. Once the planar anchoring force is overcome, the reorientation of LC molecules becomes easier. Thus the phase shifting of the spectrum speeds up[105]. Studies have shown that under prolonged exposure [106], the alignment of the dye-doped LC molecules will be perpendicular to the optical field.

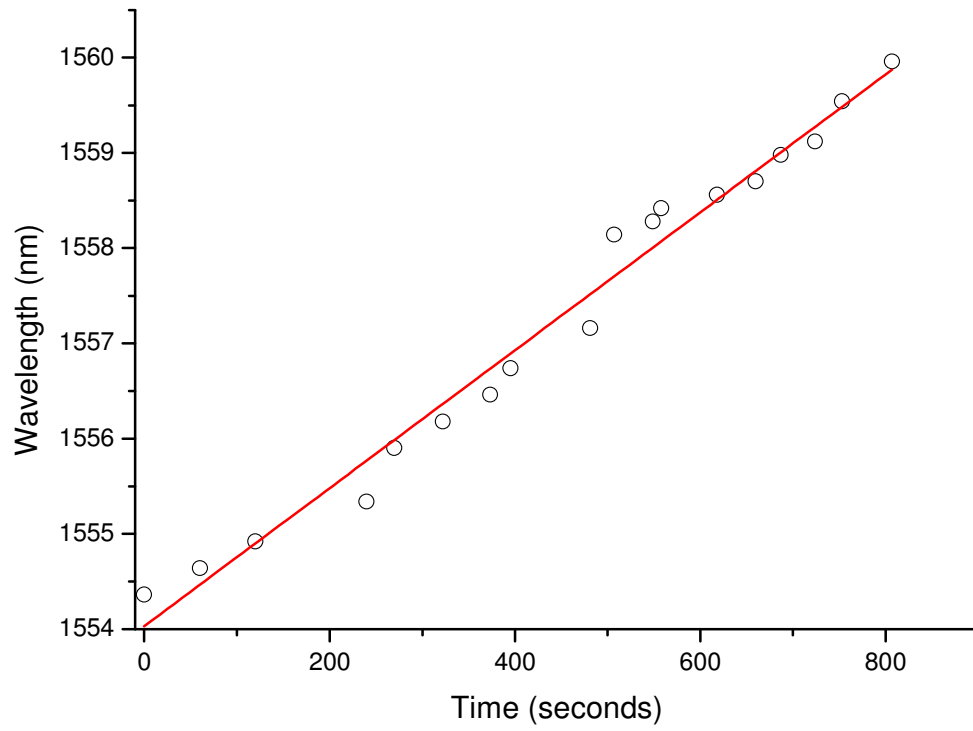


Fig 5.7 Wavelength shifting VS irradiation time of the PLCF under Argon ion laser

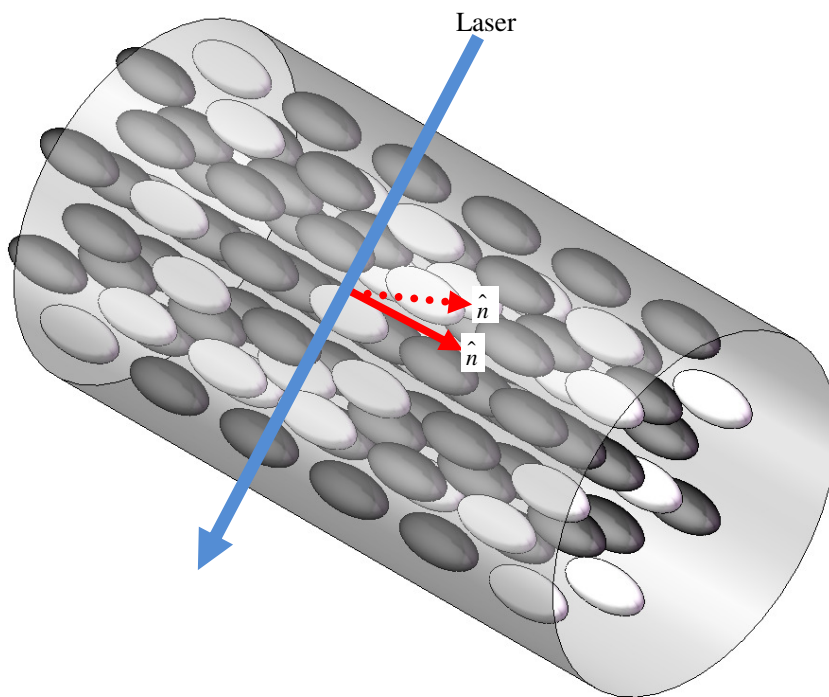


Fig 5.8 Propagation direction of optical field in planar aligned dye-doped LC

To study the exposure intensity effect on the transmission minima shifting, the PLCF was irradiated in Argon ion laser with exposure intensity of 20 mW/cm² and 200 mW/cm². When the exposure intensity was 20 mW/cm², the interference fringe underwent red shifting after irradiation under the laser for about 60 seconds. When the exposure intensity was increased to 200 mW/cm², the shifting took place in much faster way than the lower intensity shown in Fig 5.9. The transmission spectrum started to red-shift within 10 seconds after irradiation.

It is reported that the director motion generated by the external and elastic torques is linearly superposed of the external optical field generated torque, the elastic deformation torque and the dye-induced torque. The equation of the director motion can be written as[88]

$$\gamma_1 \omega_n = \Gamma^{ext} + \Gamma^{elast} \quad (5.10)$$

where γ_1 is the rotational viscosity of the nematic liquid crystal, ω_n is the director angular velocity, Γ^{ext} is the external torque and Γ^{elast} is the elastic torque.

If the liquid crystal is doped with azo dye, the equation of the director motion becomes

$$\gamma_1 \omega_n = \Gamma^{ext} + \Gamma^{elast} + \Gamma^{dye} \quad (5.11)$$

It is deemed that the dye molecules are excited by the external optical field. The optical field induces internal angular momentum on the dye molecules. The energy is continuously transferred by collisions to the host liquid crystal molecules. If the total strength is greater than the Freedericksz threshold, the reorientation occurs. The present of azo dye in liquid crystal mixture reduce the Freedericksz threshold. For higher

exposure intensity, the greater value of $(\Gamma^{ext} + \Gamma^{dye})$, the faster the Freedericksz threshold condition meets.

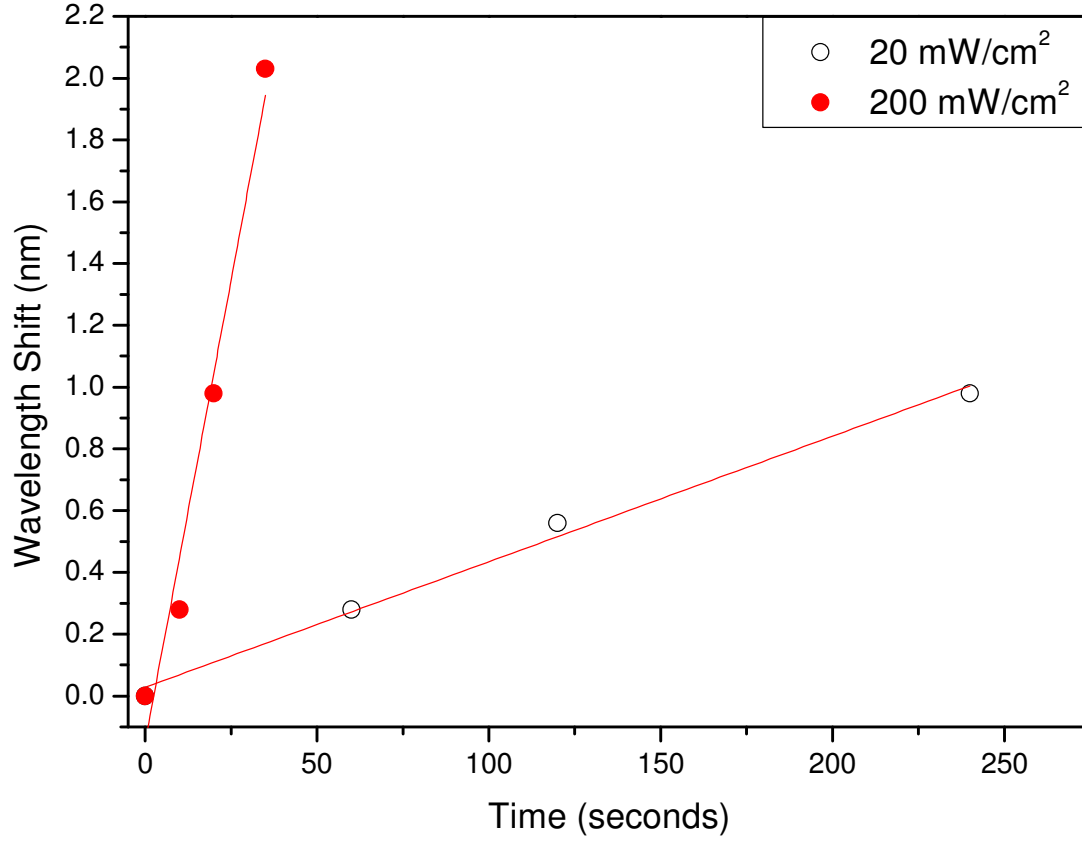


Fig 5.9 Speed and span of wavelength shiftings for different irradiation power

In particular, methyl-red-doped nematic liquid crystals are observed to have high nonlinear index as large as $6 \text{ cm}^2/\text{W}$. Furthermore, it can be enhanced by applying low-frequency AC electric field. However, a high-frequency electric field will quench the reorientational effects [102]. Under suitable surface treatment conditions, the photo-reorientational effects can be made permanent (but erasable).

5.3 Liquid Crystal Reorientation Realized by Exposure Time

While increase of exposure intensity induces faster Freedericksz transition, the optical field induced director axis reorientation is accompanied by fluid flow, inducing more complicated change of liquid crystal reorientation and change of refractive index.

Usually, the azo dye molecules have the tendency to be adsorbed onto the substrate surface under proper irradiation of blue-green light [104]. The adsorbed azo dye molecules then reorientate the LC molecules. As introduced in Section 5.2, the refractive index of liquid crystal is strongly influenced by its molecular orientation. The refractive index changes of the liquid crystals under laser beam irradiation for certain period of time are investigated in this section.

5.3.1 Experimental investigation

A broadband light source (1520 nm – 1620 nm) was used. The transmission spectra were recorded by an optical spectrum analyser (OSA, YOKOGAWA AQ6370). According to Eq (5.3), the wavelength spacing of the Sagnac interferometer can be tuned by adjusting the length of the PMF. For a 49 cm of PMF used, the spacing was about 11.48 nm. The corresponding extinction ratio of the interferometer was 12.63 dB. The PLCF region of the interferometer was irradiated with a linearly polarized CW laser from an Argon ion laser. The laser wavelength, 514 nm was within the absorption band of the Methyl Red azo dye. To have better observation of the phase shifting, the exposure intensity was set at

20 mW/cm².

The PLCF was prepared using a large mode area photonic crystal fiber (PCF) (LMA-10) from Crystal Fibre A/S. The PCF which is made of pure silica comprises four rings of hexagonally distributed cladding holes. The diameter of the solid core is 10 μm and the cladding diameter is 125 μm . The liquid crystal and azo dye were E7 ($n_e=1.7472$ and $n_o=1.5217$ at 20°C) from Merck and Methyl Red (MR) from Aldrich. 99.0 wt% of and 1.0 wt% of Methyl Red were blended at 65°C (higher than the transition temperature of E7) to form a homogeneous mixture. Empty PCF with both ends cleaved was dipped into the prepared liquid crystal mixture for about 20 minutes. The mixture was infiltrated into the airholes of PCF by capillary effect. The length of infiltration was controlled at about 20 mm to 30 mm. Owing to the higher refractive index of LC comparing to pure silica, the light in the PLCF was no longer guided by total internal reflection. Instead, light was confined in the fiber by photonic bandgap effect.

After the infiltration, both ends of the fiber were spliced into the Sagnac loop. The MR-doped PLCF was placed on a station. The collimated Ar⁺ laser light was projected on PLCF region. The laser light irradiated the MR in the PLCF, changing the orientation of the MR. The wavelength of the Ar⁺ laser was 514.5 nm. It is within the absorption band of the MR. The exposure intensity was 20 mW/cm². The transmission spectra for different exposure time were recorded by an optical spectrum analyzer.

All the physical properties of the LCs are influenced by the inter- and intra-molecular fields owing to molecular structures changes. Molecular structures therefore are expected

to influence the LCs reorientation under the optical field in both their magnitude and response time. LCs reorientation under different optical power has been investigated in Section 5.2. In this section, LCs reorientation behavior for long exposure time will be investigated.

The transmission spectra of the Sagnac loop were recorded before the Ar^+ laser was turned on. The interference spectra were fallen into the transmission bandgap of the PLCF, which is within 1200 nm to 1600 nm. The extinction ratio of 16.18 dB was observed in the transmission dip near 1545 nm. To investigate the optical tuning properties of the Sagnac interference spectra and the effect of the irradiation duration, the MR-doped PLCF was irradiated under Ar^+ laser light for more than 50 minutes. The transmission dips did not show any significant changes for the first minute. After one minute of irradiation, the MR molecules started to change from *trans*-form to *cis*-form. The *trans-cis* isomerization generates torque effect which changes the LC orientation perpendicularly to the polarization of the writing beam, leading to the change of the PLCF birefringence. Thus the effective birefringence B_{eff} of the Sagnac loop changed. The transmission spectra started to shift.

The spectra were observed red-shifting in the beginning. The transmission dip at 1554.34 nm shifted to 1560.12 nm after 17.59 minutes as shown in Fig. 5.10. A total of 5.78 nm red shifting was achieved, which has covered 52% of the wavelength spacing (about 11 nm).

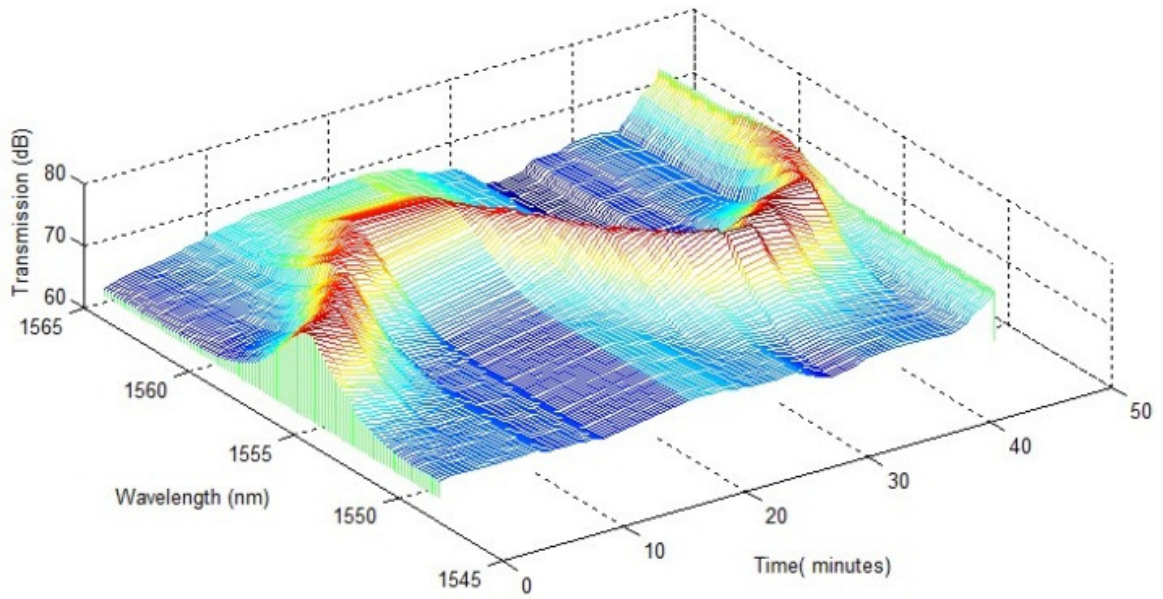


Fig 5.10 Transmission power, wavelength shifting vs. time

After having exposed for more than 18 minutes, the spectra started to blue-shift. It was reported that ripple structure will be formed after long period of irradiation[107]. The ripple structures run parallel to the pump field. When the amplitude is large enough, the structure will re-orientate LC molecules with their structure, inducing reverse shifting of the transmission spectra[108]. This property makes both red-shift and blue-shift optical tuning in one setup possible by controlling the irradiation duration without additional experimental modification.

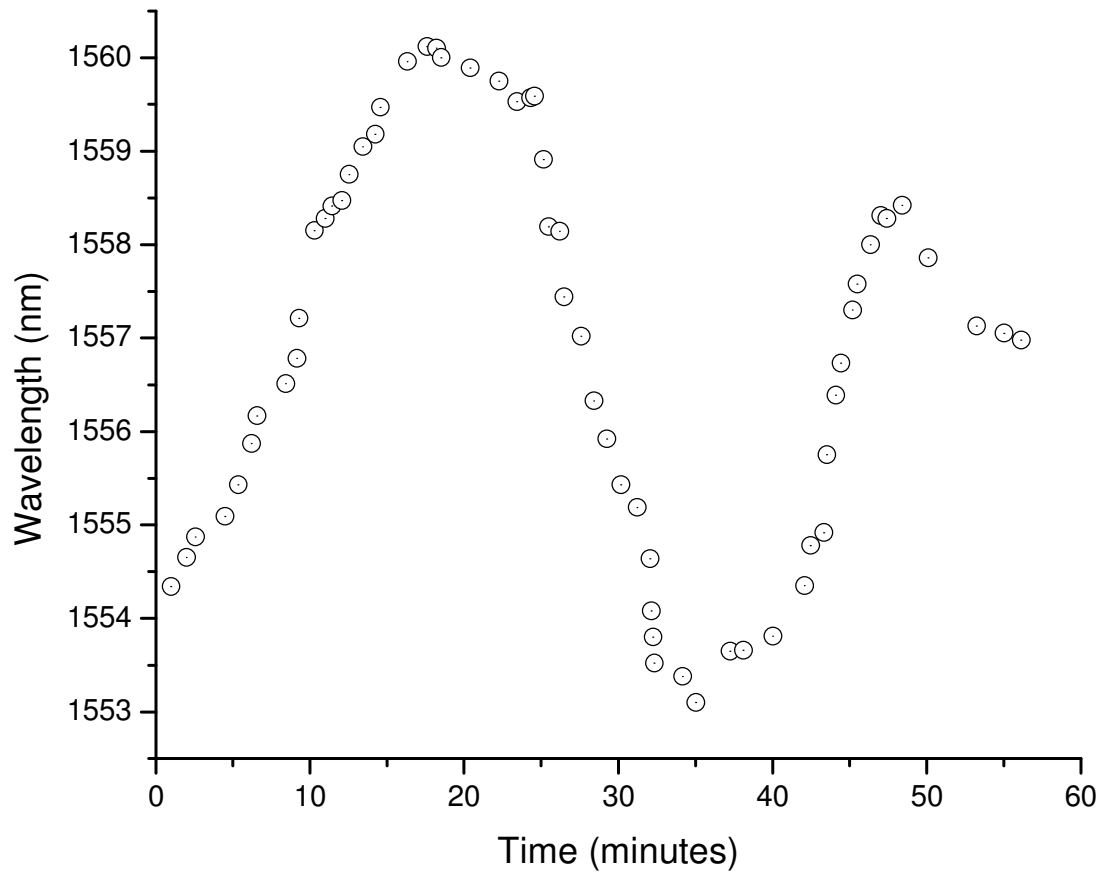


Fig 5.11 Wavelength shifting vs. exposure time

Continuously irradiation induces another red-shifting owing to the unbalanced torque from MR and the twist torque from the ripple grooves. After 50 minutes, further increase of the irradiation time shows no further shifting of the transmission spectrum. However, the transmission spectra become noisy and the corresponding extinction ratio drops. It is known that the MR molecule adsorption increases the depth of the ripple grooves in the structure when the irradiation time increases [109], which affects the light transmission along the PCF. The randomly adsorbed MR dyes can be erasable by heating the PLCF and leaving it in room temperature for few minutes[110] or change the polarization of the Ar^+ laser beam[111].

While the irradiation continues, photoabsorptions of the LC molecules and the subsequent inter- and intra-molecular thermalization give rise to the LCs temperature. The increasing of the bulk temperature and the changes of the density due to laser irradiation induce refractive index changes. As mentioned in Chapter 4, LC phase will change from nematic phase to isotropic phase once the bulk temperature increases to the E7 phase transition temperature. When LCs are in nematic phase, the change of refractive index is due to the change of order parameters and the density. While in isotropic phases, the refractive index changes are due to the density change $\Delta\rho$ following a rise in temperature ΔT .

In the isotropic phase the liquid crystal molecules are randomly orientated. But the laser will induce some degrees of ordering in the random system, as LCs will align themselves in the laser polarization direction in order to minimize the energy through the dipolar interaction if they are under intense laser irradiation. Due to the birefringent properties of LC molecules, this laser-induced partial ordering gives rise to the change of the effective optical dielectric constant. In another way, that is the change of the LC refractive index which is induced by optical field intensity. The reorientation angle of a LC is directly proportional to the laser-induced order parameter, Q , [88]

$$Q \equiv \left\langle \frac{3}{2} \cos^2 \theta - \frac{1}{2} \right\rangle \quad (5.12)$$

which the value of Q can be obtained by a statistical mechanics approach.

5.4 Optical Tuning Realized by Irradiation Polarization Angle

In previous two sections, we have demonstrated that the director axis of LCs could reorientate under laser exposure. By doping with photosensitive or photoreactive materials, LCs will be able to realign themselves at faster pace under irradiation. This photoalignment has played an important role in the development of fabricating liquid crystal display in our daily life. Wolinski et al. has demonstrated controlling LC in PCF with this non-contact alignment approach back in 2007[112, 113]. Azo dye that is used in this chapter owns its unique properties of photoinduced birefringence and dichroism. It is mainly owing to the reversible *trans* to *cis* isomerization and the orientation distribution based on the irradiation beam polarization. Furthermore, by affecting the host liquid crystal orientation, nonlinear or storage-type optical effects can also be induced if the dye molecules undergo orientational changes[114].

Herein, photoalignment is adopted again in the following section to control the LC molecular alignment in the microstructured porous PCF fiber by tuning the polarization of the irradiation laser beam. Optical interference fringes will be used to develop grating structure on the azo-dye doped PLCF region of the fiber. The LC in the dark and bright fringes will be orientated differently, inducing LC refractive index difference and forming the grating structure along the fiber. The details of the *trans-cis* isomerization and molecular displacement during the inscribing process of the grating structure are

explained.

5.4.1 Experimental investigation

The choice of fiber using for this project was still the large mode area PCF (LMA-10) from NKT Photonics A/S. The liquid crystal used was E7 from Merck. Liquid crystals mesogens choose to arrange in special alignment when infiltrating in PCF base on the surface boundary conditions and mesophase in order to lower the disorderliness of the host compounds. The photoalignment materials, azo dye used was Methyl Red (MR) from Merck as well.

MR was added into E7 with the ratio of MR:E7=0.3: 99.7. The empty cleaved PCF (7-8 cm) was placed into the LC mixture for about 30 minutes to allow the sufficient amount of LC and MR mixture infiltrate into the airholes of PCF. Both ends of PCF were then spliced to single mode fiber for experiment. The empty end of PCF was easily sliced to SMF, while for the other end of PLCF, the conditions of the splicer such arc power and arc duration had to be taken into careful consideration. The length of PLCF was controlled at about 30 mm.

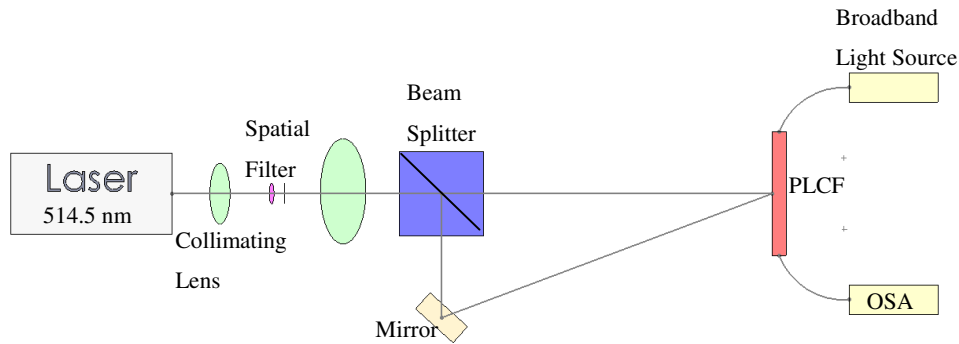


Fig 5.12 Experimental setup for fabrication of fiber bragg grating holographically

Fig 5.12 shows the experimental setup for the fabrication of grating holographically. The setup of this experiment includes Ar^+ laser beam which provides 514.5 nm continuous wave output. The laser is then splitted into two beams after passing through the beam splitter. The two beams meet each other again in the PLCF region. Since these two beams are coherent, they form interference patterns after projecting on the PLCF region. LCs reorientate in different directions for different interference region, generating refractive index modulation. In Section 4.2, we understand that grating structure will be formed if there is periodic refractive index modulation along the PLCF. To have clearer observation, the sample is exposed to lower exposure intensity, which is about 20 mW/cm^2 . It is recommended that to have better grating efficiency the range for exposure intensity should be within 16 mW/cm^2 to 29 mW/cm^2 [115]. As at lower intensity, it might take much longer time to achieve clearer and differentiable structure. But when at higher intensity, the reorientation will occur in very fast pace. And the photo-absorption of MR induces thermal effect and flows, which affecting the grating formation efficiency.

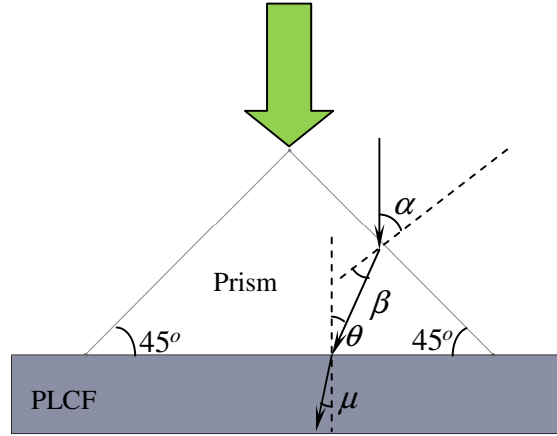


Fig 5.13 Grating Pitch Calculation

The period of the grating structure is dependent on the incident angle and refractive index of the medium. According to Snell's law

$$\sin \alpha = n_{prism} \sin \beta \quad (5.13)$$

where α is 45° . It is the incident angle on the prism. And β is the angle between the transmitted light and normal plane. n_{prism} is 1.52.

After light passing through the prism and transmitting into the fiber as shown in Fig 5.13,

$$n_{prism} \sin \theta = n_{fiber} \sin \mu \quad (5.14)$$

The period of the grating structure can be calculated as

$$\Lambda = \frac{\lambda}{2n_{fiber} \sin \mu} \quad (5.15)$$

By applying Eq(5.14)

$$\Lambda = \frac{\lambda}{2n_{prism} \sin \theta} \quad (5.16)$$

After calculation, the grating spacing is about 569.868 nm.

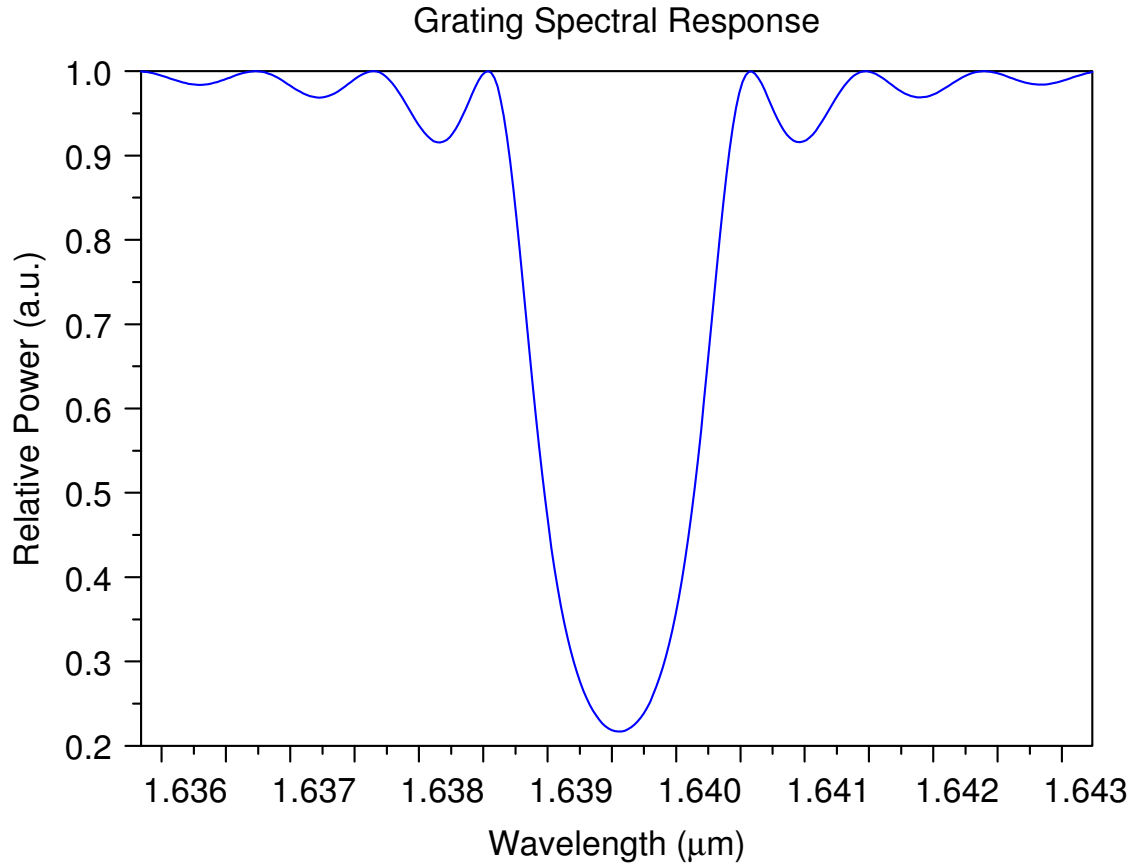


Fig 5.14 Simulated Transmission Dip Location for Grating Pitch of 569.868 nm

The transmission dip position for grating spacing of 569.868 nm is near 1639 nm as shown in Fig 5.14, which is just outside the first transmission band. Due to the limitation of our experimental setup, the transmission dip could not be observed in the optical spectrum analyzer. However, it is found that transmission band switching could be achieved by using the two beam interference.

By removing the beam splitter in Fig 5.12, the transmission spectra are the typical photonic bandgaps. In Section 5.3, we understand that shifting of the transmission

spectrum was observed by increasing of exposure time. The transmission spectrum has been observed shifting again under the irradiation of Ar^+ laser without beam splitter as shown in Fig 5.15.

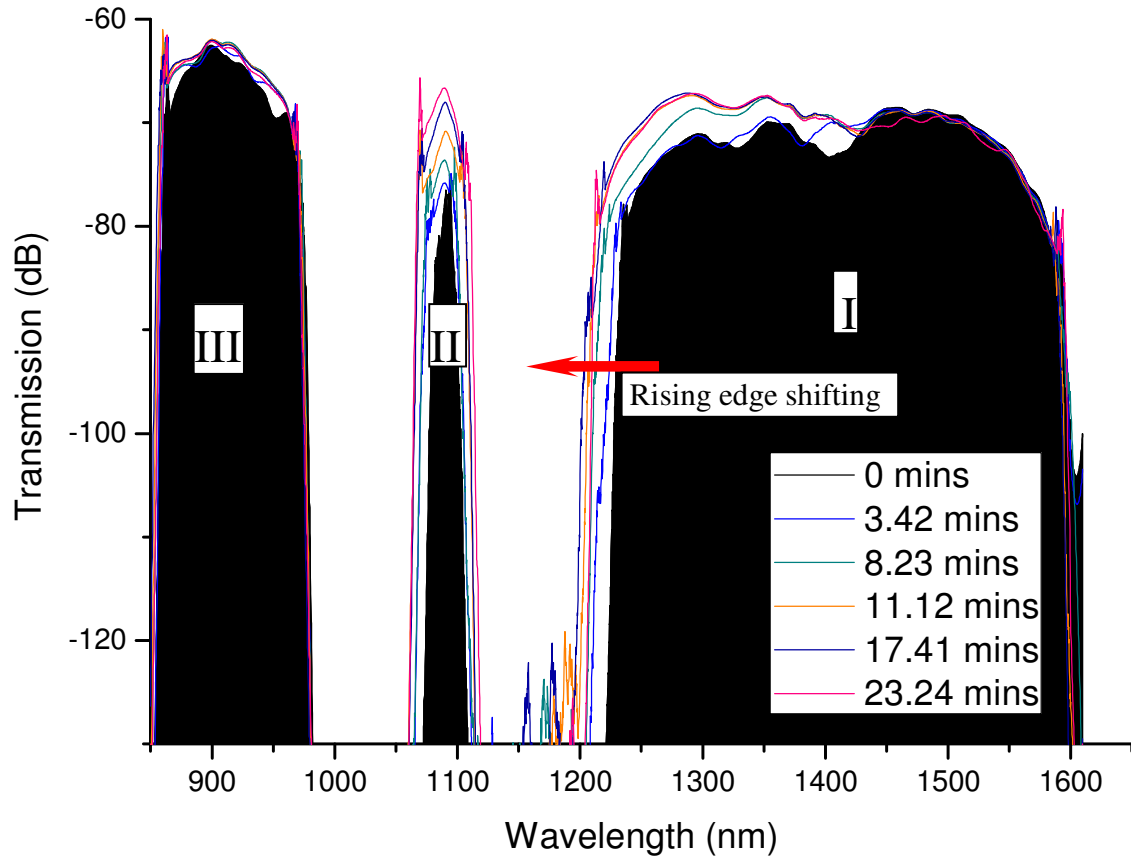


Fig 5.15 Transmission bandgap shifting under laser irradiation without beam splitter

By adding beam splitter in the experimental setup, the interference pattern is projected on the PLCF region. However, the shifting of the first transmission bandgap can hardly be observed; whereas the bandwidth for the second transmission bandgap is widened with the increase of irradiation time as shown in Fig 5.16.

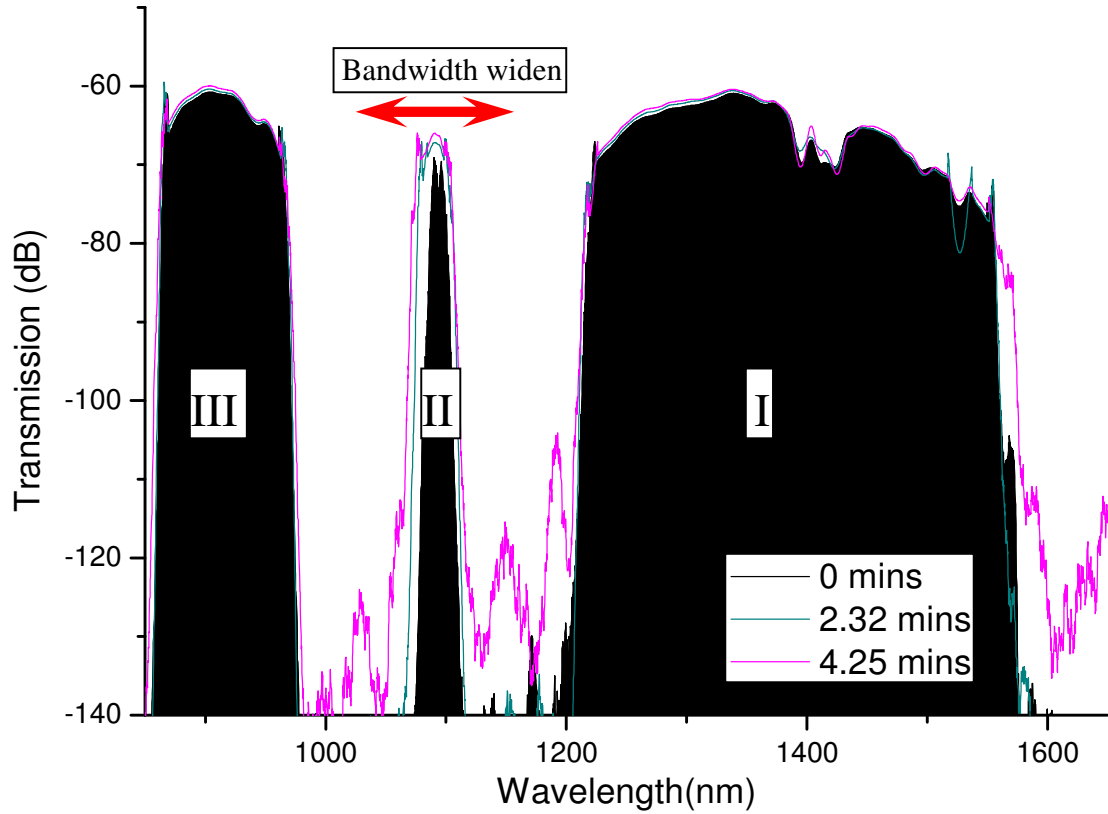


Fig 5.16 Transmission bandgap with beam splitter

For high index anisotropic inclusion of solid core PCF, the locations of the photonic bandgaps are influenced by the ratio of the birefringence and $\sqrt{n_o^2 - n_{core}^2}$ [116]. The locations of the transmission minima are determined by the specific resonant conditions of the LC-filled airholes along the fiber axis, which are related to the modal cutoffs. In this case, the transmission minima for the second bandgap shifts to shorter wavelength, leading to the broaden of the transmission band.

To test the optical tuning effect on the dye-doped PLCF, a polarizer was placed in front of the beam splitter shown in Fig 5.12. It was adjusted 45° away from the fiber axis as shown in Fig 5.17b. Data was recorded for about 32mins.

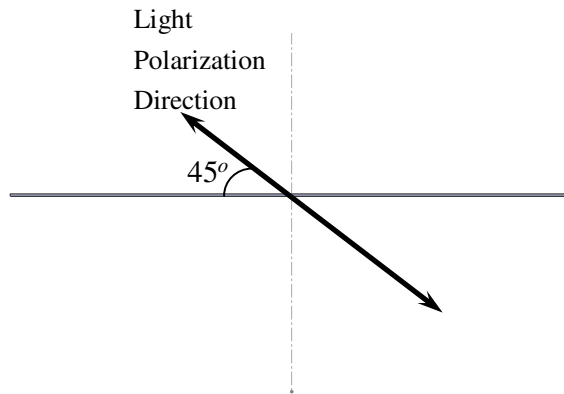
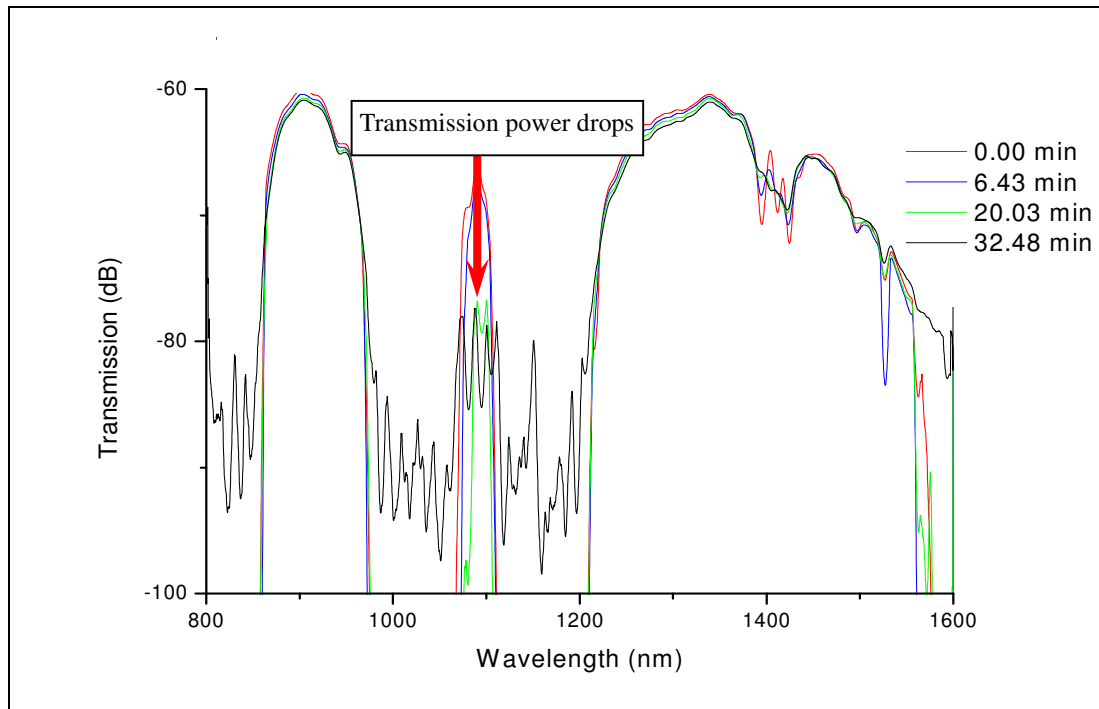


Fig 5.17 Illustration of relationship between polarizer (45° to fiber axis) and liquid crystal

From Fig 5.17a, data was collected from 0 minutes to 32.48 minutes, the second transmission band disappeared slowly when the time increased. It decreased by 15 dB significantly after 32mins. The other two transmission band shift slightly.

A range of reaction happened at exposed grating planes are all associated with the

photoisomerization of MRs under the 45° polarized laser beam. When MRs are excited by the linearly polarized light in its absorption band, they undergo *trans-cis* isomerization. The first transformation occurred is from *trans*-azopolymer to *cis*-azopolymer, which will cause perturbation in refractive indices. Because usually MRs stay at stable *trans* state when it is in the dark, but the pumping laser beam excites MRs in the reactive region when the laser is switched on. But at this point of time, the index modulation, also known as the difference in refractive indices between the exposing grating planes and non exposing grating planes, is of little significant different. However, the LC molecules will be reorientated accordingly owing to the molecular interactions between the LC and MR molecules, which results in the differences in refractive indices between different grating planes. The LC molecules tend to rotate perpendicular to the light polarization direction. The propagation constant of the light travelling along the PLCF will be different in the exposing grating region and the non exposing region.

The numbers of transmission bandgap within certain wavelength range are determined by the number of transmission minima, which depends on the fraction of power η residing in the fiber core [116]. When $\eta=0$, the effective index of the high index cladding are similar to the silica background, which leads to high loss of the transmission minima. When $\eta>0$, the amplitudes of the corresponding transmission minima are extremely small, which leads to a broader transmission band. The refractive index modulation formed by the different LC orientations along the exposing and non-exposing plane

influences the light confinement in the PLCF. The appearances of more transmission dips are observed in the second bandgap, which leading to the lost of the second transmission band.

The anisotropy of the LCs may lead to more transmission dips due to the split of the degeneracy of the modal cutoffs as the electric field in the high-index air-hole inclusion is nearly linear polarized. Moreover, the resonance occurs along the PLCF refractive index modulation region at transmission minima, which brings in additional transmission dips.

The photochemically induced LC phase transition, gradually shift from nematic to isotropic. The incompatible bent of *cis* isomer that caused the perturbation effect can isothermally convert liquid crystal phase into isotropic state shown in Fig 5.18. In other words, it causes disorderliness within the host liquid crystal [105].

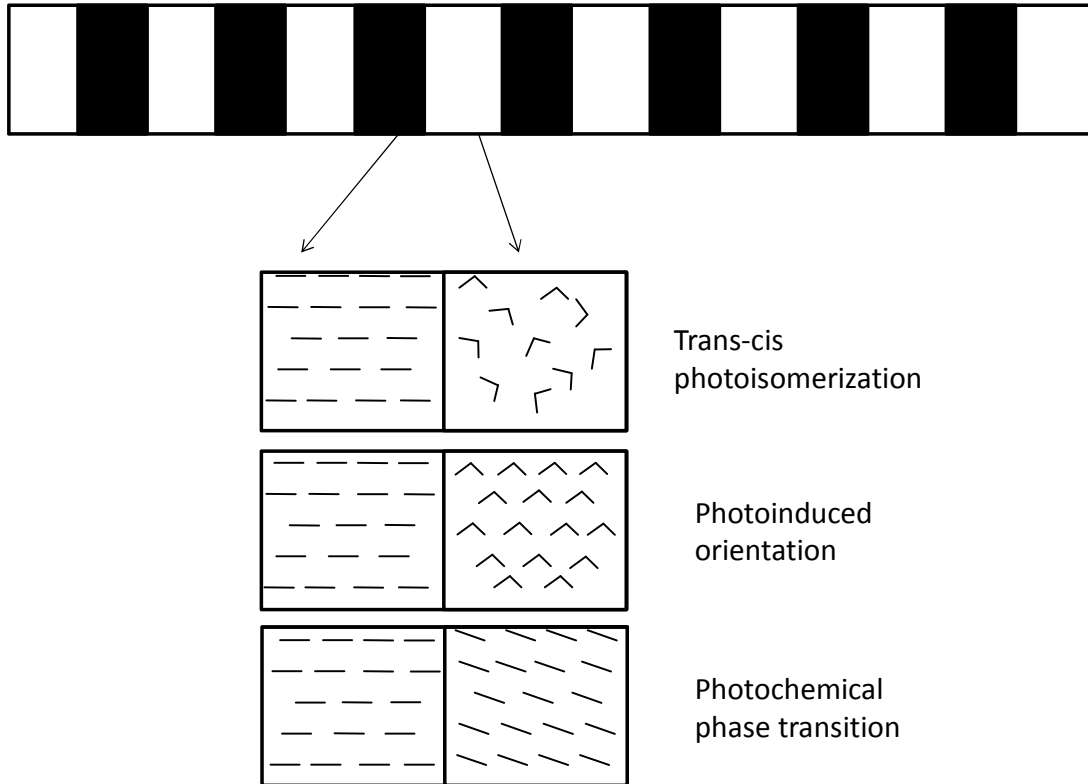
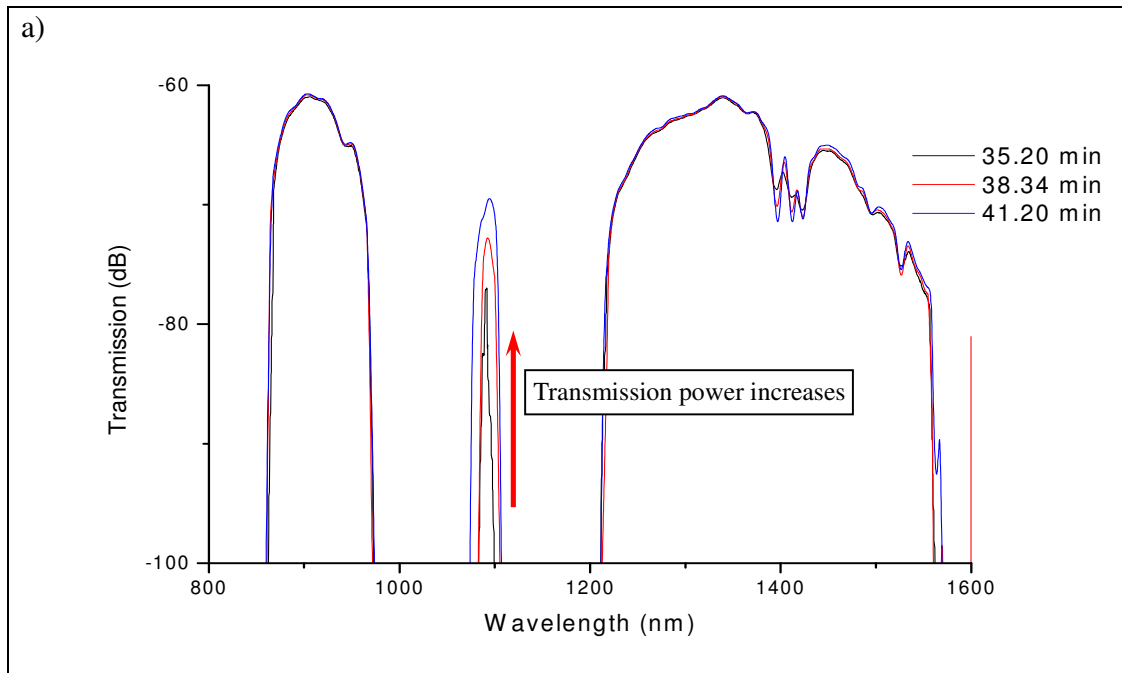


Fig 5.18 Illustration of possible periodic changes in refractive index related to photoisomerization of azobenzene.

White strips designate irradiated area (reactive region)

Due to the thermal tuning sensitivity, the irradiation laser beam would induce thermal change that would cause birefringence. It is believed that the increase in temperature provides convertible energy for the azo dye to transform from the stable *trans* form to *cis* form, accompanied by realignment as well as diffusion in molecular level in each grating plane (reactive region)[117].



b)

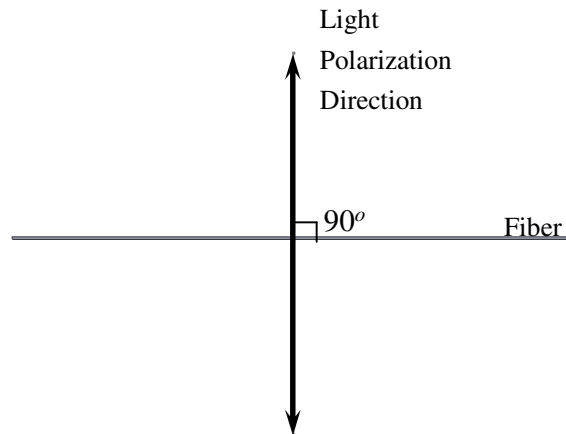


Fig 5.19 Illustration of relationship between polarizer (90° to fiber axis) and liquid crystal

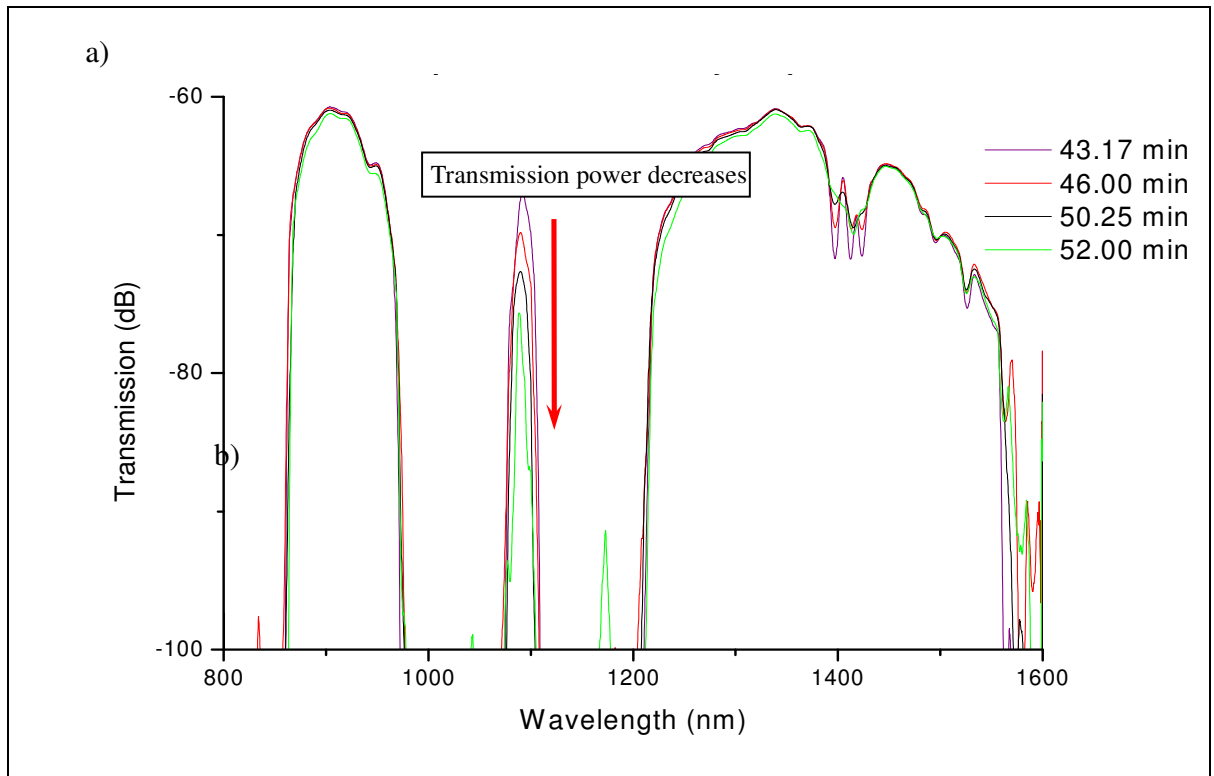
The polarization dependent properties of liquid crystals are studied by striking linearly polarized light waves onto the dye-doped PLCF. In the next stage which starts from 35.20 minutes, the polarizer is turned to the angle of 90° to the fiber axis as shown in Fig 5.19b. From Fig 5.19a, the transmission at bandgap of 1090 nm is gradually increase by 8 dB

significantly.

Different from the previous stage, the various events that happened in the reactive regions are caused by the polarization dependence of dye doped liquid crystal. Due to this unique properties, the convertible thermal energy is now provided to the MR for facilitating molecular reorientation and diffusion of LC to tilt its angle whereby the LCs director are aligned parallel to the fiber axis shown in Fig 5.19b in which the grating is erased.

The perturbation of molecular motion in this stage is mainly because of the photoinduced orientation of azo dye moieties. However, it is believed that the given rise of index changes in this stage is smaller compared to the previous situation. The reason is that due to azopolymer is still in bent *cis* state in the reactive region. The only difference is that the *cis*-azopolymer tilting to facilitate liquid crystal to reorient parallel to the fiber axis. Hence, the situation in this stage would be similar to the situation when the laser beam is about to re-orientate the azopolymer during the previous stage.

The above phenomenon shows that the photoalignment effect is not long term memory effect. The LCs could not be aligned in dye-doped PLCF permanently. The photo-induced orientation effect is erasable and transient in this case.



b)

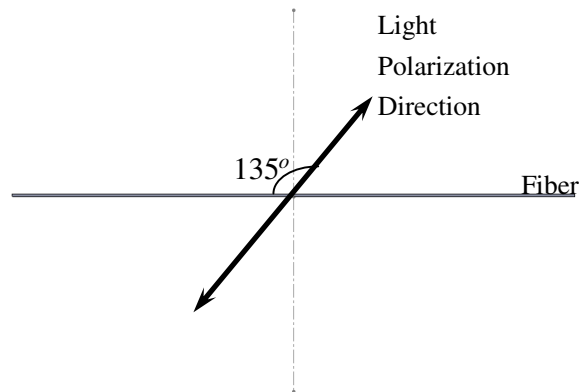


Fig 5.20 Illustration of relationship between polarizer (135° degree to fiber axis) and liquid crystal

The rewritable photoalignment phenomenon is shown in Fig 5.19 owing to its polarization dependence properties of LC. In Fig 5.18, the erasable transient grating structure is proven as LC crystal rearrange back to the initial state of alignment (tilting

90° to the polarizer). From 43.17 minutes to 52.00 minutes, the light is now polarized 135° to the fiber axis. Fig 5.19a shows that the transmission band at 1090 nm region starts to decrease of transmission power by about 8 dB.

For this stage, many similarities with the 45° polarizer is observed here. First, after the erasable effect of the previous stage, all LCs infiltrated in PCF especially in the reactive zone are all horizontally aligned along the fiber axis. Hence, in this stage, the changing direction of polarizer to 135° would induce high perturbation effect to the molecules inside the fiber including the LC and azopolymer. Hereby, the azopolymer in reactive region is still maintained in *cis* state because it is still exposed to light and they are still maintained in isotropic state. However, LCs are much dependent on the polarization of light. They would consume the thermal energy which is provided from the laser irradiation light and gradually tilt their angle to become perpendicular to the polarized light (shown in Fig 5.20) with the facilitation of the azopolymer.

Different from Fig 5.17, instead of rapid decrease of transmission, the transmission power only drop by half compared to Fig 5.17. It could be the reason that the accumulation of the absorbed azo dyes on the microstructured porous fiber increases the anchoring force of fiber with pumping.

5.5 Chapter Summary

This study has demonstrated the photoalignment of liquid crystal in PCF by using methyl-red dye which is obtained by infiltrating MR doped liquid crystals into the PCF air holes located within the cladding region. The green laser light beam excites the MR molecules in the PLCF. When the MR molecules are excited, the molecules undergo *trans-cis* transformation. They adsorb onto the capillary surfaces of the PLCF cladding holes with their long axes perpendicular to the direction of polarization of the laser beam[118]. These adsorbed dye molecules then re-orientate the LC molecules, changing the pre-tilted angle θ of LCs in the PLCF. This results in a change of B_{LC} in the PLCF region.

The photoalignment method employed in aligning LC in PCF can be used in a tunable device. Because of LC anisotropy the PLCF possess a tunable birefringence. Its birefringent property has been optically tuned by modulating the laser irradiation time. Moreover the birefringence tunability can be applied on the fabrication of the grating structure on dye-doped PLCF as well. Hence, it is believed that with the erasable and rewritable effects, it has a great potential for practical future applications that can enable creation of greatly tunable fiber applications in smaller scale. Thus, this makes them easier to be used in the field of telecommunication and sensing system.

Chapter 6

Conclusions and Future Works

6.1 Summary of the investigation

This thesis reports the investigation results on the modifications of the photonic liquid crystal fiber transmission spectrum in different approaches. The investigation mainly focuses on the photonic crystal fiber sensing and afterwards integrating liquid crystals into the PCF to achieve tuning ability of the setup. The work that has been done can be summarized as followings.

In order to have some understanding of optical fiber sensing, optical fiber long period grating glucose sensor has been developed. The cladding of the LPG section is etched by hydrofluoric acid in order to allow more evanescent field to penetrate from the core into the surrounding medium and thus enhancing the sensitivity of the fiber-based sensor significantly. The enzymes, glucose oxidase, are immobilized around the LPG section by sol-gel technique. The sol-gel glass offers a better way to immobilize biomolecules within its optically transparent matrix, while retaining the functional activity of the encapsulated biomolecules [119]. It is shown that long period grating transmission dip shifts when the glucose concentration changes. The experiment shows that LPGs allow direct quantitative chemical measurements of the medium surrounding the fiber cladding.

However the drawback is that the removing of the fiber cladding makes the fiber very fragile to handle.

With the invention of photonic crystal fiber, different research groups make different approaches for developing grating structure in the fiber core. Owing to the air holes cladding, forming grating structures in PCF is a difficult task. Thus long period grating induced by mechanical pressure offers more flexibility and tunability on the grating inscription and period. The LPG grating fringes are formed by mechanically pressing a periodic V-groove brass block on the fiber. The strain induces a periodical refractive index variation on the fiber by photoelastic effect. Larger refractive index perturbation is induced if the applied pressure on the V-groove plate increases, resulting stronger mode coupling. Titled grating is formed when the fiber is placed slantingly on the V-groove plate. The transmission dip shifts to the blue region when the tilted angle increases. The larger tilted angle it forms, the larger blue shifting of the transmission dip it induces.

Another unique property of PCF is that it is possible to introduce additional material into the fiber to achieve new features, such as infiltrating refractive index liquid into the PCF air holes. Filling of high index liquid into the air holes of solid core PCFs increases the effective index of the cladding region, changing the light guiding mechanism to photonic bandgap effect. The refractive index of the filled solution changes if the ambient temperature changes. The photonic band edge shiftings owing to the cladding refractive index variation are able to be evaluated by the refractive index scaling law. This provides

an alternative way for temperature sensing by using photonic crystal fiber. It avoids the inconveniences of writing grating in optical fibers, especially for grating in photonic crystal fiber, and yet provides higher sensitivity than un-doped optical fiber sensors.

Other than refractive index liquid, infiltrating liquid crystal introduces more interesting features for PCF. By filling liquid crystal into the PCF, it introduces birefringence in the PCF. Any changes of liquid crystal birefringence will cause the PCF transmission spectrum changes. Thermotropic liquid crystal is sensitive to ambient temperature changes. When the liquid crystal is heated over its phase transition temperature, it undergoes phase change from nematic phase to isotropic phase. When temperature changes, liquid crystal in the PCF would flow and rotate, resulting in the change of the PLCF birefringence. The shifting of the transmission spectrum due to the changes of liquid crystal birefringence is not linear. Thus it may not be suitable for temperature sensing. However, temperature tuning could be achieved.

Another unique property of liquid crystal is that its orientation can be changed when there is an applied electric field. When external electric field is applied, the liquid crystals reorient themselves to be parallel to the electric field. If placing the photonic liquid crystal fiber between a periodically comb metal plate and an electrode, a periodic grating is formed due to the different voltage levels in the periodically metal plate. The transmission dip of the grating structure can be tuned when the strength of the external field applied changes.

Besides temperature and electrical tuning, optical tuning of photonic liquid crystal fiber can also be achieved by doping azo dye with liquid crystals. By employing a green laser light to irradiate the PLCF sample; the photoalignment mechanism causes the photo-excited Methyl-red (MR) molecules to interact with bulk LC molecules in the PCF as the MR molecules undergo a series of transformations. One of the changes is photoinduced adsorption of the MR molecules which results in LC realignment indicated by the transmission spectrum shifting. The shift in the transmission spectrum is related to the birefringence change due to the realignment. The transmission spectrum can also be altered by changing the irradiation light polarization. The LCs inside the PLCF reorientated their director axis perpendicular to the polarizer. By changing the polarizer angle, LCs reorientation changes accordingly.

Infiltration of different materials into PCF opens up different opportunities for PCF sensing. Enzymatic optical fiber sensing can also be achieved by coating enzymes on the air hole surface. However, homogeneous coating on the air hole surface is very difficult to achieve and the thickness of the coating is hard to control as well.

6.2 Suggestion of Future Work

PCFs are a new class of optical fibers and their properties are still being explored. In order to integrate them as biochemical sensing devices, many issues need to be addressed. Several important approaches, especially the tuning properties of photonic liquid crystal fiber, have been studied in this research project. However, due to the time and the

experimental limitations, some promising directions were identified but could not be pursued. I have listed the following suggestions for the future work.

6.2.1 Structure and boundary condition

To get full control of the photonic liquid crystal fiber tuning properties, the boundary condition has to be taken into account. The boundary condition is determined by the anchoring conditions of liquid crystals on the airholes surface, which can be controlled by either chemical or mechanical treatments [120]. In the photonic liquid crystal fiber the anchoring type of liquid crystals will be a function of position and characterized by a set of length scales. Hence the length of the infiltrated liquid crystal inside the fiber and the surface condition will dictate the degree and spatial distribution of anchoring.

6.2.2 Coating of Enzyme

Another issue that has not been investigated is the PCF as enzymatic sensor. In earlier numerical work, the polymer coating is assumed to be uniform inside air holes. However, it is very difficult to achieve experimentally. And coating of enzyme on air holes surface is hard to control as well. Any sediment due to chemical reaction will lead to the blocking of the air holes. By employing high pressure chemical vapor deposition, homogeneous coating could be achieved and the coating thickness is controllable.

6.2.3 Integrate them into microfluidic chip

Liquid crystal is a very interesting material. The PLCF could be integrated with

microfluidic chip. The temperature, electrical and optical tuning properties of the PLCF could be used as switches in different scenarios. Furthermore, protein adsorption on the LC coating substrate will modify the anchoring condition of LC. This could be developed as biosensor as well. However, alignment of the channels in the microfluidic chip and the PCF, the efficiency of light coupling into the PCF waveguide and selective sample infiltration will be the major challenges for the integration.

Author's Publications

Journal papers:

1. **Y.F. Zhang**, C.C. Chan, Y. Peck, P. Zu, D. Luo and X.W. Sun, "Optical Tunable Filter Realized by Dye-Doped Photonic Liquid Crystal Fiber", Submitted
2. **Y.F. Zhang**, C.C. Chan, M.X.A Chia and P. Zu, "Temperature Effect of Liquid Crystal in Photonic Bandgap Fiber-Based Sagnac Loop", IEEE Sensors Journal, vol 12 (5), pp. 1609-1610, 2012
3. **Y.F. Zhang**, C.C. Chan, Y.M. Chan and P. Zu, "Tilted Long Period Gratings Pressure Sensing in Solid Core Photonic Crystal Fibers", IEEE Sensors Journal, vol 12 (5), pp. 954-957, 2012
4. **Y.F. Zhang**, C.C. Chan, and J. Sun "Enhancement of temperature measurement by using photonic bandgap effect", SENSORS AND ACTUATORS A-PHYSICAL, vol 157 (2), pp. 276-279, 2010
5. H.P. Gong, C.C. Chan, **Y.F. Zhang** and W.C. Wong, "Temperature Sensor Based on Modal Interference in Hollow-Core Photonic Bandgap Fiber With Collapse Splicing ", IEEE Sensors Journal, vol 12 (5), pp. 1421-1424, 2012
6. W.C. Wong, C.C. Chan, **Y.F. Zhang** and K.C Leong, "Miniature Single-Mode Fiber Refractive Index Interferometer Sensor Based on High Order Cladding Mode and Core-Offset", IEEE Photonics Technology Letters, vol 24 (5), pp. 359-361, 2012
7. H.P. Gong, C.C. Chan, **Y.F. Zhang**, W.C Wong and X.Y Dong, "Miniature refractometer based on modal interference in a hollow-core photonic crystal fiber with collapsed splicing", Journal of Biomedical Optics, vol 16, 2011
8. Y.X. Jin, C.C. Chan, **Y.F. Zhang**, X.Y Dong and P Zu, "Temperature sensor based on a pressure-induced birefringent single-mode fiber loop mirror", Measurement Science & Technology, vol 21(6), 2010
9. Y.X. Jin, C.C. Chan, **Y.F. Zhang** and X.Y Dong, "Mechanically induced long-period fiber grating in side-hole single-mode fiber for temperature and refractive sensing", Optics Communications, vol 283(7), pp. 1303-1306, 2010

10. J. Sun, C.C. Chan, **Y.F. Zhang** and P. Shum, "Analysis of hollow-core photonic bandgap fibers for evanescent wave biosensing", *Journal of Biomedical Optics*, vol 13(5), 2008

Conference papers:

1. **Y. F. Zhang**, C. C. Chan, J. Sun, "Enhancement of Temperature Measurement by using Photonic Bandgap Effect", 20th international conference on Optical Fiber Sensors (OFS), Edinburgh, UK, 2009
2. **Y. F. Zhang**, C. C. Chan, J. Sun, "Solid-core Photonic Bandgap Fiber with Polymer Coating for Biosensing Applications", Asia-Pacific Optical Communications, Wuhan, China, 2008
3. **Y. F. Zhang**, C. C. Chan and J. Sun "Long Period Grating Glucose Sensor Based on Sol-gel Entrapment Technique", International Conference on Advanced Infocomm Technology, Shenzhen, China, 2008
4. P. Zu, C.C. Chan and **Y.F. Zhang**, "Dispersion properties of Liquid Photonic Crystal Fiber", Conference on Advanced Sensor Systems and Applications IV, Beijing, Peoples R China, , 2010
5. J. Sun, C.C. Chan, **Y.F. Zhang** and P. Shum, "Antiresonant guiding photonic crystal fibers for measuring refractive index", 19th international conference on Optical Fiber Sensors (OFS), Perth, Australia, 2008
6. J. Sun, C.C. Chan, **Y.F. Zhang** and P. Shum, "Analysis of hollow-core photonic bandgap fibers for evanescent-wave biosensing", 6th international conference on Optics-photonics Design & Fabrication, Taipei, Taiwan, 2008
7. J. Sun, C. C. Chan, **Y. F. Zhang**, L. T. Zheng, H. L. Ho, X. Y. Dong, L. Y. Shao, "Glucose optical biosensor with sol-gel-coated long-period gratings", Asia-Pacific Optical Communications, Wuhan, China, 2008
8. J. Sun, C. C. Chan, **Y. F. Zhang**, "Single polarization guidance in liquid-crystal photonic bandgap fibers", International Conference on Advanced Infocomm Technology, Shenzhen, China, 2008

Bibliography

- [1] T. G. Giallorenzi, et al., "Optical fiber sensor technology," *IEEE Journal of Quantum Electronics*, vol. 18, pp. 626-665, 1982.
- [2] J. D. Joannopoulos, et al., "Photonic crystals: Putting a new twist on light," *Nature*, vol. 386, pp. 143-149, Mar 1997.
- [3] P. Russell, "Photonic crystal fibers," *Science*, vol. 299, pp. 358-362, Jan 2003.
- [4] O. S. Wolfbeis, "Fiber-optic chemical sensors and biosensors," *Analytical Chemistry*, vol. 76, pp. 3269-3283, Jun 2004.
- [5] M. D. Marazuela and M. C. Moreno-Bondi, "Fiber-optic biosensors - an overview," *Analytical and Bioanalytical Chemistry*, vol. 372, pp. 664-682, Mar 2002.
- [6] A. Yariv, "Coupled-mode theory for guided-wave optics," *IEEE Journal of Quantum Electronics*, vol. QE 9, pp. 919-933, 1973.
- [7] T. Erdogan, "Cladding-mode resonances in short- and long-period fiber grating filters," *Journal of the Optical Society of America a-Optics Image Science and Vision*, vol. 14, pp. 1760-1773, Aug 1997.
- [8] A. Asseh, et al., "Fiber optical Bragg grating refractometer," *Fiber and Integrated Optics*, vol. 17, pp. 51-62, 1998.
- [9] V. Bhatia and A. M. Vengsarkar, "Optical fiber long-period grating sensors," *Optics Letters*, vol. 21, pp. 692-694, May 1996.
- [10] A. D. Kersey, et al., "Fiber grating sensors," *Journal of Lightwave Technology*, vol. 15, pp. 1442-1463, Aug 1997.
- [11] Y. J. Rao, "In-fibre Bragg grating sensors," *Measurement Science & Technology*, vol. 8, pp. 355-375, Apr 1997.
- [12] D. A. Pereira, et al., "Fiber Bragg grating sensing system for simultaneous measurement of salinity and temperature," *Optical Engineering*, vol. 43, pp. 299-304, Feb 2004.
- [13] H. J. Patrick, et al., "Analysis of the response of long period fiber gratings to external index of refraction," *Journal of Lightwave Technology*, vol. 16, pp. 1606-1612, Sep 1998.
- [14] T. Eftimov, "Sensor applications of LPGs and FBGs," *Optical Sensing & Imaging*, 2006.
- [15] A. Quirrenbach, "Optical interferometry," *Annual Review of Astronomy and Astrophysics*, vol. 39, pp. 353-401, 2001.
- [16] B. H. Lee, et al., "Interferometric Fiber Optic Sensors," *Sensors*, vol. 12, pp. 2467-2486, Mar 2012.
- [17] X. Li, et al., "Research on Laser Spectrum Detecting Technology Based on Static Mach-Zehnder Interferometer," *Spectroscopy and Spectral Analysis*, vol.

- 29, pp. 62-65, Jan 2009.
- [18] B. Culshaw, "The optical fibre Sagnac interferometer: an overview of its principles and applications," *Measurement Science & Technology*, vol. 17, pp. R1-R16, Jan 2006.
 - [19] R. Anderson, et al., "Sagnac effect - A century of earth-rotated interferometers," *American Journal of Physics*, vol. 62, pp. 975-985, Nov 1994.
 - [20] E. Yablonovitch, et al., "Photonic band-structure - the face-centered-cubic case employing nonspherical atoms," *Physical Review Letters*, vol. 67, pp. 2295-2298, Oct 1991.
 - [21] P. S. J. Russell, "Photonic-crystal fibers," *Journal of Lightwave Technology*, vol. 24, pp. 4729-4749, Dec 2006.
 - [22] T. A. Birks, et al., "Endlessly single-mode photonic crystal fiber," *Optics Letters*, vol. 22, pp. 961-963, Jul 1997.
 - [23] J. C. Knight, "Photonic crystal fibres," *Nature*, vol. 424, pp. 847-851, Aug 2003.
 - [24] A. C. Federica Poli, Stefano Selleri, Ed., *Photonic crystal fibers: properties and applications*. Netherlands: Springer, 2007.
 - [25] R. Buczynski, "Photonic crystal fibers," *Acta Physica Polonica A*, vol. 106, pp. 141-167, Aug 2004.
 - [26] D. C. Zografopoulos, et al., "Photonic crystal-liquid crystal fibers for single-polarization or high- birefringence guidance," *Optics Express*, vol. 14, pp. 914-925, Jan 2006.
 - [27] T. A. Birks, et al., "Approximate band structure calculation for photonic bandgap fibres," *Optics Express*, vol. 14, pp. 9483-9490, Oct 2006.
 - [28] R. V. K. Wes R. Jamroz, Emile I. Haddad, Ed., *Applied microphotronics*. Boca Raton: Taylor and Francis Group, 2006.
 - [29] S.-T. W. Iam-Choon Khoo, Ed., *Optics and Nonlinear Optics of Liquid Crystals*. World Scientific, 1993.
 - [30] H. Kelker, "History of Liquid Crystals," *Molecular Crystals and Liquid Crystals*, vol. 21, pp. 1-48, 1973.
 - [31] S. Chandrasekhar and N. V. Madhusudana, "Liquid crystals," *Annual Review of Materials Science*, vol. 10, 1980.
 - [32] D. Demus, Ed., *Phase types, structures and chemistry of liquid crystals* (Horst Stegemeyer, *Liquid Crystals*. New York: Springer, 1994.
 - [33] S. Chandrasekhar, Ed., *Liquid Crystals*. New York: Cambridge University Press, 1992s.
 - [34] M. K. Mandal, Ed., *Multimedia Signals and Systems*. Boston/ Dordrecht/ London: Kluwer Academic Publishers, 2003.
 - [35] Nematic Phase of Liquid Crystal. Available: <http://upload.wikimedia.org/wikipedia/commons/8/80/LiquidCrystal-MesogenOrder-Nematic.jpg>
 - [36] Smectic Phases of Liquid Crystal. Available:

- <http://upload.wikimedia.org/wikipedia/commons/f/f2/LiquidCrystal-MesogenOrder-SmecticPhases.jpg>
- [37] Chiral Phase of Liquid Crystal. Available: <http://upload.wikimedia.org/wikipedia/commons/b/bf/LiquidCrystal-MesogenOrder-ChiralPhases.jpg>
- [38] Y. Jeong and B. Lee, "Theory of electrically controllable long-period gratings built in liquid-crystal fibers," *Optical Engineering*, vol. 40, pp. 1227-1233, Jul 2001.
- [39] I. C. Khoo, "Nonlinear optics of liquid crystalline materials," *Physics Reports-Review Section of Physics Letters*, vol. 471, pp. 221-267, Feb 2009.
- [40] Photos of Various Fluorescent Dyes. Available: <http://upload.wikimedia.org/wikipedia/commons/thumb/0/09/FluorescentCells.jpg/200px-FluorescentCells.jpg>
- [41] N. A. Davidenko, et al., "Optical, electrical, and photophysical properties of films of polycomplexes of azobenzene derivatives with cobalt," *Optics and Spectroscopy*, vol. 101, pp. 906-913, Dec 2006.
- [42] High resolution scanning tunneling microscopy image of Carbon Nanotube Available: <http://upload.wikimedia.org/wikipedia/commons/5/5f/Chiraltube.gif>
- [43] Multi-Walled Carbon Nanotube. Available: http://upload.wikimedia.org/wikipedia/commons/b/bc/Multi-walled_Carbon_Nanotube.png
- [44] Rolling of a layer of graphene into a seamless Carbon Nanotube. Available: http://upload.wikimedia.org/wikipedia/commons/c/c4/Carbon_nanoribbon_povray.PNG
- [45] "Rolling of a layer of graphene into a seamless Carbon Nanotube."
- [46] C. Fantini, et al., "Optical transition energies for carbon nanotubes from resonant Raman spectroscopy: Environment and temperature effects," *Physical Review Letters*, vol. 93, Oct 2004.
- [47] J. K. Lim, et al., "A phase-stabilized carbon nanotube fiber laser frequency comb," *Optics Express*, vol. 17, pp. 14115-14120, Aug 2009.
- [48] D. G. Georganopoulou, et al., "Nanoparticle-based detection in cerebral spinal fluid of a soluble pathogenic biomarker for Alzheimer's disease," *Proceedings of the National Academy of Sciences of the United States of America*, vol. 102, pp. 2273-2276, Feb 2005.
- [49] X. Liu, et al., "A one-step homogeneous immunoassay for cancer biomarker detection using gold nanoparticle probes coupled with dynamic light scattering," *Journal of the American Chemical Society*, vol. 130, pp. 2780+, Mar 2008.
- [50] M. Grande, et al., "Asymmetric plasmonic grating for optical sensing of thin layers of organic materials," *Sensors and Actuators B-Chemical*, vol. 160, pp. 1056-1062, Dec 2011.
- [51] TEM Images of Silica Nanoparticle. Available:

- http://upload.wikimedia.org/wikipedia/commons/6/6d/Mesoporous_Silica_Nanoparticle.jpg
- [52] A. B. W. J. Hecht, Ed. York, Ed., *Understand Fiber Optics*. PA: Pearson Prentice Hall, 2006.
 - [53] K. T. V. Grattan, Ed., *Optical Fiber Sensor Technology: Devices and Technology*. Springer, 1997.
 - [54] A. D. Kersey, et al., "High-resolution fiber-grating based strain sensor with interferometric wavelength-shift detection," *Electronics Letters*, vol. 28, pp. 236-238, Jan 1992.
 - [55] Y. Z. Zhu and A. B. Wang, "Miniature fiber-optic pressure sensor," *Ieee Photonics Technology Letters*, vol. 17, pp. 447-449, Feb 2005.
 - [56] J. Broeng, et al., "Photonic crystal fibers: A new class of optical waveguides," *Optical Fiber Technology*, vol. 5, pp. 305-330, Jul 1999.
 - [57] X. W. Shu, et al., "Sensitivity characteristics of long-period fiber gratings," *Journal of Lightwave Technology*, vol. 20, pp. 255-266, Feb 2002.
 - [58] S. W. James and R. P. Tatam, "Optical fibre long-period grating sensors: Characteristics and application," *Measurement Science & Technology*, vol. 14, pp. R49-R61, 2003.
 - [59] S. Shtelzer and S. Braun, "An optical biosensor based upon glucose-oxidase immobilized in sol-gel silicate matrix," *Biotechnology and Applied Biochemistry*, vol. 19, pp. 293-305, Jun 1994.
 - [60] W. W. M. G. Meltz, and W. H. Glenn, "In-fibre Bragg grating tap," presented at the Optical fiber Communication Conference, OFC'90, San Francisco, 1990.
 - [61] G. Laffont and P. Ferdinand, "Tilted short-period fibre-Bragg-grating-induced coupling to cladding modes for accurate refractometry," *Measurement Science & Technology*, vol. 12, pp. 765-770, Jul 2001.
 - [62] C. Caucheteur, et al., "Tilted Fiber Bragg Grating Refractometer Using Polarization-Dependent Loss Measurement," *Ieee Photonics Technology Letters*, vol. 20, pp. 2153-2155, Nov-Dec 2008.
 - [63] C. Chen, et al., "The sensitivity characteristics of tilted fibre Bragg grating sensors with different cladding thicknesses," *Measurement Science & Technology*, vol. 18, pp. 3117-3122, Oct 2007.
 - [64] T. Guo, et al., "Temperature-independent tilted fiber grating vibration sensor based on cladding-core recoupling," *Optics Letters*, vol. 33, pp. 1004-1006, May 2008.
 - [65] E. Kerrinckx, et al., "Suppression of discrete cladding mode resonances in fibre slanted Bragg gratings for gain equalisation," *Optics Express*, vol. 14, pp. 1388-1394, Feb 2006.
 - [66] C. W. Haggans, et al., "Narrow-band rejection filters with negligible backreflection using tilted photoinduced gratings in single-mode fibers," *Ieee Photonics Technology Letters*, vol. 10, pp. 690-692, May 1998.

-
- [67] H. S. Park, et al., "All-fiber add-drop wavelength-division multiplexer based on intermodal coupling," *IEEE Photonics Technology Letters*, vol. 13, pp. 460-462, May 2001.
- [68] E. Marin, et al., "Bragg gratings in 2 x 2 symmetric fused fiber couplers: Influence of the tilt on the wavelength response," *IEEE Photonics Technology Letters*, vol. 11, pp. 1434-1436, Nov 1999.
- [69] X. Yu, et al., "Highly Sensitive Photonic Crystal Fiber-Based Refractive Index Sensing Using Mechanical Long-Period Grating," *IEEE Photonics Technology Letters*, vol. 20, pp. 1688-1690, Sep-Oct 2008.
- [70] J. H. Lim, et al., "Tunable fiber gratings fabricated in photonic crystal fiber by use of mechanical pressure," *Optics Letters*, vol. 29, pp. 331-333, Feb 2004.
- [71] R. Kashyap, *Fiber Bragg Gratings*, Second ed.: Elsevier Inc., 2010.
- [72] L. Dong, et al., "Coupling characteristics of cladding modes in tilted optical fiber Bragg gratings," *Applied Optics*, vol. 37, pp. 5099-5105, Aug 1998.
- [73] G. Antonopoulos, et al., "Experimental demonstration of the frequency shift of bandgaps in photonic crystal fibers due to refractive index scaling," *Optics Express*, vol. 14, pp. 3000-3006, Apr 2006.
- [74] T. A. Birks, et al., "Scaling laws and vector effects in bandgap-guiding fibres," *Optics Express*, vol. 12, pp. 69-74, Jan 2004.
- [75] X. Yu, et al., "Photonic crystal fibers with high index infiltrations for refractive index sensing," *Optics Communications*, vol. 281, pp. 4555-4559, Sep 2008.
- [76] J. Zeng, et al., "Applications of optical fiber SPR sensor for measuring of temperature and concentration of liquids," in *17th International Conference on Optical Fibre Sensors*, Brugge, Belgium, 2005, pp. 667-670.
- [77] J. Sun and C. C. Chan, "Photonic bandgap fiber for refractive index measurement," *Sensors and Actuators B-Chemical*, vol. 128, pp. 46-50, Dec 2007.
- [78] J. B. Jensen, et al., "Photonic crystal fiber based evanescent-wave sensor for detection of biomolecules in aqueous solutions," *Optics Letters*, vol. 29, pp. 1974-1976, Sep 2004.
- [79] R. A. Potyrailo, et al., "A dual-parameter optical sensor fabricated by gradient axial doping of an optical fibre," *Measurement Science & Technology*, vol. 16, pp. 235-241, Jan 2005.
- [80] W. Peng, et al., "Investigation of dual-channel fiber-optic surface plasmon resonance sensing for biological applications," *Opt. Lett.*, vol. 30, pp. 2988-2990, 2005.
- [81] M. A. van Eijkelenborg, et al., "Microstructured polymer optical fibre," *Optics Express*, vol. 9, pp. 319-327, Sep 2001.
- [82] J. Jensen, et al., "Selective detection of antibodies in microstructured polymer optical fibers," *Opt. Express*, vol. 13, pp. 5883-5889, 2005.
- [83] P. N. Prasad, "Optical Biosensors," *Introduction to Biophotonics*, pp. 311 - 356,

- 2003.
- [84] M. P. DeLisa, et al., "Evanescent wave long-period fiber bragg grating as an immobilized antibody biosensor," *Analytical Chemistry*, vol. 72, pp. 2895-2900, 2000.
 - [85] P. J. A. Sazio, et al., "Microstructured optical fibers as high-pressure microfluidic reactors," *Science*, vol. 311, pp. 1583-1586, Mar 2006.
 - [86] J. Sun, et al., "High-resolution photonic bandgap fiber-based biochemical sensor," *Journal of Biomedical Optics*, vol. 12, Jul-Aug 2007.
 - [87] L. Rindorf, et al., "Photonic crystal fiber long-period gratings for biochemical sensing," *Opt. Express*, vol. 14, pp. 8224-8231, 2006.
 - [88] I.-C. Khoo, Ed., *Liquid Crystals*. John Wiley & Sons, 2007.
 - [89] T. R. Wolinski, et al., "Polarization optics of microstructured liquid crystal fibers," *Molecular Crystals and Liquid Crystals*, vol. 454, pp. 325-342, 2006.
 - [90] S. T. Kowel, et al., "Focusing by electrical modulation of refraction in a liquid-crystal cell," *Applied Optics*, vol. 23, pp. 278-289, 1984.
 - [91] L. A. Madsen, et al., "Thermotropic biaxial nematic liquid crystals," *Physical Review Letters*, vol. 92, Apr 2004.
 - [92] J. B. Du, et al., "Electrically tunable Sagnac filter based on a photonic bandgap fiber with liquid crystal infused," *Optics Letters*, vol. 33, pp. 2215-2217, Oct 2008.
 - [93] D. H. Kim and J. U. Kang, "Sagnac loop interferometer based on polarization maintaining photonic crystal fiber with reduced temperature sensitivity," *Optics Express*, vol. 12, pp. 4490-4495, Sep 2004.
 - [94] S. T. Wu, "Birefringence dispersions of liquid-crystals," *Physical Review A*, vol. 33, pp. 1270-1274, Feb 1986.
 - [95] F. C. Frank, "On the theory of liquid crystals," *Discussions of the Faraday Society*, 1958.
 - [96] T. R. Wolinski, et al., "Propagation effects in a photonic crystal fiber filled with a low-birefringence liquid crystal," in *Liquid Crystals VIII*. vol. 5518, Bellingham: Spie-Int Soc Optical Engineering, 2004, pp. 232-237.
 - [97] K. Nowecka, et al., "Influence of temperature and electric field on polarization properties in photonic liquid crystal fibers - art. no. 66080J," in *Lightguides and Their Applications III*. vol. 6608, J. Wojcik and W. Wojcik, Eds., ed, 2007.
 - [98] I. Janossy, "Molecular interpretation of the absorption-induced optical reorientation of nematic liquid-crystals," *Physical Review E*, vol. 49, pp. 2957-2963, Apr 1994.
 - [99] J. Du, et al., "Electrically tunable Sagnac filter based on a photonic bandgap fiber with liquid crystal infused," *Opt. Lett.*, vol. 33, pp. 2215-2217, 2008.
 - [100] Y. J. Liu, et al., "Lasing from a one-dimensional photonic crystal made of dye-doped holographic polymer-dispersed liquid crystal gratings," *Japanese Journal of Applied Physics Part 2-Letters & Express Letters*, vol. 45, pp.

- L559-L561, Jun 2006.
- [101] Y. J. Liu, et al., "Holographic fabrication of azo-dye-functionalized photonic structures," *Journal of Materials Chemistry*, vol. 21, pp. 2982-2986, 2011.
 - [102] C. H. Lee, et al., "Photo and electrical tunable effects in photonic liquid crystal fiber," *Optics Express*, vol. 18, pp. 2814-2821, Feb 2010.
 - [103] T. Alkeskjold, et al., "All-optical modulation in dye-doped nematic liquid crystal photonic bandgap fibers," *Opt. Express*, vol. 12, pp. 5857-5871, 2004.
 - [104] C. R. Lee, et al., "Surface-assisted photoalignment in dye-doped liquid-crystal films," *Physical Review E*, vol. 69, p. 031704, 2004.
 - [105] H. Ringsdorf and H. W. Schmidt, "Electro-optical effects of azo dye containing liquid-crystalline copolymers," *Makromolekulare Chemie-Macromolecular Chemistry and Physics*, vol. 185, pp. 1327-1334, 1984.
 - [106] I. Janossy, et al., "Temperature-dependence of the optical freedericksz transition in dyed nematic liquid-crystals," *Physical Review A*, vol. 44, pp. 8410-8413, Dec 1991.
 - [107] G. Alagappan, et al., "Tunable dispersion properties of liquid crystal infiltrated into a two-dimensional photonic crystal," *IEEE Journal of Quantum Electronics*, vol. 42, pp. 404-409, Mar-Apr 2006.
 - [108] A. Y. G. Fuh, et al., "Laser-induced reorientation effect and ripple structure in dye-doped liquid-crystal films," *Optics Letters*, vol. 28, pp. 1179-1181, Jul 2003.
 - [109] C. Y. Huang, et al., "Dynamics of photoalignment in azo-dye-doped liquid crystals," *Applied Physics Letters*, vol. 93, Nov 2008.
 - [110] K. T. Cheng, et al., "Electrically switchable and optically rewritable reflective Fresnel zone plate in dye-doped cholesteric liquid crystals," *Optics Express*, vol. 15, pp. 14078-14085, Oct 2007.
 - [111] W. M. Gibbons, et al., "Surface-mediated alignment of nematic liquid-crystals with polarized laser-light," *Nature*, vol. 351, pp. 49-50, May 1991.
 - [112] T. R. Wolinski, et al., "Polarization effects in photonic liquid crystal fibers," *Measurement Science & Technology*, vol. 18, pp. 3061-3069, Oct 2007.
 - [113] T. R. Wolinski, et al., "Tunable highly birefringent solid-core photonic liquid crystal fibers," *Optical and Quantum Electronics*, vol. 39, pp. 1021-1032, Oct 2007.
 - [114] S. Ertman, et al., "Liquid crystal molecular orientation in photonic liquid crystal fibers with photopolymer layers - art. no. 658706," in *Liquid Crystals and Applications in Optics*. vol. 6587, M. Glogarova, et al., Eds., ed, 2007.
 - [115] K. Pavani, et al., "Electro-optical switching of the holographic polymer-dispersed liquid crystal diffraction gratings," *Journal of Optics a-Pure and Applied Optics*, vol. 11, Feb 2009.
 - [116] J. Sun, et al., "Analysis of photonic crystal fibers infiltrated with nematic liquid crystal," *Optics Communications*, vol. 278, pp. 66-70, Oct 2007.

- [117] P. T. I. Professor Yue Zhao, *Smart Light-Responsive Materials: Azobenzene-Containing Polymers and Liquid Crystals*: John Wiley & Sons Inc, 2008.
- [118] F. S. a. O. Francescangeli, "Effects of light on molecular orientation of liquid crystals," *Journal of Physics: Condensed Matter*, 1999.
- [119] B. Dunn, et al., "Strategies for encapsulating biomolecules in sol-gel matrices," *Acta Materialia*, vol. 46, pp. 737-741, Jan 1998.
- [120] O. O. Ramdane, et al., "Memory-free conic anchoring of liquid crystals on a solid substrate," *Physical Review Letters*, vol. 84, pp. 3871-3874, Apr 2000.

-
- [1] T. G. Giallorenzi, *et al.*, "Optical fiber sensor technology," *IEEE Journal of Quantum Electronics*, vol. 18, pp. 626-665, 1982.
 - [2] J. D. Joannopoulos, *et al.*, "Photonic crystals: Putting a new twist on light," *Nature*, vol. 386, pp. 143-149, Mar 1997.
 - [3] P. Russell, "Photonic crystal fibers," *Science*, vol. 299, pp. 358-362, Jan 2003.
 - [4] O. S. Wolfbeis, "Fiber-optic chemical sensors and biosensors," *Analytical Chemistry*, vol. 76, pp. 3269-3283, Jun 2004.
 - [5] M. D. Marazuela and M. C. Moreno-Bondi, "Fiber-optic biosensors - an overview," *Analytical and Bioanalytical Chemistry*, vol. 372, pp. 664-682, Mar 2002.
 - [6] A. Yariv, "Coupled-mode theory for guided-wave optics," *IEEE Journal of Quantum Electronics*, vol. QE 9, pp. 919-933, 1973.
 - [7] T. Erdogan, "Cladding-mode resonances in short- and long-period fiber grating filters," *Journal of the Optical Society of America a-Optics Image Science and Vision*, vol. 14, pp. 1760-1773, Aug 1997.
 - [8] A. Asseh, *et al.*, "Fiber optical Bragg grating refractometer," *Fiber and Integrated Optics*, vol. 17, pp. 51-62, 1998.
 - [9] V. Bhatia and A. M. Vengsarkar, "Optical fiber long-period grating sensors," *Optics Letters*, vol. 21, pp. 692-694, May 1996.
 - [10] A. D. Kersey, *et al.*, "Fiber grating sensors," *Journal of Lightwave Technology*, vol. 15, pp. 1442-1463, Aug 1997.
 - [11] Y. J. Rao, "In-fibre Bragg grating sensors," *Measurement Science & Technology*, vol. 8, pp. 355-375, Apr 1997.
 - [12] D. A. Pereira, *et al.*, "Fiber Bragg grating sensing system for simultaneous measurement of salinity and temperature," *Optical Engineering*, vol. 43, pp. 299-304, Feb 2004.
 - [13] H. J. Patrick, *et al.*, "Analysis of the response of long period fiber gratings to external index of refraction," *Journal of Lightwave Technology*, vol. 16, pp. 1606-1612, Sep 1998.
 - [14] T. Eftimov, "Sensor applications of LPGs and FBGs," *Optical Sensing & Imaging*, 2006.
 - [15] A. Quirrenbach, "Optical interferometry," *Annual Review of Astronomy and Astrophysics*, vol. 39, pp. 353-401, 2001.
 - [16] B. H. Lee, *et al.*, "Interferometric Fiber Optic Sensors," *Sensors*, vol. 12, pp. 2467-2486, Mar 2012.
 - [17] X. Li, *et al.*, "Research on Laser Spectrum Detecting Technology Based on Static Mach-Zehnder Interferometer," *Spectroscopy and Spectral Analysis*, vol. 29, pp. 62-65, Jan 2009.
 - [18] B. Culshaw, "The optical fibre Sagnac interferometer: an overview of its principles and applications," *Measurement Science & Technology*, vol. 17, pp. R1-R16, Jan 2006.

-
- [19] R. Anderson, *et al.*, "Sagnac effect - A century of earth-rotated interferometers," *American Journal of Physics*, vol. 62, pp. 975-985, Nov 1994.
 - [20] E. Yablonovitch, *et al.*, "Photonic band-structure - the face-centered-cubic case employing nonspherical atoms," *Physical Review Letters*, vol. 67, pp. 2295-2298, Oct 1991.
 - [21] P. S. J. Russell, "Photonic-crystal fibers," *Journal of Lightwave Technology*, vol. 24, pp. 4729-4749, Dec 2006.
 - [22] T. A. Birks, *et al.*, "Endlessly single-mode photonic crystal fiber," *Optics Letters*, vol. 22, pp. 961-963, Jul 1997.
 - [23] J. C. Knight, "Photonic crystal fibres," *Nature*, vol. 424, pp. 847-851, Aug 2003.
 - [24] A. C. Federica Poli, Stefano Selleri, Ed., *Photonic crystal fibers: properties and applications*. Netherlands: Springer, 2007.
 - [25] R. Buczynski, "Photonic crystal fibers," *Acta Physica Polonica A*, vol. 106, pp. 141-167, Aug 2004.
 - [26] D. C. Zografopoulos, *et al.*, "Photonic crystal-liquid crystal fibers for single-polarization or high- birefringence guidance," *Optics Express*, vol. 14, pp. 914-925, Jan 2006.
 - [27] T. A. Birks, *et al.*, "Approximate band structure calculation for photonic bandgap fibres," *Optics Express*, vol. 14, pp. 9483-9490, Oct 2006.
 - [28] R. V. K. Wes R. Jamroz, Emile I. Haddad, Ed., *Applied microphotronics*. Boca Raton: Taylor and Francis Group, 2006.
 - [29] S.-T. W. Iam-Choon Khoo, Ed., *Optics and Nonlinear Optics of Liquid Crystals*. World Scientific, 1993.
 - [30] H. Kelker, "History of Liquid Crystals," *Molecular Crystals and Liquid Crystals*, vol. 21, pp. 1-48, 1973.
 - [31] S. Chandrasekhar and N. V. Madhusudana, "Liquid crystals," *Annual Review of Materials Science*, vol. 10, 1980.
 - [32] D. Demus, Ed., *Phase types, structures and chemistry of liquid crystals* (Horst Stegemeyer, Liquid Crystals. New York: Springer, 1994.
 - [33] S. Chandrasekhar, Ed., *Liquid Crystals*. New York: Cambridge University Press, 1992s.
 - [34] M. K. Mandal, Ed., *Multimedia Signals and Systems*. Boston/ Dordrecht/ London: Kluwer Academic Publishers, 2003.
 - [35] *Nematic Phase of Liquid Crystal*. Available: <http://upload.wikimedia.org/wikipedia/commons/8/80/LiquidCrystal-MesogenOrder-Nematic.jpg>
 - [36] *Smectic Phases of Liquid Crystal*. Available: <http://upload.wikimedia.org/wikipedia/commons/f/f2/LiquidCrystal-MesogenOrder-SmecticPhases.jpg>
 - [37] *Chiral Phase of Liquid Crystal*. Available: <http://upload.wikimedia.org/wikipedia/commons/b/bf/LiquidCrystal-MesogenOrder-ChiralPhase.jpg>

- [er-ChiralPhases.jpg](#)
- [38] Y. Jeong and B. Lee, "Theory of electrically controllable long-period gratings built in liquid-crystal fibers," *Optical Engineering*, vol. 40, pp. 1227-1233, Jul 2001.
 - [39] I. C. Khoo, "Nonlinear optics of liquid crystalline materials," *Physics Reports-Review Section of Physics Letters*, vol. 471, pp. 221-267, Feb 2009.
 - [40] *Photos of Various Fluorescent Dyes.* Available: <http://upload.wikimedia.org/wikipedia/commons/thumb/0/09/FluorescentCells.jpg/200px-FluorescentCells.jpg>
 - [41] N. A. Davidenko, *et al.*, "Optical, electrical, and photophysical properties of films of polycomplexes of azobenzene derivatives with cobalt," *Optics and Spectroscopy*, vol. 101, pp. 906-913, Dec 2006.
 - [42] *High resolution scanning tunneling microscopy image of Carbon Nanotube* Available: <http://upload.wikimedia.org/wikipedia/commons/5/5f/Chiraltube.gif>
 - [43] *Multi-Walled Carbon Nanotube.* Available: http://upload.wikimedia.org/wikipedia/commons/b/bc/Multi-walled_Carbon_Nanotube.png
 - [44] *Rolling of a layer of graphene into a seamless Carbon Nanotube.* Available: http://upload.wikimedia.org/wikipedia/commons/c/c4/Carbon_nanoribbon_povray.PNG
 - [45] "Rolling of a layer of graphene into a seamless Carbon Nanotube."
 - [46] C. Fantini, *et al.*, "Optical transition energies for carbon nanotubes from resonant Raman spectroscopy: Environment and temperature effects," *Physical Review Letters*, vol. 93, Oct 2004.
 - [47] J. K. Lim, *et al.*, "A phase-stabilized carbon nanotube fiber laser frequency comb," *Optics Express*, vol. 17, pp. 14115-14120, Aug 2009.
 - [48] D. G. Georganopoulou, *et al.*, "Nanoparticle-based detection in cerebral spinal fluid of a soluble pathogenic biomarker for Alzheimer's disease," *Proceedings of the National Academy of Sciences of the United States of America*, vol. 102, pp. 2273-2276, Feb 2005.
 - [49] X. Liu, *et al.*, "A one-step homogeneous immunoassay for cancer biomarker detection using gold nanoparticle probes coupled with dynamic light scattering," *Journal of the American Chemical Society*, vol. 130, pp. 2780-+, Mar 2008.
 - [50] M. Grande, *et al.*, "Asymmetric plasmonic grating for optical sensing of thin layers of organic materials," *Sensors and Actuators B-Chemical*, vol. 160, pp. 1056-1062, Dec 2011.
 - [51] *TEM Images of Silica Nanoparticle.* Available: http://upload.wikimedia.org/wikipedia/commons/6/6d/Mesoporous_Silica_Nanoparticle.jpg
 - [52] A. B. W. J. Hecht, Ed. York, Ed., *Understand Fiber Optics*. PA: Pearson Prentice Hall, 2006.

-
- [53] K. T. V. Grattan, Ed., *Optical Fiber Sensor Technology: Devices and Technology*. Springer, 1997.
 - [54] A. D. Kersey, *et al.*, "High-resolution fiber-grating based strain sensor with interferometric wavelength-shift detection," *Electronics Letters*, vol. 28, pp. 236-238, Jan 1992.
 - [55] Y. Z. Zhu and A. B. Wang, "Miniature fiber-optic pressure sensor," *Ieee Photonics Technology Letters*, vol. 17, pp. 447-449, Feb 2005.
 - [56] J. Broeng, *et al.*, "Photonic crystal fibers: A new class of optical waveguides," *Optical Fiber Technology*, vol. 5, pp. 305-330, Jul 1999.
 - [57] X. W. Shu, *et al.*, "Sensitivity characteristics of long-period fiber gratings," *Journal of Lightwave Technology*, vol. 20, pp. 255-266, Feb 2002.
 - [58] S. W. James and R. P. Tatam, "Optical fibre long-period grating sensors: Characteristics and application," *Measurement Science & Technology*, vol. 14, pp. R49-R61, 2003.
 - [59] S. Shtelzer and S. Braun, "An optical biosensor based upon glucose-oxidase immobilized in sol-gel silicate matrix," *Biotechnology and Applied Biochemistry*, vol. 19, pp. 293-305, Jun 1994.
 - [60] W. W. M. G. Meltz, and W. H. Glenn, "In-fibre Bragg grating tap," presented at the Optical fiber Communication Conference, OFC'90, San Francisco, 1990.
 - [61] G. Laffont and P. Ferdinand, "Tilted short-period fibre-Bragg-grating-induced coupling to cladding modes for accurate refractometry," *Measurement Science & Technology*, vol. 12, pp. 765-770, Jul 2001.
 - [62] C. Caucheteur, *et al.*, "Tilted Fiber Bragg Grating Refractometer Using Polarization-Dependent Loss Measurement," *Ieee Photonics Technology Letters*, vol. 20, pp. 2153-2155, Nov-Dec 2008.
 - [63] C. Chen, *et al.*, "The sensitivity characteristics of tilted fibre Bragg grating sensors with different cladding thicknesses," *Measurement Science & Technology*, vol. 18, pp. 3117-3122, Oct 2007.
 - [64] T. Guo, *et al.*, "Temperature-independent tilted fiber grating vibration sensor based on cladding-core recoupling," *Optics Letters*, vol. 33, pp. 1004-1006, May 2008.
 - [65] E. Kerrinckx, *et al.*, "Suppression of discrete cladding mode resonances in fibre slanted Bragg gratings for gain equalisation," *Optics Express*, vol. 14, pp. 1388-1394, Feb 2006.
 - [66] C. W. Haggans, *et al.*, "Narrow-band rejection filters with negligible backreflection using tilted photoinduced gratings in single-mode fibers," *Ieee Photonics Technology Letters*, vol. 10, pp. 690-692, May 1998.
 - [67] H. S. Park, *et al.*, "All-fiber add-drop wavelength-division multiplexer based on intermodal coupling," *IEEE Photonics Technology Letters*, vol. 13, pp. 460-462, May 2001.
 - [68] E. Marin, *et al.*, "Bragg gratings in 2 x 2 symmetric fused fiber couplers:

- Influence of the tilt on the wavelength response," *IEEE Photonics Technology Letters*, vol. 11, pp. 1434-1436, Nov 1999.
- [69] X. Yu, *et al.*, "Highly Sensitive Photonic Crystal Fiber-Based Refractive Index Sensing Using Mechanical Long-Period Grating," *IEEE Photonics Technology Letters*, vol. 20, pp. 1688-1690, Sep-Oct 2008.
- [70] J. H. Lim, *et al.*, "Tunable fiber gratings fabricated in photonic crystal fiber by use of mechanical pressure," *Optics Letters*, vol. 29, pp. 331-333, Feb 2004.
- [71] R. Kashyap, *Fiber Bragg Gratings*, Second ed.: Elsevier Inc., 2010.
- [72] L. Dong, *et al.*, "Coupling characteristics of cladding modes in tilted optical fiber Bragg gratings," *Applied Optics*, vol. 37, pp. 5099-5105, Aug 1998.
- [73] G. Antonopoulos, *et al.*, "Experimental demonstration of the frequency shift of bandgaps in photonic crystal fibers due to refractive index scaling," *Optics Express*, vol. 14, pp. 3000-3006, Apr 2006.
- [74] T. A. Birks, *et al.*, "Scaling laws and vector effects in bandgap-guiding fibres," *Optics Express*, vol. 12, pp. 69-74, Jan 2004.
- [75] X. Yu, *et al.*, "Photonic crystal fibers with high index infiltrations for refractive index sensing," *Optics Communications*, vol. 281, pp. 4555-4559, Sep 2008.
- [76] J. Zeng, *et al.*, "Applications of optical fiber SPR sensor for measuring of temperature and concentration of liquids," in *17th International Conference on Optical Fibre Sensors*, Brugge, Belgium, 2005, pp. 667-670.
- [77] J. Sun and C. C. Chan, "Photonic bandgap fiber for refractive index measurement," *Sensors and Actuators B-Chemical*, vol. 128, pp. 46-50, Dec 2007.
- [78] J. B. Jensen, *et al.*, "Photonic crystal fiber based evanescent-wave sensor for detection of biomolecules in aqueous solutions," *Optics Letters*, vol. 29, pp. 1974-1976, Sep 2004.
- [79] R. A. Potyrailo, *et al.*, "A dual-parameter optical sensor fabricated by gradient axial doping of an optical fibre," *Measurement Science & Technology*, vol. 16, pp. 235-241, Jan 2005.
- [80] W. Peng, *et al.*, "Investigation of dual-channel fiber-optic surface plasmon resonance sensing for biological applications," *Opt. Lett.*, vol. 30, pp. 2988-2990, 2005.
- [81] M. A. van Eijkelenborg, *et al.*, "Microstructured polymer optical fibre," *Optics Express*, vol. 9, pp. 319-327, Sep 2001.
- [82] J. Jensen, *et al.*, "Selective detection of antibodies in microstructured polymer optical fibers," *Opt. Express*, vol. 13, pp. 5883-5889, 2005.
- [83] P. N. Prasad, "Optical Biosensors," *Introduction to Biophotonics*, pp. 311 - 356, 2003.
- [84] M. P. DeLisa, *et al.*, "Evanescent wave long-period fiber bragg grating as an immobilized antibody biosensor," *Analytical Chemistry*, vol. 72, pp. 2895-2900, 2000.
- [85] P. J. A. Sazio, *et al.*, "Microstructured optical fibers as high-pressure microfluidic

- reactors," *Science*, vol. 311, pp. 1583-1586, Mar 2006.
- [86] J. Sun, *et al.*, "High-resolution photonic bandgap fiber-based biochemical sensor," *Journal of Biomedical Optics*, vol. 12, Jul-Aug 2007.
- [87] L. Rindorf, *et al.*, "Photonic crystal fiber long-period gratings for biochemical sensing," *Opt. Express*, vol. 14, pp. 8224-8231, 2006.
- [88] I.-C. Khoo, Ed., *Liquid Crystals*. John Wiley & Sons, 2007.
- [89] T. R. Wolinski, *et al.*, "Polarization optics of microstructured liquid crystal fibers," *Molecular Crystals and Liquid Crystals*, vol. 454, pp. 325-342, 2006.
- [90] S. T. Kowel, *et al.*, "Focusing by electrical modulation of refraction in a liquid-crystal cell," *Applied Optics*, vol. 23, pp. 278-289, 1984.
- [91] L. A. Madsen, *et al.*, "Thermotropic biaxial nematic liquid crystals," *Physical Review Letters*, vol. 92, Apr 2004.
- [92] J. B. Du, *et al.*, "Electrically tunable Sagnac filter based on a photonic bandgap fiber with liquid crystal infused," *Optics Letters*, vol. 33, pp. 2215-2217, Oct 2008.
- [93] D. H. Kim and J. U. Kang, "Sagnac loop interferometer based on polarization maintaining photonic crystal fiber with reduced temperature sensitivity," *Optics Express*, vol. 12, pp. 4490-4495, Sep 2004.
- [94] S. T. Wu, "Birefringence dispersions of liquid-crystals," *Physical Review A*, vol. 33, pp. 1270-1274, Feb 1986.
- [95] F. C. Frank, "On the theory of liquid crystals," *Discussions of the Faraday Society*, 1958.
- [96] T. R. Wolinski, *et al.*, "Propagation effects in a photonic crystal fiber filled with a low-birefringence liquid crystal," in *Liquid Crystals VIII*. vol. 5518, Bellingham: Spie-Int Soc Optical Engineering, 2004, pp. 232-237.
- [97] K. Nowecka, *et al.*, "Influence of temperature and electric field on polarization properties in photonic liquid crystal fibers - art. no. 66080J," in *Lightguides and Their Applications III*. vol. 6608, J. Wojcik and W. Wojcik, Eds., ed, 2007.
- [98] I. Janossy, "Molecular interpretation of the absorption-induced optical reorientation of nematic liquid-crystals," *Physical Review E*, vol. 49, pp. 2957-2963, Apr 1994.
- [99] J. Du, *et al.*, "Electrically tunable Sagnac filter based on a photonic bandgap fiber with liquid crystal infused," *Opt. Lett.*, vol. 33, pp. 2215-2217, 2008.
- [100] Y. J. Liu, *et al.*, "Lasing from a one-dimensional photonic crystal made of dye-doped holographic polymer-dispersed liquid crystal gratings," *Japanese Journal of Applied Physics Part 2-Letters & Express Letters*, vol. 45, pp. L559-L561, Jun 2006.
- [101] Y. J. Liu, *et al.*, "Holographic fabrication of azo-dye-functionalized photonic structures," *Journal of Materials Chemistry*, vol. 21, pp. 2982-2986, 2011.
- [102] C. H. Lee, *et al.*, "Photo and electrical tunable effects in photonic liquid crystal fiber," *Optics Express*, vol. 18, pp. 2814-2821, Feb 2010.

-
- [103] T. Alkeskjold, *et al.*, "All-optical modulation in dye-doped nematic liquid crystal photonic bandgap fibers," *Opt. Express*, vol. 12, pp. 5857-5871, 2004.
- [104] C. R. Lee, *et al.*, "Surface-assisted photoalignment in dye-doped liquid-crystal films," *Physical Review E*, vol. 69, p. 031704, 2004.
- [105] H. Ringsdorf and H. W. Schmidt, "Electro-optical effects of azo dye containing liquid-crystalline copolymers," *Makromolekulare Chemie-Macromolecular Chemistry and Physics*, vol. 185, pp. 1327-1334, 1984.
- [106] I. Janossy, *et al.*, "Temperature-dependence of the optical freedericksz transition in dyed nematic liquid-crystals," *Physical Review A*, vol. 44, pp. 8410-8413, Dec 1991.
- [107] G. Alagappan, *et al.*, "Tunable dispersion properties of liquid crystal infiltrated into a two-dimensional photonic crystal," *IEEE Journal of Quantum Electronics*, vol. 42, pp. 404-409, Mar-Apr 2006.
- [108] A. Y. G. Fuh, *et al.*, "Laser-induced reorientation effect and ripple structure in dye-doped liquid-crystal films," *Optics Letters*, vol. 28, pp. 1179-1181, Jul 2003.
- [109] C. Y. Huang, *et al.*, "Dynamics of photoalignment in azo-dye-doped liquid crystals," *Applied Physics Letters*, vol. 93, Nov 2008.
- [110] K. T. Cheng, *et al.*, "Electrically switchable and optically rewritable reflective Fresnel zone plate in dye-doped cholesteric liquid crystals," *Optics Express*, vol. 15, pp. 14078-14085, Oct 2007.
- [111] W. M. Gibbons, *et al.*, "Surface-mediated alignment of nematic liquid-crystals with polarized laser-light," *Nature*, vol. 351, pp. 49-50, May 1991.
- [112] T. R. Wolinski, *et al.*, "Polarization effects in photonic liquid crystal fibers," *Measurement Science & Technology*, vol. 18, pp. 3061-3069, Oct 2007.
- [113] T. R. Wolinski, *et al.*, "Tunable highly birefringent solid-core photonic liquid crystal fibers," *Optical and Quantum Electronics*, vol. 39, pp. 1021-1032, Oct 2007.
- [114] S. Ertman, *et al.*, "Liquid crystal molecular orientation in photonic liquid crystal fibers with photopolymer layers - art. no. 658706," in *Liquid Crystals and Applications in Optics*, vol. 6587, M. Glogarova, *et al.*, Eds., ed, 2007.
- [115] K. Pavani, *et al.*, "Electro-optical switching of the holographic polymer-dispersed liquid crystal diffraction gratings," *Journal of Optics a-Pure and Applied Optics*, vol. 11, Feb 2009.
- [116] J. Sun, *et al.*, "Analysis of photonic crystal fibers infiltrated with nematic liquid crystal," *Optics Communications*, vol. 278, pp. 66-70, Oct 2007.
- [117] P. T. I. Professor Yue Zhao, *Smart Light-Responsive Materials: Azobenzene-Containing Polymers and Liquid Crystals*: John Wiley & Sons Inc, 2008.
- [118] F. S. a. O. Francescangeli, "Effects of light on molecular orientation of liquid crystals," *Journal of Physics: Condensed Matter*, 1999.
- [119] B. Dunn, *et al.*, "Strategies for encapsulating biomolecules in sol-gel matrices,"

- Acta Materialia*, vol. 46, pp. 737-741, Jan 1998.
- [120] O. O. Ramdane, *et al.*, "Memory-free conic anchoring of liquid crystals on a solid substrate," *Physical Review Letters*, vol. 84, pp. 3871-3874, Apr 2000.